VIBRATION SUPPRESSION AND FLYWHEEL ENERGY STORAGE IN A DRILLSTRING BOTTOM-HOLE-ASSEMBLY

A Dissertation

by

AHMED MOHAMED SAEED

Submitted to the Office of Graduate Studies of
Texas A&M University
in partial fulfillment of the requirements for the degree of

DOCTOR OF PHILOSOPHY

May 2012

Major Subject: Mechanical Engineering

Vibration Suppression and Flywheel Energy Storage in a Drillstring Bottom-Hole-Assembly

VIBRATION SUPPRESSION AND FLYWHEEL ENERGY STORAGE IN A DRILLSTRING BOTTOM-HOLE-ASSEMBLY

A Dissertation

by

AHMED MOHAMED SAEED

Submitted to the Office of Graduate Studies of
Texas A&M University
in partial fulfillment of the requirements for the degree of

DOCTOR OF PHILOSOPHY

Approved by:

Co-Chairs of Committee,	Alan Palazzolo
	Shehab Ahmed
Committee Members,	Won-jong Kim
	Daniel McAdams
Head of Department,	Jerald Caton

May 2012

Major Subject: Mechanical Engineering

ABSTRACT

Vibration Suppression and Flywheel Energy Storage in a Drillstring Bottom-Hole-Assembly. (May 2012)

Ahmed Mohamed Saeed, B.S.; M.S., Alexandria University-Egypt

Co-Chairs of Advisory Committee: Dr. Alan Palazzolo
Dr. Shehab Ahmed

In this study, a novel concept for a downhole flywheel energy storage module to be embedded in a bottom-hole-assembly (BHA) is presented and modeled, as an alternative power source to existing lithium-ion battery packs currently deployed in measurement-while-drilling (MWD) or logging-while-drilling (LWD) operations. Lithium-ion batteries disadvantages include deteriorated performance in high temperature, limited lifetime that necessitates frequent replacement which elevates operational costs, and environmental disposal. Extreme and harsh downhole conditions necessitate that the flywheel module withstands temperatures and pressures exceeding 300℉ and 20 kpsi, respectively, as well as violent vibrations encountered during drilling. Moreover, the flywheel module should adhere to the geometric constraints of the wellbore and its corresponding BHA.

Hence, a flywheel sizing procedure was developed that takes into consideration the required energy to be stored, the surrounding environmental conditions, and the geometric constraints. A five-axis magnetic levitation control system was implemented and tuned to maintain continuous suspension of the flywheel under the harsh lateral,

axial and torsional drilling vibrations of the BHA. Thus, an integrated finite element model was developed that included the rotordynamic behavior of the flywheel and the BHA, the component dynamics of the magnetic levitation control system, and the cutting dynamics of the drillbit for both PDC and tricone types. The model also included a newly developed coupling between lateral, axial and torsional vibrations. It was demonstrated through simulations conducted by numerical integration that the flywheel maintains levitation due to all different types of external vibration as well as its own lateral vibration due to mass unbalance. Moreover, a passive proof-mass-damper (PPMD) was developed that suppresses axial bit-bounce vibrations as well as torsional vibrations, and was extended to also mitigate lateral vibrations. Optimized values of the mass, stiffness and damping values of the PPMD were obtained by the hybrid analytical-numerical Chebyshev spectral method that was superior in computational efficiency to iterative numerical integration. This also enabled the fine-plotting of an operating stability chart indicating stability regions where bit-bounce and stick-slip are avoided. The proof-mass-damping concept was extended to the flywheel to be an active proof-mass-damper (APMD) where simulations indicated functionality for a light-weight BHA.

DEDICATION

To My Family

ACKNOWLEDGEMENTS

I would like to thank my committee co-chairs, Dr. Palazzolo and Dr. Ahmed for their limitless support and guidance throughout the course of this research. I would also like to thank Dr. Kim, and Dr. McAdams, for serving on my committee, and giving their insights.

Thanks also go to my friends and colleagues and the department faculty and staff for making my time at Texas A&M University a great experience. I also want to extend my gratitude to the Qatar National Research Fund for funding this research and making this work possible through NPRP Grant # C11-00349.

Finally, thanks to my mother and father for their encouragement and to my wife for her patience and love.

NOMENCLATURE

a	Drillbit Radius
AMB	Active Magnetic Bearing
APMD	Active Proof-Mass-Damper
b	Roller-Cone Drillbit Factor
BHA	Bottom-Hole-Assembly
C	Damping Matrix
c_{abs}	Shock Absorber Damping
C_{AMB}	AMB Equivalent Damping
c_f, c_{fT}	PPMD Axial & Torsional Damping
CG	Center of Gravity
C_T	BHA Torsional Damping-to-Ground
c_1, c_2	Axial Applied Load – ROP Relation Factors
d, d_n	Total Depth of Cut & Depth of Cut/Blade
D_i	Inner Pipe Diameter
E	Energy Stored in Flywheel
e	Error Voltage
e_0	BHA Mass Unbalance Eccentricity
FEM	Finite Element Model
f_m, f_{nm}	Magnetic, Non-Magnetic Forces
FOS	Factor of Safety

F_r, F_t	Radial & Tangential BHA-Wellbore Contact Forces
F_y, F_z	Lateral Forces Due to BHA Mass Unbalance in Y & Z Directions
G_p	Controller Proportional Gain
G_d	Controller Derivative Gain
i_{PA}	Power Amplifier/Coil Current
J	BHA Inertia
J_f	Flywheel Inertia
K	Stiffness Matrix
k_{abs}	Shock Absorber Stiffness
K_{AMB}	AMB Equivalent Stiffness
K_B	Wellbore Contact Stiffness
k_c	Equivalent Rock Formation Stiffness
k_f, k_{fT}	PPMD Axial & Torsional Stiffness
K_i	Current Stiffness
K_L	Lead/Lag Compensator Gain
K_{PA}	Power Amplifier Overall Gain
k_{PA}	Power Amplifier Feed-Forward Gain
K_S	Position Sensor Gain
K_T	BHA Torsional Stiffness-to-ground
K_x	Position Stiffness
L	Coil Inductance
l	Drillbit Wearflat Length

LWD	Logging While Drilling
M	Mass Matrix
m_{abs}	Shock Absorber Mass
m_{DC}	Drill-Collar/BHA Mass
MWD	Measurement While Drilling
MR	Magneto Rheological
n	Number of Blades
p	Lead/Lag Compensator Pole
PD	Proportional Derivative
PDC	Polycrystalline Diamond Compact
PID	Proportional Integral Derivative
P_{max}	Maximum Downhole Pressure
PPMD	Proof-Mass-Damper
r_{fi}	Inner Flywheel Radius
r_{fo}	Outer Flywheel Radius
Q	Notch Filter Quality Factor
R	Coil Resistance
r	Radial Displacement of BHA CG
r_c	Radial BHA-Wellbore Clearance
ROP	Rate of Penetration
s, s_0	Formation, Mean Formation Elevation
S_a	Alternating Stress

S_e	Endurance Strength
S_m	Mean Stress
S_y	Yield Stress
t	time
T_c, T_f	Cutting, Friction Components of TOB
T_d	Top Drive Torque
TOB	Torque on Bit
t_{pipe}	Pipe Thickness
t_n	Blade Time Delay
v_e, v_{PA}, v_{PD}, v_R, v_S	Error, Power Amplifier, PD, Reference, Sensor Voltage
W_c, W_f	Cutting, Friction Components of WOB
W_o	Axial Applied Load at the Top of the Drill Rig
WOB	Weight on Bit
x_d,y_d, z_d	BHA CG Displacements in X, Y & Z Directions
x_f,y_f, z_f	PPMD Displacements in X, Y & Z Directions
z	Lead/Lag Compensator Zero
α	Inclination of WOB with Respect to BHA
ε	Rock Specific Intrinsic Energy
ζ	Drillbit-Formation Interaction Factor
ϕ	Drillbit Angular Displacement
ϕ_f	PPMD Angular Displacement
γ	Power Amplifier Feedback Gain

μ, μ_0	Drillbit-Formation Stribeck & Mean Contact Friction
μ_w	Wellbore-BHA Mean Contact Friction
υ	Poisson's Ratio
ρ	Material Density
σ	Rock Cutting Stress
$\sigma_{\max}$	Permissible Normal Stress
σ_θ	Tangential Normal Stress
τ_c, τ_f, τ_s	Controller, Filter, Sensor Time Constants
Ω	Drillbit Angular Velocity
ω_c	BHA CG Whirling Rate
ω_d	Top Drive Spin Velocity
ω_f	Flywheel Spin Velocity
ω_{min}, ω_{max}	Minimum, Maximum Flywheel Spin Velocity

TABLE OF CONTENTS

Page

LIST OF FIGURES

FIGURE Page

FIGURE Page

FIGURE Page

FIGURE Page

FIGURE Page

LIST OF TABLES

1. INTRODUCTION

1.1 Statement of the Problem

As the quest for exploiting underground reservoirs have become more challenging than in the past, oil and gas companies are continuously deploying sophisticated operations than ever before. Logging-while-drilling (LWD) or measurement-while-drilling (MWD) operations utilize downhole lithium-ion batteries to supply power supply to the logging/measurement tools. However, lithium-ion batteries have to be replaced after a short period of time, and their operation deteriorates under high temperatures in ultra-deep wells in addition to the environmental hazards associated with the disposal process. Moreover, the battery packs have to be exchanged after 100 hours of operation which means that the logging job would have to be interrupted, the tools be lifted back up to the surface to be disassembled and reassembled and finally lowered down the well to the point where the logging operation was interrupted. Obviously, the battery replacement process is uneconomic increasing the cost of operations by millions of dollars. Hence, in this work, a permanent downhole flywheel is proposed as an alternative to serve as an energy storage device, and is to be embedded in the bottom-hole-assembly (BHA) of the drillstring. In addition to the harsh downhole environment, the active magnetic bearings (AMB) must maintain levitation of the flywheel when the drillstring is subjected to violent downhole vibrations. This also necessitates the investigation and analysis of the different types of drillstring vibrations and finding practical solutions to suppress or mitigate these harmful vibrations

---

This dissertation follows the style of *Journal of Sound & Vibration.*

1.2 Literature Review

The problem of drillstring vibrations has been recognized as one of the prime causes of deterioration in drilling performance, and these vibrations can be lateral, torsional, or axial. Field observations have indicated that drillstrings exhibit severe vibrations that become more severe at the bottom-hole assembly (BHA). The BHA comprises the drillcollars, stabilizers, and the bit in addition to other logging tools and instruments. As the drill-bit is penetrating the formation during drilling, the normal reaction force, or weight-on-bit (WOB) can become excessive and fluctuate causing axial vibration in the drill-string & this is also known as bit-bounce. Excessive axial vibration or bit-bounce can lead deterioration of rate-of-penetration (ROP) as well as drill-bit damage, adverse effect on the telemetry tools & the data it conveys to the surface and fatigue of the drill-pipes that all leads to decreased efficiency in the drilling process and increased costs in operation & replacement of components. Excessive torsional vibrations can eventually lead to limit cycles where the BHA rotary speeds are bounded between zero and 2 or even 3 times the designated rotary table speed. This is known as stick-slip phenomenon where the drill-bit momentarily reaches zero velocity and "sticks" and then due to buildup of torque-on-bit (TOB), the drill-bit is released and "slips" beyond the prescribed rotary table speed. Stick-slip phenomenon is also detrimental to the drill-pipes, drill-bit, logging tools, and to the entire drilling operation as a whole.

Previous studies of torsional and axial vibrations that affect drillstring dynamics have shown the coupled nature of these two modes of vibrations. Yigit and Christoforou [1] examined the coupling between the axial and torsional vibrations using a simple model that adequately captures the dynamics, and used it to simulate the effects of varying operating conditions on stick-slip and bit-bounce interactions. The authors demonstrated that the conditions at the bit/formation interface, such as bit speed and formation stiffness, are major factors in shaping the dynamic response and due to the varying and uncertain nature of these conditions, simple operational guidelines or active rotary table control strategies are not sufficient to eliminate both stick-slip and bit-bounce. A proportional-derivative active controller was implemented to control both the axial hook load and the rotary table torque in order to suppress both bit-bounce, and stick-slip vibrations, respectively, providing smoother drilling over a wide range of conditions. Yigit and Christoforou [2] also investigated a fully coupled model for axial, lateral, and torsional vibrations of actively controlled drillstrings. The model included the mutual dependence of these vibrations that arises due to bit, formation and drillstring/borehole wall interactions as well as other geometric and dynamic non-linearities. The active control strategy was based on optimal state feedback control designed to control the drillstring rotational motion. It was demonstrated by simulation results that bit motion causes torsional vibrations, which in turn excite axial and lateral vibrations resulting in bit bounce and impacts with the borehole wall which was with close qualitative agreement with field observations regarding stick–slip and axial vibrations. Moreover, Yigit and Christoforou have also studied the coupled torsional and

bending vibrations of drillstrings subject to impact with friction [3] in addition to designing a linear quadratic regulator (LQR) controller [4] in order to regulate the torque supplied to the rotary table, and demonstrated its effectiveness in suppressing stick-slip oscillations once they are initiated. In general, active control approaches require response measurements be fed back to a controller to obtain actuator command signals. The length of the drillstring may introduce significant time delays in this process which are destabilizing for the control, and the cost and reliability of the required instrumentation may also be prohibitive. In contrast, the proposed PPMD is a totally passive device which does not require response measurements, control decisions, or actuation devices.

Khulief et al. [5] formulated a finite-element-model (FEM) for the drill-pipes and drill-collars of the drillstring that accounts for gyroscopics and axial-bending coupling via the gravitational force field using a Lagrangian approach in order to study the self-excited nature of stick-slip oscillations and bit-bounce. Explicit expressions of the finite element coefficient matrices were derived using a consistent mass formulation and the developed model is integrated into a computational scheme to calculate time-response of the drillstring system in the presence of stick–slip excitations. Sampaio et al. [6] presented a geometrically nonlinear model was presented to study the coupling of axial and torsional vibrations on a drillstring and the geometrical stiffening was analyzed using a nonlinear finite element approximation, in which large rotations and nonlinear strain-displacements are taken into account, in addition to the effect of structural

damping was also included in the model. It is to be mentioned that in references [1] to [6], the drillbit was of a roller cone type and the modeling of the interaction between the cutting action of the cones and the formation is explained in detail in Spanos et al. [7].

Roukema and Altintas [8] presented a time domain model of the torsional–axial chatter vibrations in drilling that considers exact kinematics of rigid body, and coupled torsional and axial vibrations of the drill. The tool was modeled as a pre-twisted beam that exhibits axial and torsional deflections due to torque and thrust loading, in which a mechanistic cutting force model was used to predict the cutting torque and thrust as a function of feed-rate, radial depth of cut, and drill geometry. The model considered nonlinearities in cutting coefficients, tool jumping out of cut and overlapping of multiple regeneration waves. The stability of the drilling process is also evaluated using the time domain simulation model, and compared with extensive experiments. Voronov et al. [9] analyzed the nonlinear dynamics of a tool commonly employed in deep hole drilling that is modeled as a two-degree of freedom system that vibrates in the axial and torsional directions as a result of the cutting process. The mechanical model of cutting forces is a nonlinear function of cutting tool displacement including state variables with time delay. The introduction of an absolute angle of rotation as the new independent variable, instead of time, increases the system dimension, but leads to a set of equations with constant delay. The Poincaré maps of state variables for various sets of operating conditions allow the prediction of conditions for stable continuous cutting and unstable regions and time domain simulation allows determination of the chip shape most suitable for certain workpiece material and tool geometry. Richard et al. [10] described a new

approach to understand the causes of stick-slip vibrations experienced by PDC bits. This new model takes into consideration not only the axial & torsional modes of vibrations, but also the coupling between these two modes through bit-rock interaction laws that account for both frictional contact & cutting processes at the bit-rock interface, and are formulated in terms of the depth of cut, a variable that brings into the equations the position of the bit at a previous a priori unknown time. The delayed and coupled nature of this interaction is ultimately responsible for the occurrence of self-excited vibrations that can degenerate under certain conditions. The features of the torsional vibrations that are predicted with this model were well in accordance with field observations. Richard, Germay, and Detournay [11] studied the self-excited stick–slip oscillations of a rotary drilling system with a drag bit, using a discrete model which takes into consideration the axial and torsional vibration modes of the bit. Both axial and torsional vibrations of the bit, as well as the coupling between the two vibration modes through the bit-rock interaction laws are considered as well as the interface laws that account both for cutting of the rock and for frictional contact between the cutter wearflats and the rock. The evolution of the system is governed by two coupled delay differential equations, with the delay being part of the solution, and by discontinuous contact conditions. Germay et al. [12] studied the dynamical response of a rotary drilling system with a drag bit, using a lumped parameter model that takes into consideration the axial and torsional vibration modes of the bit that are coupled through a bit-rock interaction law. At the bit-rock interface, the cutting process introduces a state-dependent delay, while the frictional process is responsible for discontinuous right-hand sides in the equations governing the

motion of the bit. This complex system is characterized by a fast axial dynamics compared to the slow torsional dynamics. A dimensionless formulation exhibits a large parameter in the axial equation, enabling a two-time-scales analysis that uses a combination of averaging methods and a singular perturbation approach. The analytical expression of the solution of the axial dynamics is used to derive an approximate analytical expression of the velocity weakening friction law related to the physical parameters of the system, and can be used to provide recommendations on the operating parameters in order to reduce the amplitude of the torsional vibrations.

In common practice, conventional impact shock absorbers are fitted in the BHA above the drillbit in an attempt to mitigate or suppress axial vibrations due to bit-bounce but sometimes these devices can exacerbate the vibration problems [13-17]. In this case, the driller is left with no other choice other than to decrease the WOB and ROP that adds cost to the drilling operation. APS Technology has developed an active magnetorheological (MR) three-axis damper [18-20] whose hardness can be adjusted continuously to accommodate changing operational and downhole environmental conditions. The active MR damper has demonstrated reduced levels of axial vibrations that lead to more efficient and economical drilling. Elsayed & Aissi [21] also conducted a laboratory study using an MR damper manufactured by Lord Corporation [22] in which a shock absorber was tuned to mitigate bit-bounce. Baker Hughes Inc developed a thruster assembly to be fitted above the drillbit in order to eliminate axial vibrations by hydraulically controlling WOB [23]. In this study, Schmalhorst [23] highlights that

conventional vibration control devices, such as shock absorbers do potentially offer the ability to decouple the bit from the drillstring, thereby removing a prime excitation source, they fail to maximize drilling efficiency. In addition, while shock absorbers may improve axial vibrations they often aggravate lateral vibrations. Also, analysis of downhole and surface-measured data indicates that incorrectly rated shock absorbers may cause significant bit and drillstring damage.

Mongkolcheep et al [24] presented a methodology to predict lateral vibrations of drilllstrings by of a flexible drill collar utilizing a modal coordinate condensed, finite element approach. The nonlinear effects of drillstring / borehole contact, friction and quadratic damping were included. Bifurcation diagrams were presented to illustrate the effects of speed, friction, stabilizer gap and drill collar length on chaotic vibration response. A study that considered the length of time to steady state, the number and duration of linearization sub-intervals, the presence of rigid body modes and the number of finite elements and modal coordinates, was conducted on factors for improving the accuracy of Lyapunov Exponents to predict the presence of chaos. Yigit and Christoforou [25] employed an Euler-Bernoulli beam, assumed modes model to study the coupling of axial and lateral vibrations. The impact of the drillstring with the borehole wall was modeled using Hertzian contact theory. The coupling of the vibrations yielded a value of the critical axial load lower than the one obtained from a linear analysis and resulted in chaotic response.

Flywheel systems with magnetic suspensions for energy storage have found wide applications in both military and commercial applications. Active magnetic bearings (AMB) provide a novel, efficient and effective means for levitating and stabilizing high-speed rotordynamic systems in many applications. The capability of reacting to applied loads, such as inertia, maneuver or imbalance, as well as the adaptability to changing operating conditions in a wide range of environments derives significant benefits as compared with rolling element bearings. G. Sun et al [26] conducted numerical simulations of a rotor drop on catcher bearings in flywheel energy storage system with a detailed CB model which includes a Hertzian load–deflection relationship between mechanical contacts, speed-and preload-dependent bearing stiffness due to centrifugal force, and a Palmgren's drag friction torque. Catcher bearings provide backup protection for rotating machines with AMBs, and are required in the event of an AMB failure or high transient loads. The transient simulation results illustrated the rotor shaft response variations with the design parameters: shaft/ bearing friction coefficients, axial preload, support damping of damper liner, and side loads from magnetic bearings. The results revealed that the friction coefficients, support damping, and side loads are critical parameters to satisfy catcher bearing design objectives and prevent backward whirl. Park & Palazzolo [27] provided theory and simulations for MIMO active vibration control for satellite integrated power transfer and attitude control via four, variable speed flywheels that potentially provide the energy storage and attitude control functions of existing batteries and control moment gyros on a satellite. The assumption of rigidity in the flywheel's bearings and the satellite structure was eliminated utilizing control algorithms

for active vibration control, flywheel shaft levitation, and integrated power transfer and attitude control that were effective even with low stiffness AMBs and flexible satellite appendages. The flywheel active vibration control and levitation tasks were provided by a multiple input–multiple output control law that enhances stability by reducing the dependence of the forward and backward gyroscopic poles with changes in flywheel speed. The control law was shown to be effective even for large polar to transverse inertia ratios, which increased the stored energy density while causing the poles to become more speed dependent, and for low bandwidth controllers shaped to suppress high frequency noise. Notch, low-pass, and bandpass filters were implemented in the AMB system to reduce and cancel high frequency, dynamic bearing forces and motor torques due to flywheel mass imbalance. Lei and Palazzolo [28] presented an approach for the analysis and design of magnetic suspension systems with large flexible rotordynamics models including dynamics, control, and simulation. The objective was to formulate and synthesize a large-order, flexible shaft rotordynamics model for a flywheel supported with magnetic bearings. A finite element model of the rotor system was assembled and then employed to develop a magnetic suspension compensator to provide good reliability and disturbance rejection. The large number of flexible modes and speed dependent modes made the controller development particularly challenging. Stable operation over the complete speed range and optimization of the closed-loop rotordynamic properties were obtained via synthesis of eigenvalue analysis, Campbell plots, waterfall plots, and mode shapes. A flywheel system was studied as an example for realizing a physical controller that provides stable rotor suspension and good

disturbance rejection in all operating states. The baseline flywheel system control was determined from extensive rotordynamics synthesis and analysis for rotor critical speeds, mode shapes, frequency responses, and time responses. The flywheel system supported by active magnetic bearings demonstrated the properties of robustness to the standard sensor runout patterns, mass imbalances and inertial load impact. The coil peak voltages were within the specific limits for the selected power amplifiers with adequate margin against clipping, and the peak vibration was suppressed within the catcher bearing gaps for the given runout and imbalance disturbances. The reader is referred to references [29] to [44] for extended literature on magnetic bearings and their applications.

1.3 Objectives

Hence in this work, a passive proof mass damper (PPMD) is presented that has the ability to mitigate and completely suppresses downhole lateral, axial and torsional vibrations, over a wide range of operating conditions, in order to maintain a constant ROP. Viguié and Kerschen [45] have proposed a similar device but it only addresses torsional vibrations since it doesn't consider the axial degree of freedom. The advantages of this PPMD are that, it is easy to fabricate and integrate into the BHA, inexpensive to manufacture and install, doesn't require any supervisory control from the top, and suppresses the vibrations at the source and downhole. Moreover, since it is a passive device, it doesn't require telemetry of vibration data to the top of the drill-rig in order to pursue complete vibration control.

Moreover, a novel conceptual downhole flywheel design is presented that serves as an alternative solution to existing lithium-ion batteries. The flywheel rotor is levitated by AMBs and the objective is to design a stable and robust closed-loop control system that maintains levitation despite the violent different types of downhole vibrations. It will also be demonstrated that the proposed flywheel module can mitigate downhole vibrations, in addition to its original energy storage function.

1.4 Statement of Contributions

The dissertation provides five major contributions:

1) Development and verification an effective and comprehensive methodology to suppress downhole (BHA) bit bounce vibrations by use of a passive mass-proof-damper using practical and effective methods of modeling, simulation, and design guidelines.
2) Development and verification an effective and comprehensive methodology to maintain levitation of a high speed, magnetically levitated, energy storage flywheel installed in a BHA, and subjected to its natural vibration environment including self-excited and externally forced motion.
3) Extend the system capabilities in (2) to also suppress BHA natural vibrations by use of the flywheel inertia and magnetic suspension designs.
4) Develop improved mathematical based approaches to reduce the simulation time for modeling drillstring bit bounce vibration and its suppression as described in (1) - (3) .

5) Enhance the drillstring dynamics model to account for the lateral vibration instability driver due to the self-excited stick-slip-bit-bounce phenomenon, and hence spotlighting a mutual dynamic coupling between the lateral, axial and torsional modes.

2. FLYWHEEL DESIGN AND MAGNETIC LEVITATION

2.1 Design Constraints and Objectives

Flywheels are kinetic energy storage devices, and store energy in a rotating mass (rotor), with the amount of stored energy (capacity) dependent on the mass and form (inertia), and rotational speed of the rotor. In order to initiate the proposed design of the flywheel that is to be embedded in the BHA, one must consider both the geometric and downhole environmental constraints. The BHA is the heaviest portion of the drillstring and it consists of several heavy drillcollar sections, in addition to the logging/measurement tools and the drillbit. The drillcollar sections are slightly smaller in diameter than that of the drillbit whose diameter determines the size of borehole of the well. Thus, the outer diameter of the container enclosing the flywheel must not exceed the outer diameter of the drillcollars. The drilling process requires a minimum amount of mud flowrate in order to lubricate the drillbit and clean the shavings, and hence the inner diameter of the drillcollar must permit such flowrate. Therefore, the inner diameter of the container enclosing the flywheel must be at least equal to the inner diameter of the drillcollar. The harsh environmental constraints require that the flywheel module sustains extreme high temperature and pressure. Thus, the thickness of the container enclosing the flywheel must sustain pressures as high as 30 kpsi. Inside its enclosure, the flywheel shall be suspended on a five-axis magnetic bearing system that continues to maintain levitation when the BHA is subjected to the harshest downhole vibrations. The flywheel should also provide 1 – 2 kW.hr of energy that existing lithium-ion batteries currently provide. Thus, in the following sections, the conceptual schematic design, a

step-by-step sizing procedure, and AMB levitation closed-loop control system are presented.

2.2 Flywheel Conceptual Design and Sizing

Given the geometric constraints of the problem, the containment vessel is comprised of two parts: an outer container pipe whose outer diameter is exposed to the borehole and inner container pipe whose inner diameter is exposed to the mud-flow. In between the inner and outer containers, the hollow flywheel rotor is enclosed. Since the high performance flywheels operate at very high speeds exceeding 20,000 rpm, the rotor shall be supported on active magnetic bearings and placed in a vacuum space to eliminate aerodynamic drag and reduce magnetic bearing winding losses. Figure 2.1 shows an exploded view of the design concept. The rotor is to be levitated by two radial and a thrust (axial) AMBs installed on the inner container and hence providing five-axis magnetic levitation. A similar inside-out configuration has been previously proposed by Lei and Palazzolo [28]. The rotor is spun by a motor/generator assembly also installed on the inner container pipe. An accelerating torque (motor mode) causes the flywheel rotor to speed up and store energy, while a decelerating torque (generator mode) causes the flywheel rotor to slow down and regenerate energy.

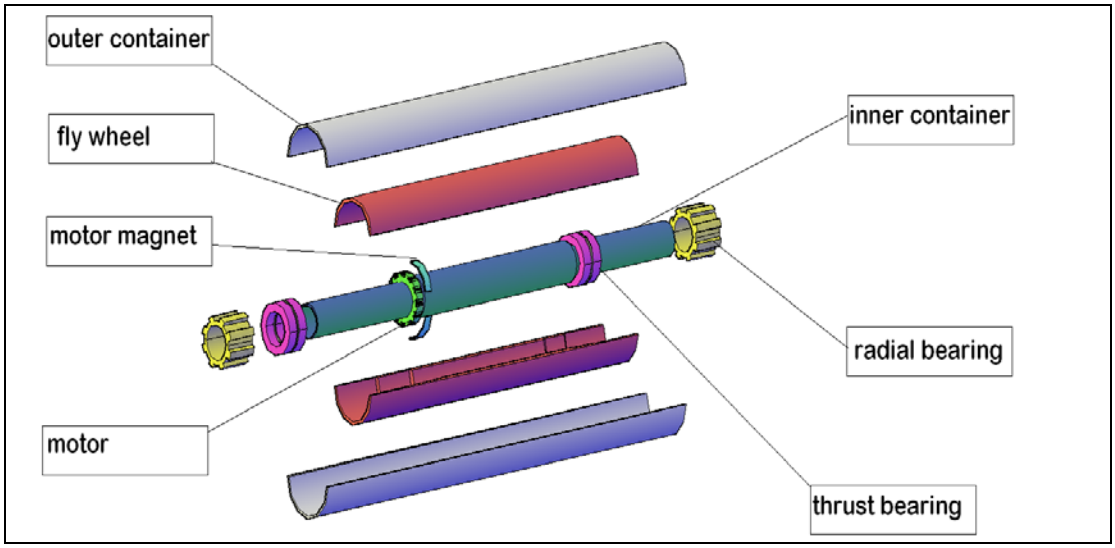

Figure 2.1: Exploded Schematic View of the Proposed Downhole Flywheel Concept

The maximum downhole pressure determines the thickness of both the inner and outer container pipes based on the "pressure-vessel-equation":

$$t_{pipe} = \frac{P_{\max}.D_i}{2\sigma_{\max}} \tag{2.1}$$

where

$\boldsymbol{P_{max}}$ is the maximum downhole pressure

$\boldsymbol{D_i}$ is the inner diameter of the pipe

$\boldsymbol{\sigma_{max}}$ is the permissible radial normal stress in the pipe

The maximum speed of the flywheel is determined by the permissible hoop normal stress, $\boldsymbol{\sigma_\theta}$ according to [43]:

$$\sigma_\theta = \frac{3+\upsilon}{8}\left(r_{fi}^{\ 2} + r_{fo}^{\ 2} - \frac{1+3\upsilon}{3+\upsilon} r^2 + \frac{r_{fi}^2 . r_{fo}^2}{r^2} \right) \rho.\omega_f^{\ 2} \tag{2.2}$$

where

υ is Poisson's ratio

r_{fi} is the inner flywheel radius

r_{fo} is the outer flywheel radius

ρ is the material density

ω_f is the flywheel spin velocity

Taking into consideration the spacing required to install the AMBs, the flywheel outer diameter will be smaller than inner diameter of the outer container, and the flywheel inner diameter will be greater than the outer diameter of the inner container.

The kinetic energy stored, E, in the flywheel is given as:

$$E = \frac{1}{2} J_f . \left(\omega_{\max}^2 - \omega_{\min}^2 \right) \tag{2.3}$$

where

J_f is the polar moment of inertia of the flywheel

ω_{max} is the maximum spin velocity of the flywheel

ω_{min} is the minimum spin velocity of the flywheel

The spin velocity variation of the flywheel implies that by taking into consideration Equation 2.2, there will be a cyclic load on the flywheel rotor. Hence the spin speed limit must take fatigue into consideration, and according to the ASME elliptical equation [43]:

$$\sqrt{\left(\frac{S_a}{S_e}\right)^2+\left(\frac{S_m}{S_y}\right)^2}=\frac{1}{\text{FOS}} \tag{2.4}$$

where

$\boldsymbol{S_a}$ is the alternating stress

$\boldsymbol{S_e}$ is the endurance strength of the material

$\boldsymbol{S_m}$ is the mean stress

$\boldsymbol{S_y}$ is the yield strength of the material

FOS is the factor of safety

Thus the sizing procedure can be summarized as follows:

a. Define the geometric constraints. The outer diameter of the BHA is the outer diameter of the flywheel enclosure (outer diameter of the outer container) and the mud-flow diameter is its inner diameter (inner diameter of the inner container).
b. Given the downhole pressure, calculate the thicknesses of the inner and outer containers, and thus determine the inner diameter of the outer container and the outer diameter of the outer container using Equation 2.1.
c. Determine the inner and outer diameters of the flywheel after accounting for the space required for the AMBs. The flywheel inner diameter is slightly greater than the outer diameter of the inner container and the flywheel outer diameter is slightly smaller than the inner diameter of the outer container.

d. Using Equations 2.2 and 2.4, determine the maximum spin speed of the flywheel. It is recommended in most common practices that the minimum spin speed to be one third of the maximum [41].
e. With the knowledge of the energy storage requirement, evaluate the polar inertia of the flywheel using Equation 2.3, and hence also determining its mass, and length.

2.3 Active Magnetic Bearings and Magnetic Levitation Control

Since ball bearings cannot sustain the dynamic load due to the high spinning speed of the flywheel rotor, and in addition to the expected associated friction losses, the flywheel rotor is to be suspended on magnetic bearings. Figure 2.2 shows the block diagram of the closed-loop control system for the proposed magnetic levitation. The system comprises a proportional-integral-derivative (PID) controller, power amplifier, magnetic bearings, position sensors and additional filters if necessary.

The PD controller consists of 2 transfer function G_1 and G_2. G_1 is the proportional path transfer function and is defined as:

$$G_1(s) = \frac{G_p}{\tau_c s + 1} \tag{2.5}$$

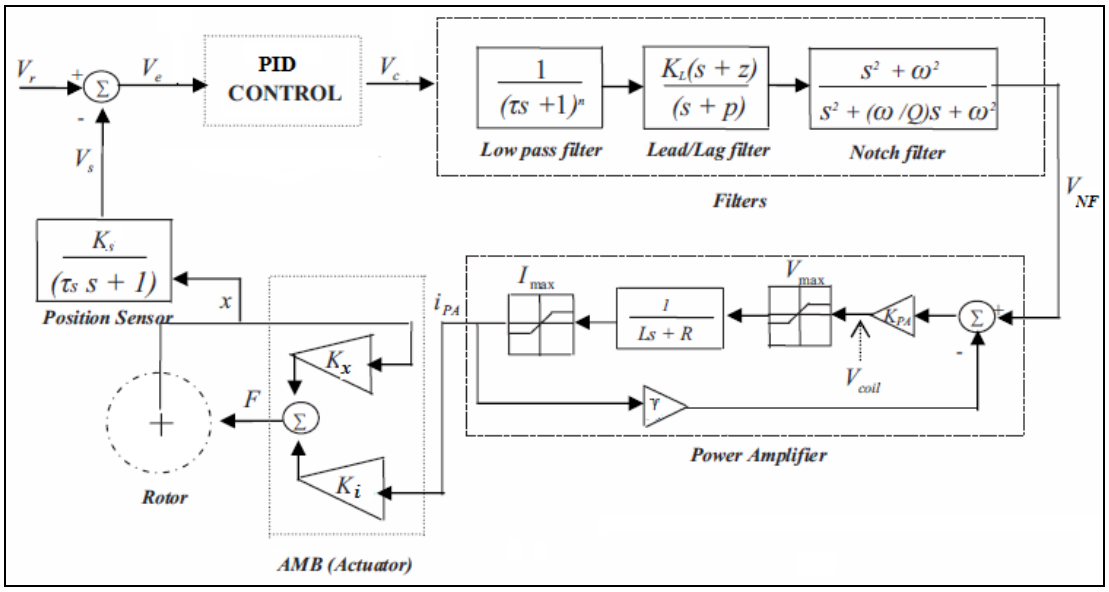

Figure 2.2: Magnetic Levitation Control System

Meanwhile, the derivative path transfer function, G_2 is defined as:

$$G_2(s) = \frac{G_d s}{(\tau_c s + 1)^2} \tag{2.6}$$

The overall transfer function G_{PD} is the summation of G_1 and G_2 and is given as:

$$G_{PD}(s) = \frac{\left(\frac{G_d}{\tau_c^2} + \frac{G_p}{\tau_c}\right)s + \frac{G_p}{\tau_c^2}}{s^2 + \frac{2}{\tau_c}s + \frac{1}{\tau_c^2}} \tag{2.7}$$

The state-space representation of the PD controller is:

$$\begin{aligned} \dot{x}_{PD} &= \mathrm{A}_{PD} x_{PD} + \mathrm{B}_{PD} e \\ v_{PD} &= \mathrm{C}_{PD} x_{PD} \end{aligned} \tag{2.8}$$

$$\mathrm{A}_{PD}=\begin{bmatrix} -\frac{2}{\tau_c} & -\frac{1}{\tau_c^2} \\ 1 & 0 \end{bmatrix} \quad , \quad \mathrm{B}_{PD}=\begin{bmatrix} 1 \\ 0 \end{bmatrix} \quad , \quad \mathrm{C}_{PD}=\begin{bmatrix} \left(\frac{G_d}{\tau_c^2}+\frac{G_p}{\tau_c}\right) & \frac{G_p}{\tau_c^2} \end{bmatrix} \tag{2.9}$$

The power amplifier transfer function G_{PA} is defined as:

$$G_{PA}(s)=\frac{k_{PA}}{Ls+(R+\gamma k_{PA})} \tag{2.10}$$

The state-space representation of the power amplifier is given as:

$$\begin{aligned} \dot{x}_{pai} &= \mathrm{A}_{PA}x_{pai}+\mathrm{B}_{PA}v_{nfi} \\ i_{pai} &= \mathrm{C}_{PA}x_{pai} \end{aligned} \tag{2.11}$$

$$\mathrm{A}_{PA}=-\frac{(R+\gamma k_{PA})}{L} \quad , \quad \mathrm{B}_{PA}=1 \quad , \quad \mathrm{C}_{PA}=\frac{k_{PA}}{L} \tag{2.12}$$

The voltage and current saturation can be both applied by considering the feedback equation with reference to Figure 2.2:

$$v_{PA}=k_{PA}.(v_{NF}-\gamma.i) \tag{2.13}$$

The lag/lead Compensator transfer function G_{LC} is defined as:

$$G_{LC}(s)=K_L\frac{(s+z)}{(s+p)} \tag{2.14}$$

$$\begin{aligned} \dot{x}_{LC} &= \mathrm{A}_{LC}x_{LC}+\mathrm{B}_{LC}v_{PD} \\ v_{LC} &= \mathrm{C}_{LC}x_{LC}+\mathrm{D}_{LC}v_{PD} \end{aligned} \tag{2.15}$$

where

$$\mathrm{A}_{LC} = -p \quad , \quad \mathrm{B}_{LC} = 1 \quad , \quad \mathrm{C}_{LC} = K_L(z-p) \quad , \quad \mathrm{D}_{LC} = K_L \tag{2.16}$$

The notch filter transfer function is given as:

$$G_{NF}(s) = \frac{s^2 + \omega_f^2}{s^2 + \frac{\omega_f}{Q}s + \omega_f^2} \tag{2.17}$$

The state-space representation is defined as:

$$\begin{aligned} \dot{x}_{NF} &= \mathrm{A}_{NF} x_{NF} + \mathrm{B}_{NF} v_{LC} \\ v_{NF} &= \mathrm{C}_{NF} x_{NF} + \mathrm{D}_{NF} v_{LC} \end{aligned} \tag{2.18}$$

where

$$\mathrm{A}_{NF} = \begin{bmatrix} \frac{-\omega_f}{Q} & -\omega_f^2 \\ 1 & 0 \end{bmatrix} \quad , \quad \mathrm{B}_{NF} = \begin{bmatrix} 1 \\ 0 \end{bmatrix} \quad , \quad \mathrm{C}_{NF} = \begin{bmatrix} \frac{-\omega_f}{Q} & 0 \end{bmatrix} \quad , \quad \mathrm{D}_{NF} = 1 \tag{2.19}$$

The equation of motion of the rotordynamic system is given as:

$$\mathrm{M}\ddot{\mathrm{X}} + \mathrm{C}\dot{\mathrm{X}} + \mathrm{KX} = f_m + f_{nm} \tag{2.20}$$

Thus, the state-space format representing the rotor is defined as:

$$\begin{aligned} \dot{w}_R &= \mathrm{A}_R w_R + \mathrm{B}_R f_{nm} + \mathrm{B}_m f_m \\ y_S &= \mathrm{C}_R w_R \end{aligned} \tag{2.21}$$

It is assumed that the active magnetic bearing actuator and sensor are located at the same nodal position. The actuating force of the magnetic bearing is given by:

$$f_m = -K_i i_{pa} - K_x y_s \tag{2.22}$$

The system is connected in series, and so the output of one system is the input to the other. Starting at the PD-controller, its output voltage is the input to the lag/lead compensator and so by substituting

$$\begin{aligned} \dot{x}_{LC} &= \mathrm{A}_{LC} x_{LC} + \mathrm{B}_{LC} \mathrm{C}_{PD} x_{PD} \\ v_{LC} &= \mathrm{C}_{LC} x_{LC} + \mathrm{D}_{LC} \mathrm{C}_{PD} x_{PD} \end{aligned} \tag{2.23}$$

Feeding the output of the lag/lead compensator to the notch filter yields:

$$\begin{aligned} \dot{x}_{NF} &= \mathrm{A}_{NF} x_{NF} + \mathrm{B}_{NF} \mathrm{C}_{LC} x_{LC} + \mathrm{B}_{NF} \mathrm{D}_{LC} \mathrm{C}_{PD} x_{PD} \\ v_{NF} &= \mathrm{C}_{NF} x_{NF} + \mathrm{D}_{NF} \mathrm{C}_{LC} x_{LC} + \mathrm{D}_{NF} \mathrm{D}_{LC} \mathrm{C}_{PD} x_{PD} \end{aligned} \tag{2.24}$$

Feeding the output of the notch filter to the power amplifier yields:

$$\begin{aligned} \dot{x}_{PA} &= \mathrm{A}_{PA} x_{PA} + \mathrm{B}_{PA} \mathrm{C}_{NF} x_{NF} + \mathrm{B}_{PA} \mathrm{D}_{NF} \mathrm{C}_{LC} x_{LC} + \mathrm{B}_{PA} \mathrm{D}_{NF} \mathrm{D}_{LC} \mathrm{C}_{PD} x_{PD} \\ i_{PA} &= \mathrm{C}_{PA} x_{PA} \end{aligned} \tag{2.25}$$

The output current activates the actuator magnetic force, thus:

$$\begin{aligned} \dot{w}_R &= \mathrm{A}_R w_R + \mathrm{B}_R \mathrm{C}_{PA} x_{PA} - \mathrm{B}_m \left(\mathrm{K}_i i_{pa} + \mathrm{K}_x y_s \right) \\ y_S &= \mathrm{C}_R w_R \end{aligned} \tag{2.26}$$

The position sensor converts the nodal displacements to voltages, and hence:

$$\begin{aligned} \dot{x}_{PS} &= \mathrm{A}_{PS} x_{PS} + \mathrm{B}_{PS} \mathrm{C}_R w_R \\ v_{PS} &= \mathrm{C}_{PS} x_{PS} \end{aligned} \tag{2.27}$$

The error fed into the controller is given by:

$$e(t) = v_R(t) - v_{PS}(t) \tag{2.28}$$

where $v_R(t)$ is the reference control voltage (usually set equal to zero)

But $v_{PS} = C_{PS} x_{PS}$ (2.29)

Thus:

$$e(t) = v_R(t) - C_{PS} x_{PS} \tag{2.30}$$

The overall integrated state-space representation of the system is obtained by augmenting all the states of all existing components, and hence by defining the system state vector as:

$$\mathrm{X} = \left\{ w_R \quad x_{PD} \quad x_{LC} \quad x_{NF} \quad x_{PA} \quad x_{PS} \right\}^T$$

The state-space representing the system can be written as:

$$\dot{\mathrm{X}} = \mathrm{A}_X \mathrm{X} + \mathrm{B}_{AMB} v_R + \mathrm{B}_{EXT} f_R \tag{2.31}$$

where

$$\mathrm{A}_X = \begin{bmatrix} \mathrm{A}_R - \mathrm{B}_m \mathrm{K}_x \mathrm{C}_R & \underline{\mathrm{O}} & \underline{\mathrm{O}} & \underline{\mathrm{O}} & -\mathrm{B}_m \mathrm{K}_i \mathrm{C}_{PA} & \underline{\mathrm{O}} \\ \underline{\mathrm{O}} & \mathrm{A}_{PD} & \underline{\mathrm{O}} & \underline{\mathrm{O}} & \underline{\mathrm{O}} & -\mathrm{B}_{PD} \mathrm{C}_{PS} \\ \underline{\mathrm{O}} & \mathrm{B}_{LC} \mathrm{C}_{PD} & \mathrm{A}_{LC} & \underline{\mathrm{O}} & \underline{\mathrm{O}} & \underline{\mathrm{O}} \\ \underline{\mathrm{O}} & \mathrm{B}_{NF} \mathrm{D}_{LC} \mathrm{C}_{PD} & \mathrm{B}_{NF} \mathrm{C}_{LC} & \mathrm{A}_{NF} & \underline{\mathrm{O}} & \underline{\mathrm{O}} \\ \underline{\mathrm{O}} & \mathrm{B}_{PA} \mathrm{D}_{NF} \mathrm{D}_{LC} \mathrm{C}_{PD} & \mathrm{B}_{PA} \mathrm{D}_{NF} \mathrm{C}_{LC} & \mathrm{B}_{PA} \mathrm{C}_{NF} & \mathrm{A}_{PA} & \underline{\mathrm{O}} \\ \mathrm{B}_{PS} \mathrm{C}_R & \underline{\mathrm{O}} & \underline{\mathrm{O}} & \underline{\mathrm{O}} & \underline{\mathrm{O}} & \mathrm{A}_{PS} \end{bmatrix}$$

$$B_{AMB} = \begin{bmatrix} \underline{O} \\ B_{PD} \\ \underline{O} \\ \underline{O} \\ \underline{O} \\ \underline{O} \end{bmatrix} \quad , \quad B_{EXT} = \begin{bmatrix} B_R \\ \underline{O} \\ \underline{O} \\ \underline{O} \\ \underline{O} \\ \underline{O} \end{bmatrix} \tag{2.32}$$

Define the outputs to be the nodal displacements where the sensors are located, and hence:

$$y_S = \begin{bmatrix} C_R & \underline{O} & \underline{O} & \underline{O} & \underline{O} & \underline{O} \end{bmatrix} X \tag{2.33}$$

3. MODELING OF DRILLSTRING DYNAMICS

3.1 Lumped System Modeling

Figure 3.1 illustrates the main components of a drilling rig and Figure 3.2 shows a simplified schematic.

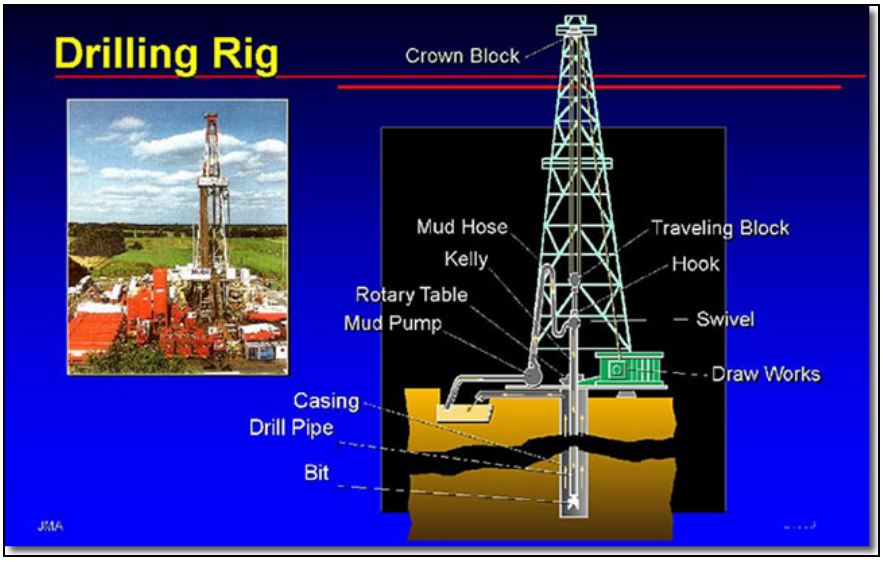

Figure 3.1: Main Components of a Drilling Rig

Figure 3.3 illustrates a schematic of the drillsting and BHA. The system is modeled as a lumped system having 2 degrees of freedom (DOF), axial and torsional [10-12]. Since the weight of the drillpipes are generally much smaller than that of the drillcollars (BHA), the drillpipe is replaced by an equivalent torsional spring and damper that connect the BHA to the rotating top drive at the surface of the drilling rig.

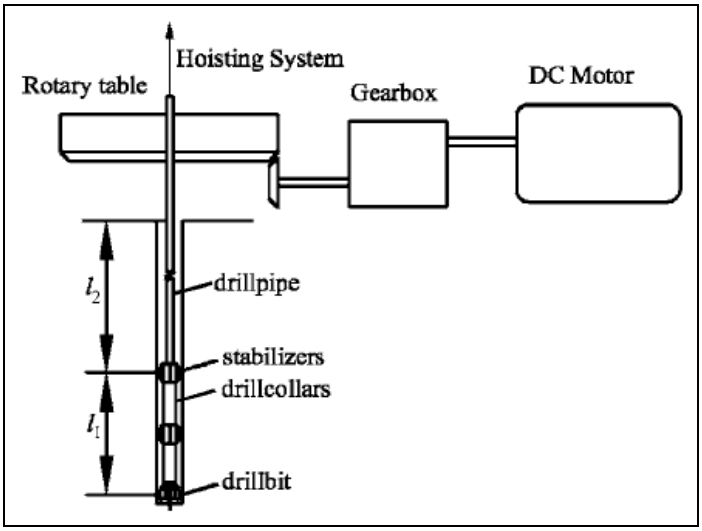

Figure 3.2: Schematic of Drillstring Components

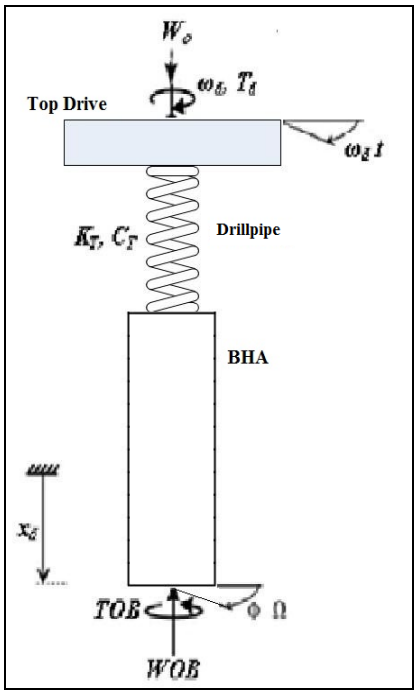

Figure 3.3: Schematic of the BHA/Drillstring with External Forces

When a drillbit is penetrating a rock formation, a reaction force and torque are generated and known as weight-on-bit (WOB) and torque-on-bit (TOB), respectively. The WOB and TOB will be explained in detail in the next section.

The torsional equation of motion is given as:

$$J\ddot{\phi} + C_T\dot{\phi} + K_T\phi = T_d - \text{TOB} \tag{3.1}$$

where

$$T_d = K_T.\omega_d.t \tag{3.2}$$

The axial equation of motion is given as:

$$m_{DC}\ddot{x}_d = W_0 - \text{WOB} \tag{3.3}$$

If the BHA has a mass unbalance, then there will also be a lateral motion, adding an extra 2 DOFs to the lumped-mass model, and if the resulting radial motion is greater than the wellbore-BHA clearance, then there will be contact with the wellbore. Figure 3.4 shows a schematic of the lateral motion of the BHA and wellbore contact.

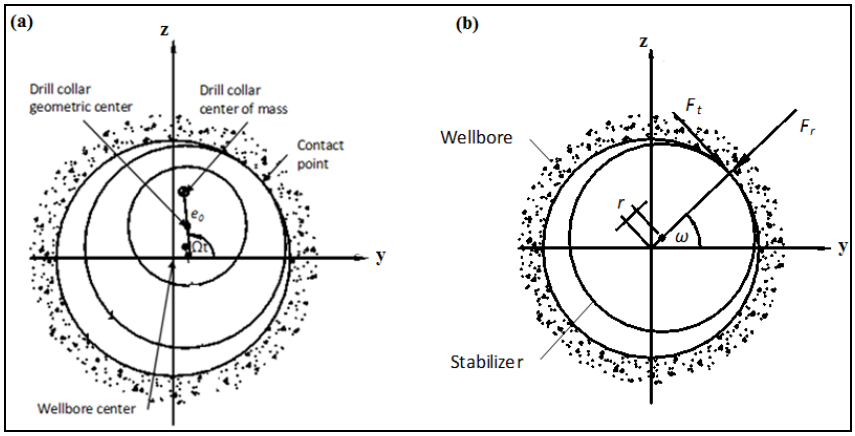

Figure 3.4: Lateral Motion Due to Mass Unbalance (a) & Contact Forces (b) [21]

The lateral forces due to mass unbalance are given as:

$$F_y = m_{DC}.e_0.\omega_d^2.\cos\omega_d.t \tag{3.4}$$

$$F_z = m_{DC}.e_0.\omega_d^2.\sin\omega_d.t \tag{3.5}$$

The radial displacement of the geometric center of the BHA is given as:

$$r = \sqrt{y_d^2 + z_d^2} \tag{3.6}$$

There is contact between the BHA and the wellbore if the radial displacement is greater than or equal to the radial clearance, $\boldsymbol{r_c}$. Assuming a contact stiffness value of K_b, the normal reaction between the BHA and the wellbore can be written as:

$$F_r = -K_b.(r - r_c) \tag{3.7}$$

Assuming sliding friction between the BHA and the wellbore, the tangential friction force can be evaluated as:

$$F_t = -\mu_w.F_r.\mathrm{sgn}(\omega_c) \tag{3.8}$$

where ω_c is the angular rate of change of the BHA geometric position given as:

$$\omega_c = \frac{d}{dt}\left(\tan^{-1}\frac{z_d}{y_d}\right) = \frac{y_d.\dot{z}_d - z_d.\dot{y}_d}{r^2} \tag{3.9}$$

3.2 Drillbit Dynamics Modeling

Rock formation cutting and penetration is performed by a drillbit attached to the bottom of the BHA. There are two types of drillbits (Figure 3.5): polycrystalline-diamond-compact (PDC) and roller-cone. PDC drillbits are characterized by blades

whilst roller-cone drillbits are characterized by rotating cones that mesh in the center and the common type is the three-cone construction or tricone.

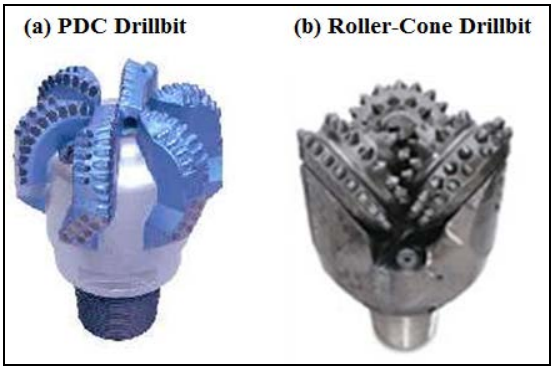

Figure 3.5: Types of Drillbits

For a PDC drillbit, the depth of cut per revolution per blade is given as:

$$d_n(t) = x_d(t) - x_d(t - t_n) \tag{3.10}$$

Hence, by assuming an equal depth of cut for all blades, the total depth of cut is given as:

$$d = n.d_n \tag{3.11}$$

where $\boldsymbol{t_n}$ is the instantaneous time delay obtained by solving the equation:

$$\phi(t) - \phi(t - t_n) = 2\pi / n \tag{3.12}$$

This time delay is an instability driver and resembles adding negative destabilizing damping to the system. The WOB and TOB both have cutting and friction components:

$$\text{WOB} = W_c + W_f \tag{3.13}$$

$$\text{TOB} = T_c + T_f \tag{3.14}$$

The expressions for the cutting components are given as [10 – 12]:

$$W_c = a.\xi.\varepsilon.d \tag{3.15}$$

$$T_c = \frac{a^2}{2}.\varepsilon.d \tag{3.16}$$

The friction components are given as:

$$W_f = a.l.\sigma \tag{3.17}$$

$$T_f = \frac{a^2}{2}.\gamma.l.\sigma.\mu \tag{3.18}$$

A Stribeck friction model is utilized and expressed as [1– 4]:

$$\mu = \mu_0.\left(\tanh\dot{\phi} + \frac{2.\dot{\phi}}{1+\dot{\phi}^2} + 0.01\dot{\phi}\right) \tag{3.19}$$

When the drill-bit loses contact with the formation during bit-bounce, the depth of cut, ***d***, is negative and the friction components vanish.

By substituting Equations 3.14 and 3.16 into Equation 3.1:

$$J\ddot{\phi} + C_T\dot{\phi} + K_T\phi + \frac{a^2}{2}.\varepsilon.n.x_d(t) = T_d - T_f + \frac{a^2}{2}.\varepsilon.n.x_d(t-t_n) \tag{3.20}$$

By substituting Equation 3.13 and 3.15 into Equation 3.3

$$m_d\ddot{x}_d + a.\xi.\varepsilon.n.x_d(t) = W_0 - W_f + a.\xi.\varepsilon.n.x_d(t-t_n) \tag{3.21}$$

With reference to Equation 3.21, the coefficient of $\boldsymbol{x_d}$ represents the stiffness of the formation that can be expressed as:

$$k_c = a.\zeta.\varepsilon.n \tag{3.22}$$

As can be seen from Equations 3.10 through 3.21, there is a complex coupling between the axial and torsional modes due to the reaction forces and torques between the PDC drillbit and the rock formation. The cutting reaction torque component is dependent on the axial depth of cut and the depth of cut per blade is dependent upon the rotation angle as described by Equation 3.12. This mutual coupling adds to the instability drivers of the system in addition to the time delay due to the cutting action of the blades of the PDC drillbit. This is similarly the case with roller-cone bits except that there is no time delay instability driver but the self-excitation is of sinusoidal nature. The WOB in the case of a roller-cone drillbit is given by [1-4]:

$$\text{WOB} = \begin{cases} k_c\left(x_d - s\right) & \text{if } x_d \geq s \\ 0 & \text{if } x_d < s \end{cases} \tag{3.23}$$

The formation surface elevation, ***s***, is given as:

$$s = s_0 . \sin b\phi \tag{3.24}$$

The torque-on-bit (TOB) is given as:

$$\text{TOB} = \text{WOB}.\left(\mu\left(\dot{\phi}\right) + \sqrt{\frac{d}{a}} \right).a \tag{3.25}$$

The depth of cut, d, in this case is given as:

$$d = \frac{2.\pi.\text{ROP}}{\omega_d} \tag{3.26}$$

The rate of penetration (ROP) is defined as:

$$\text{ROP} = c_1.W_0.\sqrt{\omega_d} + c_2 \tag{3.27}$$

The coupling between the axial and the torsional modes can be seen from Equations 3.23 through 3.25, and as in the case with the PDC drillbit the instability driver is self-excited. At steady-state, the axial penetration velocity of the BHA is equal to the ROP, and the drillbit spins at the same speed of the top drive at the surface. This implies that the WOB and TOB are equal to the applied force at the top of the rig, $\boldsymbol{W_o}$, and the driving torque, $\boldsymbol{T_d}$, respectively. When the TOB value is higher than the driving torque, the drillbit decelerates, and the drillbit can come to zero spinning velocity and this is known as sticking. As the top drive continues spinning whilst the drillbit is sticking, the drillpipe acts as a torsional spring storing potential energy that is suddenly released causing the drillbit to accelerate (or known as slipping) to two or even three times the top drive speed until it decelerates again and sticks, and the stick-slip cycle is repeated. If the normal reaction of the formation or WOB is greater than the applied axial force, $\boldsymbol{W_o}$, the drillbit loses contact with bottom of the wellbore, and the BHA is forced upward with negative velocity or conventionally known as bit-bounce. The weight of the BHA will bring it down again and drillbit-formation contact is reinstated and the cycle repeats itself. Figure 3.26 shows a reproduced example of combined stick-slip and bit-bounce from Yigit and Christoforou [1].

Hence, it is very crucial for drilling operators to estimate the stable operating region(s) in order to avoid stick-slip and bit-bounce vibrations, as this leads to inefficient drilling and detrimental damage to the drillpipes, BHA, and the logging tools. In the field, stick-slip is usually observed at low spin rates, especially with PDC drillbits since

the time delay value is higher meaning that there is a higher destabilizing equivalent negative damping. Bit-bounce occurs when the applied axial load from the top of the rig is not high enough to overcome the dynamic peak values of the WOB. Since the axial and torsional modes are dynamically coupled, a high fluctuating spin rate variation of the drillbit will likely cause a fluctuating ROP also leading to bit-bounce if the axial applied load, W_o, is not high enough.

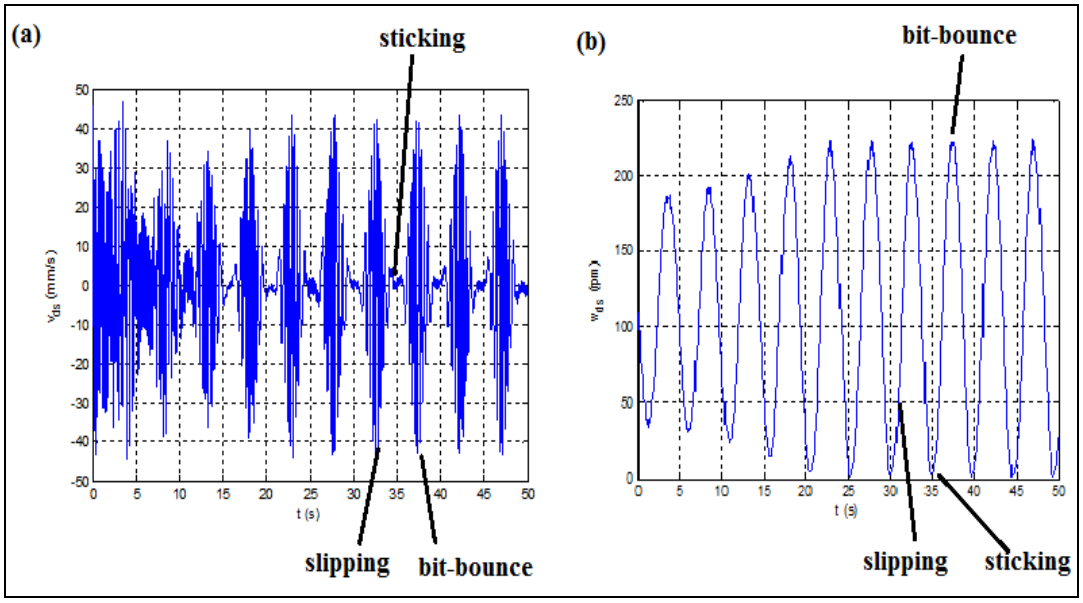

Figure 3.6: Illustration of Drillbit Sticking, Slipping, & Bit-Bounce

It is to be noted that Richard et al [10-11] utilized a constant Coulomb friction since previous experimental studies indicated that some PDC drillbit designs are rate-insensitive, i.e. do not possess a velocity-weakening Stribeck friction law. The study by Richard et al [10-11] concludes that stick-slip and bit-bounce vibrations are caused by the dynamic depth of cut that dominates the system. The following example illustrates

and validates the conclusion by Richard et al [10-11]. At first the top drive is spinning at 50 rpm and the response is evaluated by both a constant Coulomb friction and a Stribeck friction law. As can be clearly seen in Figure 3.7, the drillbit spin speed response obtained in both cases is almost identical. This scenario is repeated over and over again when the speed is raised to 65 rpm as shown in Figure 3.8.

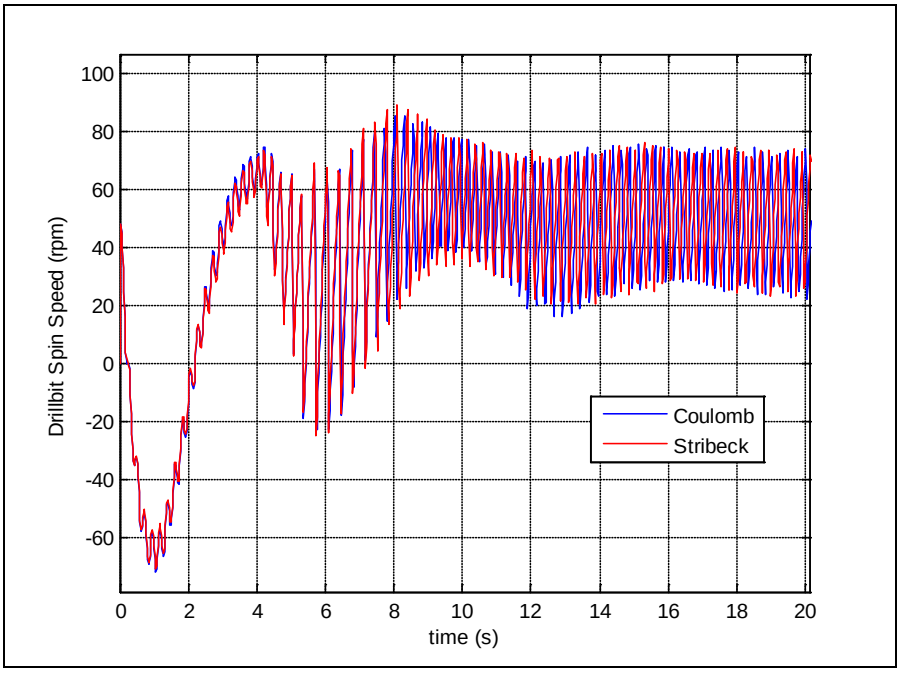

Figure 3.7: PDC Drillbit Spin Speed Obtained Utilizing Coulomb & Stribeck Friction (Top Drive Speed = 50 rpm)

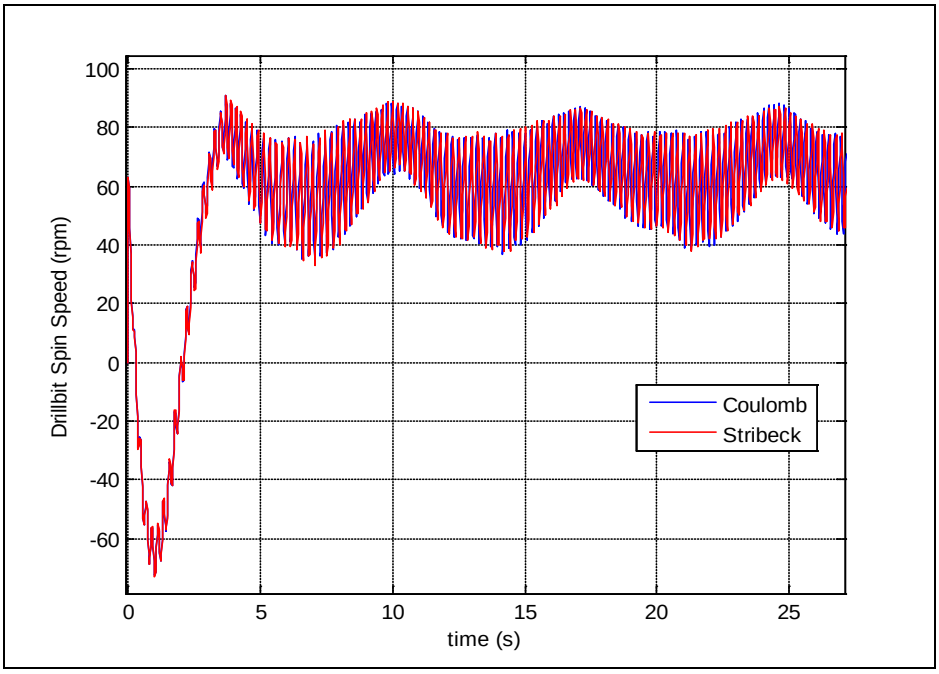

Figure 3.8: PDC Drillbit Spin Speed Obtained Utilizing Coulomb & Stribeck Friction (Top Drive Speed = 65 rpm)

3.3 Lateral-Axial-Torsional Coupling

As illustrated in the previous section, the drillbit-formation interaction induces a dynamic coupling between the axial and torsional modes of vibration. If the formation reaction or WOB is not purely axial but rather tilted with respect to the BHA longitudinal axis, there will be a lateral component of the WOB affecting the BHA and rotating with the drillbit as shown in Figure 3.9.

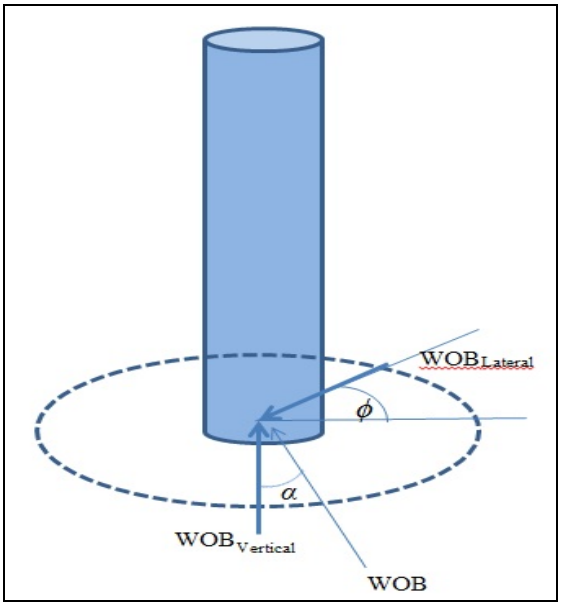

Figure 3.9: Illustration of Lateral WOB Component Action

This resembles the effect of centrifugal force due to unbalance but this lateral WOB component will rotate with the variable spin rate of the drillbit. If the inclination of the generated WOB with respect to the BHA is $\boldsymbol{\alpha}$, then the lateral component can be written as:

$$\mathrm{WOB}_{Lateral} = \mathrm{WOB}.\sin\alpha.e^{i\phi} \tag{3.28}$$

Thus, Equation (3.28) couples the lateral mode to both the axial and torsional modes due to this inclination of the WOB with respect to the BHA as a result of a misaligned drillbit or a bent housing utilized in deviated well drilling operations as shown in Figure 3.10. To the best of knowledge, this particular type of lateral-axial-torsional coupling identification, description and quantification has not been addressed before in the literature. Fu and Shi [47] presented a dynamic model to study the effects

of rotary speed, WOB, bent angle, and inclination on the dynamic characteristics of the BHA with bent housing using finite element theory. The work identified the effect of bent angle on relating the WOB to the lateral vibration but didn't consider the axial – torsional coupling of the drillbit cutting dynamics. Defourny and Abbassian [48] introduced a novel concept of a flexible PDC drillbit that reduced detrimental vibration associated with bit-tilt. The work identifies the nature of the axial – lateral coupling due to bit-tilt as well as the torsional – axial coupling due to the drillbit cutting dynamics but doesn't quantify the combined lateral-axial-torsional coupling. Other work in the literature includes a lateral-axial coupling that is similar to the buckling effect by assuming nonlinear coupling terms between the axial and torsional modes of non-rotating drillstrings as in Yigit and Christoforou [22], and also due to the axial stiffening effect as in Khulief et al. [5] based on the formula mentioned in Przemieniecki [49]. Buckling can be avoided in vertical and slightly deviated wells by installing stabilizers along the length of the drillstring and the axial stiffening effect is associated with very high modes of vibration that are unlikely to occur in the low-frequency dominated drillstring system.

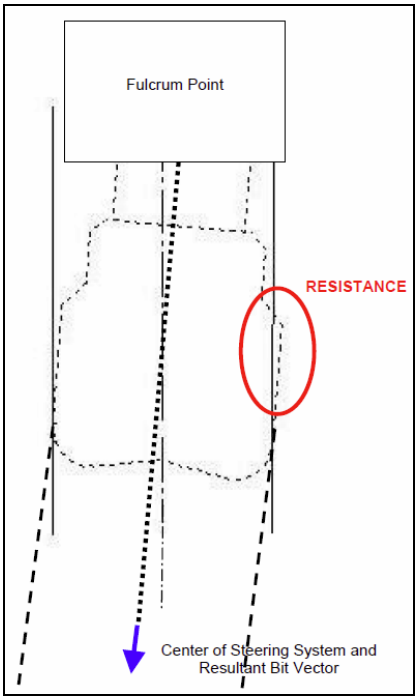

Figure 3.10: Steerable Drillbit in a Bent Housing Sub (National Oilwell Varco)

3.4 Passive Proof Mass Damper & Vibration Suppression

In order to passively attempt to suppress or mitigate the bit-bounce or stick-slip vibration, positive damping must be introduced to the system. In most common practice, the BHA is fitted with shock absorbers but sometimes this can exacerbate the vibration especially that the damping is not theoretically connected to the ground. An alternative is to add additional drill-collars to the BHA, and hence increasing the effective mass that adds more stability to the system. But this process will require the drilling operation to be halted in order to add the additional sections and thus increasing costs of operation. Hence, a passive proof-mass-damper (PPMD) is proposed that consists of a drillpipe

suspended on coils of springs and dampers that is embedded and connected to the BHA, similar to a dynamic absorber as shown in Figure 3.11.

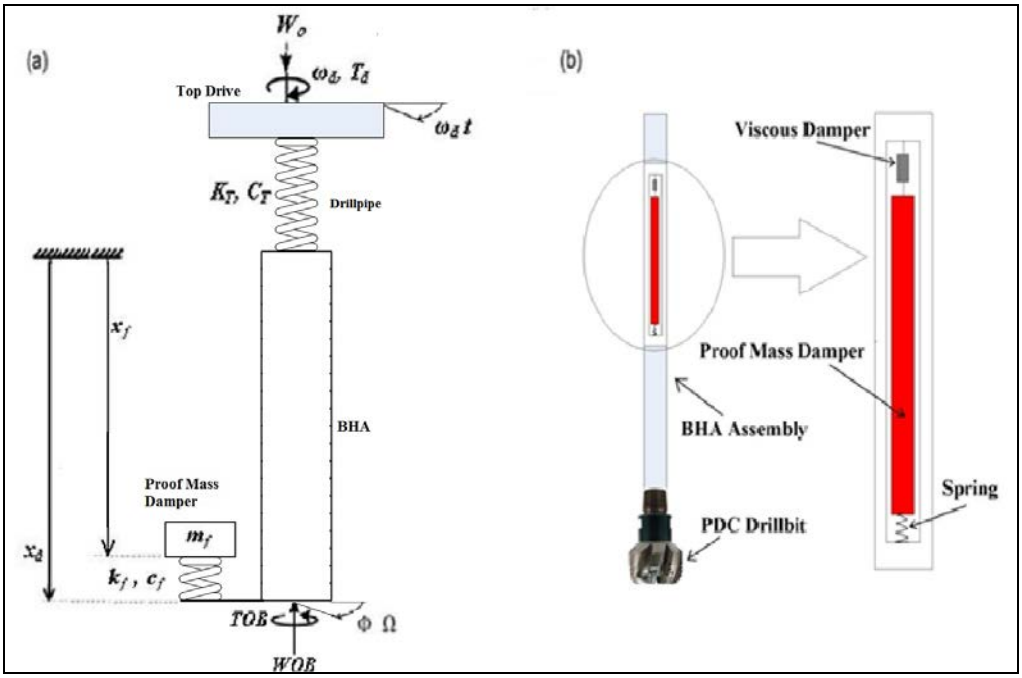

Figure 3.11: Illustration of the PPMD Embedded in the BHA

The addition of the PPMD will continuously suppress or mitigate the bit-bounce and torsional vibrations and thus the drilling operation wouldn't need to be interrupted to add additional drill-collar sections, and as will be illustrated in the results section, the PPMD mass is much smaller than the added sections in order to produce the same damping effect. After adding the PPMD, the equation of motion for the sprung mass is given as:

$$m_f.\ddot{x}_f + c_f(\dot{x}_f - \dot{x}_{DC}) + k_f.(x_f - x_d) = 0 \tag{3.29}$$

Hence the axial equation of motion of the BHA, if a PDC drillbit is utilized, after adding the PPMD is given as:

$$m_{DC}\ddot{x}_d + a.\xi.\varepsilon.n.x_d(t) = W_0 - W_f + a.\xi.\varepsilon.n.x_d(t-t_n) + c_f(\dot{x}_f - \dot{x}_d) + k_f.(x_f - x_d) \qquad (3.30)$$

If a torsional spring and damper denoted by $\boldsymbol{k_{fT}}$ and $\boldsymbol{c_{fT}}$, respectively, is attached to the PPMD, and if the PPMD inertia is denoted by $\boldsymbol{J_f}$, then the torsional equation of the PPMD can be written as:

$$J_f.\ddot{x}_f + c_{fT}(\dot{\phi}_f - \dot{\phi}) + k_{fT}.(\phi_f - \phi) = 0 \qquad (3.31)$$

Hence the torsional equation of motion of the BHA, if a PDC drillbit is utilized, after adding the PPMD is given as:

$$J\ddot{\phi} + C_T\dot{\phi} + K_T\phi + \frac{a^2}{2}.\varepsilon.n.x_d(t) = T_d - T_f + \frac{a^2}{2}.\varepsilon.n.x_d(t-t_n) + c_{fT}(\dot{\phi}_f - \dot{\phi}) + k_{fT}.(\phi_f - \phi) \qquad (3.32)$$

Figures 3.12 – 3.14 illustrates how the PPMD mitigates and suppresses bit-bounce. Consider a drillstring equipped with a PDC drillbit that is drilling a formation stiffness of 100 MN/m. When the top drive is spinning at 60 rpm, the bit bounces and there is no penetration as shown in Figure 3.12(a) and (b). By adding the PPMD, bit-bounce vibrations are reduced and stick-slip is initiated as shown in Figure 3.12(c) and (d). When the top drive spin speed increases to 70 rpm, before adding the PPMD there is still bit-bounce without penetration as shown in Figure 3.13(a) and 3.13(b), and with the PPMD there is stick-slip and bit-bounce with velocity peaks that are double that of the original BHA as shown in Figure 3.14(c) and (d). By increasing the top drive speed to 80

rpm, the original BHA is forced into severe stick-slip and bit-bounce as shown in Figure 3.14 (a) and (b), and by adding the PPMD penetration is achieved (Figure 3.14(c)) and there is minimal bit-bounce (Figure 3.14(d)) with minimal torsional oscillations. The drillbit spin speed before adding the PPMD is shown in Figure 3.15 when the top drive is rotating at 60, 70 and 80 rpm, and similarly, Figure 3.16 shows the drillbit spin speed at after adding the PPMD.

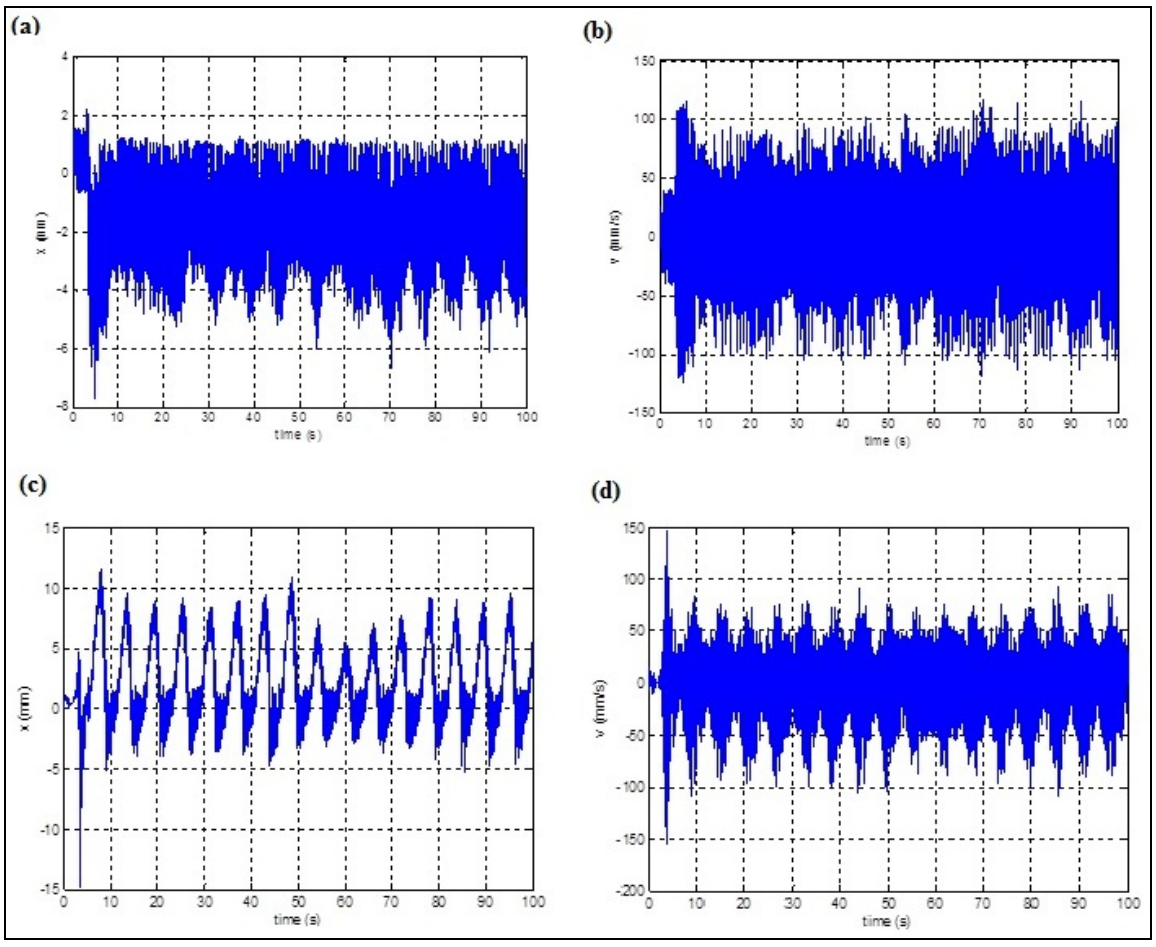

Figure 3.12: Penetration without PPMD (a), Axial Velocity without PPMD (b), Penetration with PPMD (c), Axial Velocity with PPMD (d) at 60 rpm

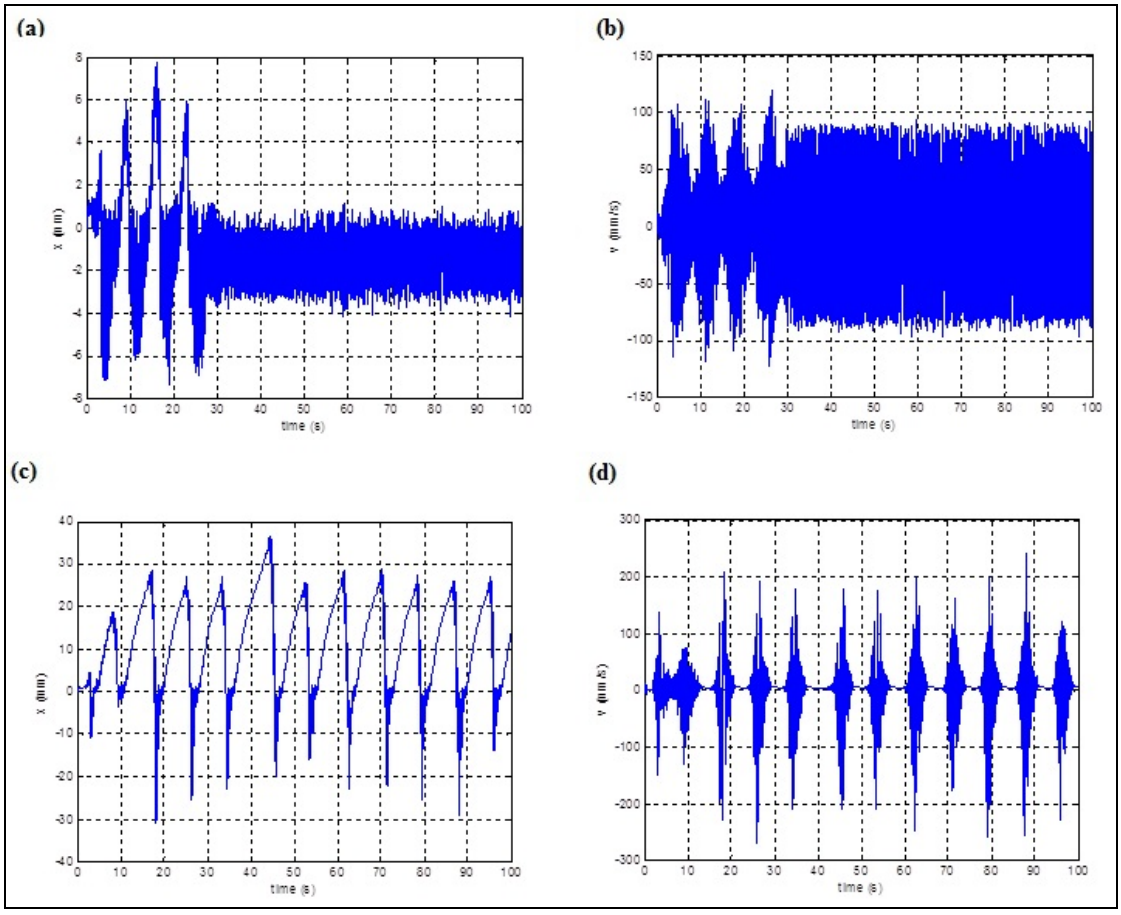

Figure 3.13: Penetration without PPMD (a), Axial Velocity without PPMD (b), Penetration with PPMD (c), Axial Velocity with PPMD (d) at 70 rpm

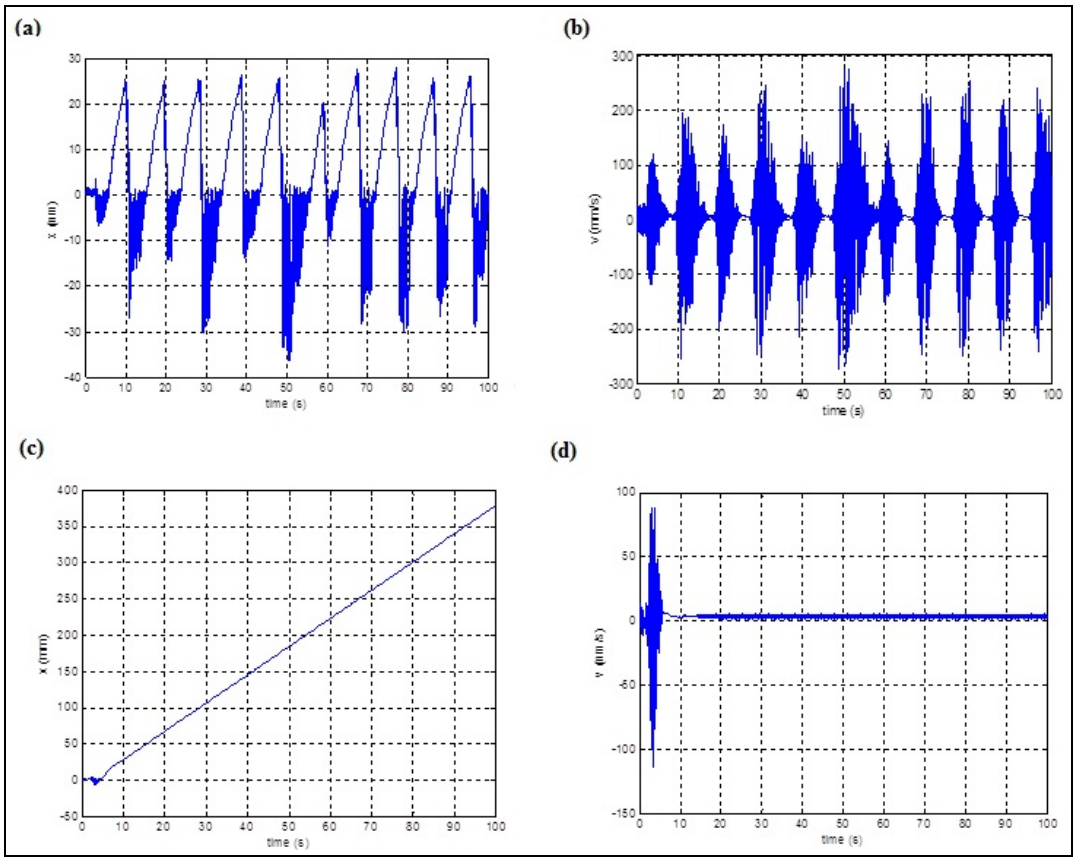

Figure 3.14: Penetration without PPMD (a), Axial Velocity without PPMD (b), Penetration with PPMD (c), Axial Velocity with PPMD (d) at 80 rpm

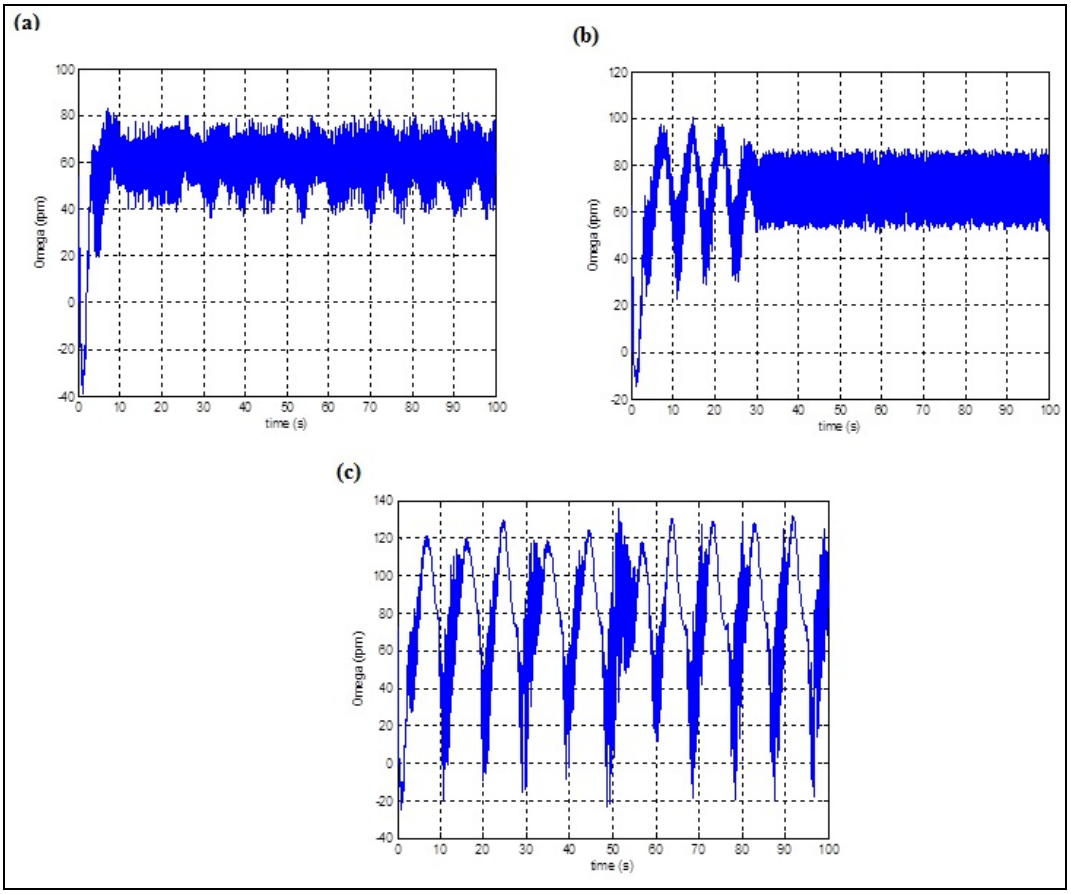

Figure 3.15: Drillbit Spin Velocity without PPMD at Top Drive Spin Speeds of (a) 60 rpm, (b) 70 rpm, and (c) 80 rpm.

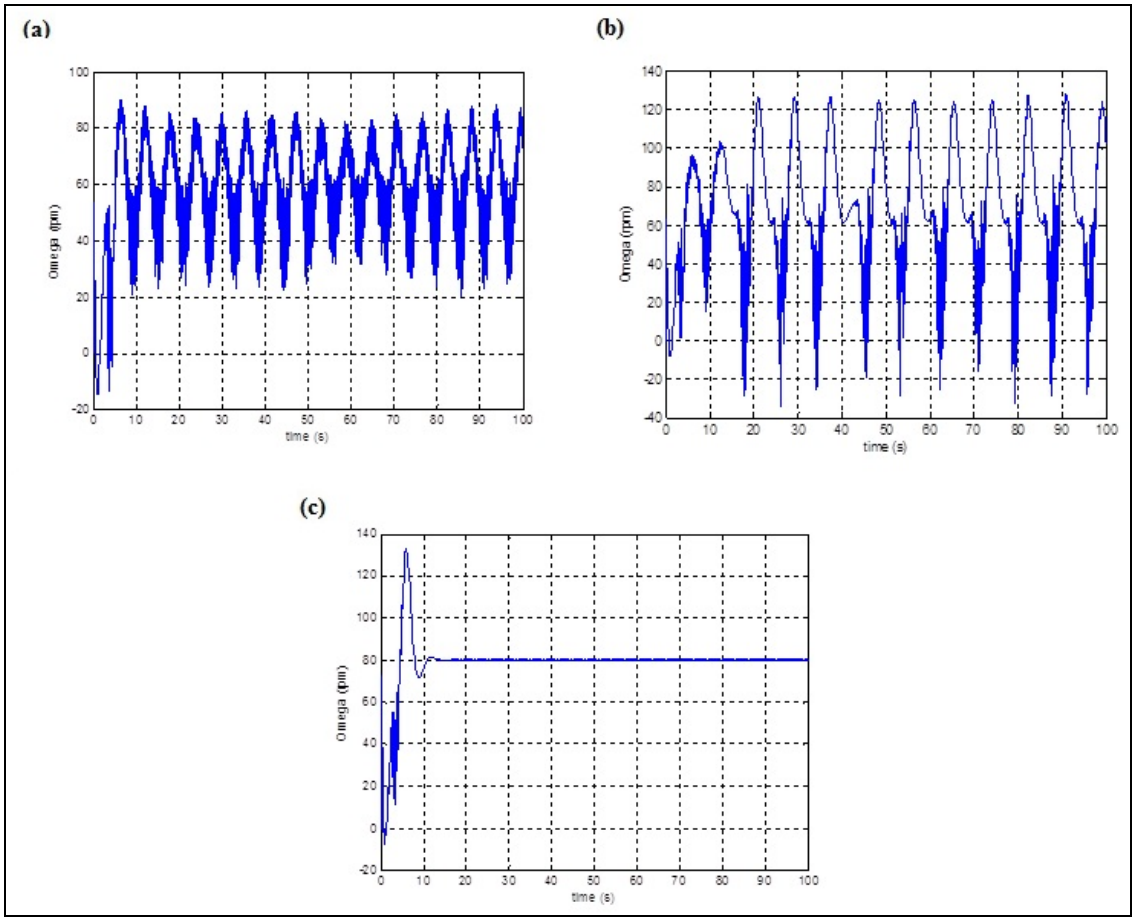

Figure 3.16: Drillbit Spin Velocity with PPMD at Top Drive Spin Speeds of (a) 60 rpm, (b) 70 rpm, and (c) 80 rpm.

3.5 Finite Element Modeling

The modeling of the system can be enhanced by utilizing a finite element model (FEM) for the BHA. Instead of treating the BHA as a single mass and inertia, the BHA is meshed into a number of elements, and the external forces are applied at the appropriate nodes. For each element, a Timoshenko beam element, with added axial and torsional stiffness compliance, is utilized and each node has six degrees of freedom.

Gyroscopic effects are also included in the FEM. Since the drillpipes are generally much lighter than the BHA, the drillpipes can be substituted by a lumped mass, torsional spring and damper attached to the top node of the BHA. Figure 3.17 shows the FEM of the BHA. Detailed description and numerical evaluation of the FEM matrices are listed in [49].

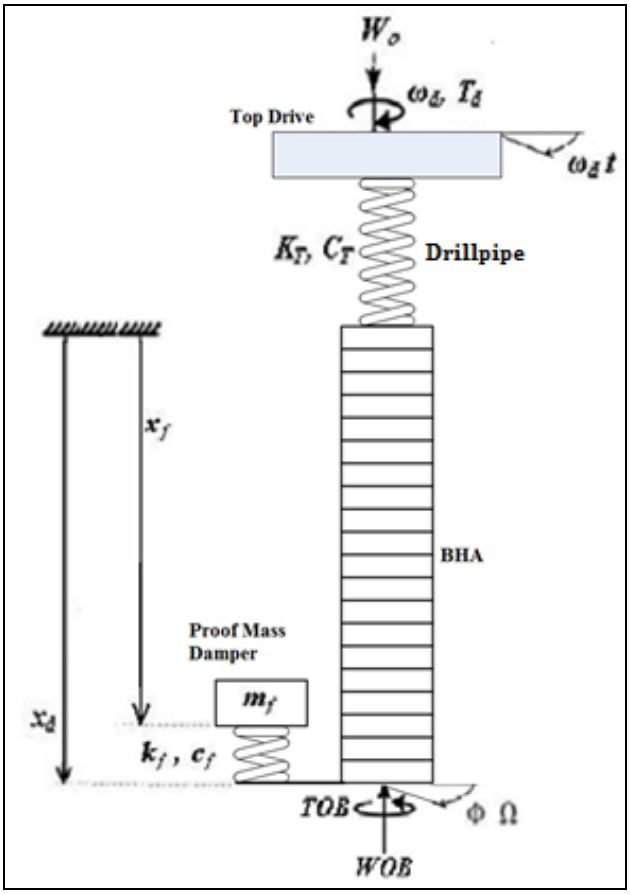

Figure 3.17: FEM of the BHA

4. CHEBYSHEV DISCRETIZATION SPECTRAL METHOD FOR SOLVING THE DELAY DIFFERENTIAL EQUATIONS

In general, the state-space model comprising time-delay is expressed as:

$$\dot{x}(t) = A_0.x(t) + A_1.x(t-\tau) + B.u(t) \tag{4.1}$$

The characteristic equation is a quasi-polynomial in the form of:

$$\left| s.I - A_0 - A_1.e^{-\tau.s} \right| = 0 \tag{4.2}$$

The presence of the term $e^{-\tau.s}$ leads to a theoretical infinite number of complex solutions for a continuous system. A discrete system will have a finite number of roots. In this work, the quasi-polynomial is solved using the approach developed by Breda et al [50] to discretize the solution operator. The solution operator is the operator transforming an initial condition φ onto the solution segment at a later timepoint specified by a parameter *h*, in the following sense:

Definition: The solution operator of the DDE in Equation 4.1 is the operator transforming an initial condition ϕ to the solution segment at timepoint h. This operator is denoted by $T(h) : C([-\tau, 0], \Re^n) \rightarrow C(-\tau, 0], \Re^n)$. The solution operator applied to ϕ, i.e., $(T(h)\ \phi)(\theta) =: \psi(\theta)$, is the solution segment of (4.1) with initial condition $\varphi = \phi$ at time-point h. More precisely,

$\psi(\theta) := (T(h)\ \phi)(\theta) = x(h+\theta)$, $\theta \in [-\tau, 0]$, where $x(t)$ is the solution of Equation 4.1 with initial condition $\varphi = \phi$.

Every DDE can be rewritten as a partial differential equation (PDE) by introducing an additional memory-dimension. If the original DDE is represented as:

$$\begin{cases} \dot{x}(t) = A_0.x(t) + A_1.x(t-\tau) & t \geq 0 \\ x(t) = \varphi(t) & t \in [-\tau, 0] \end{cases} \tag{4.3}$$

Then, the equivalent PDE can be written as a boundary value problem as:

$$\begin{cases} \dfrac{\partial u}{\partial \theta} = \dfrac{\partial u}{\partial t} & t \geq 0,\ \theta \in [-\tau, 0] \\ u'_\theta(t,0) = A_1.u(t,-\tau) + A_0.u(t,0) & t \geq 0 \\ u(0,\theta) = \varphi(\theta) & \theta \in [-\tau, 0] \end{cases} \tag{4.4}$$

for the unknown $u \in C([0,\infty]\times[-\tau,0],\Re^n)$. Let $\varphi \in C([-\tau,0],\Re^n)$ be given. Then if $x(t)$ is the solution to Equation 4.3 and if $u(t,\theta)$ is a solution to Equation 4.4, then:

$$u(t,\theta) = x(t+\theta), \quad \theta \in [-\tau, 0],\ t \geq 0 \tag{4.5}$$

Let A correspond to the differentiation operator in θ-direction with the domain of functions fulfilling the boundary conditions in Equation 4.4, that is:

$$(A\varphi)(\theta) := \frac{d\varphi}{d\theta}(\theta), \qquad \varphi'(0) = A_1\varphi(-\tau) + A_0\varphi(0) \tag{4.6}$$

Hence the problem is reduced to an abstract Cauchy-problem in the form:

$$\frac{d}{dt}x_t = Ax_t \tag{4.7}$$

The differentiation operator, ***A***, of the abstract Cauchy-problem is expressed in terms of the solution operator of the DDE, T, as:

$$A\varphi := \lim_{t\to 0^+} \frac{1}{t}(T(t)\varphi - \varphi) \tag{4.8}$$

The eigenvalues of the operator ***A*** are the eigenvalues of the DDE. It is now required to discretize ***A*** and compute the eigenvalues of the corresponding finite-dimensional linear operator $\mathbf{A_N}$

For a given natural number, *N*, the Chebyshev nodes over the interval [-τ,0] are defined as [51]:

$$x_{N,i} = \frac{\tau}{2}.\left(\cos\left(i.\frac{\pi}{N}\right) - 1\right) \qquad , i = 0,\ 1,\ 2,\ \ldots\ N \tag{4.9}$$

The Chebyshev differentiation matrix, $\mathbf{D_N}$, is obtained utilizing the Chebyshev nodes as [52]:

$$\mathbf{D_N} = \frac{-2}{\tau}\begin{pmatrix} -1 & 1 & & \\ & \ddots & \ddots & \\ & & -1 & 1 \end{pmatrix} \in \Re^{N\times(N+1)} \tag{4.10}$$

Thus $\mathbf{A_N}$ can now be evaluated as [52]:

$$\mathbf{A_N} = \begin{bmatrix} \mathbf{D_N} \otimes \mathbf{I_m} \\ \mathbf{A_1} 0 \cdots 0 \mathbf{A_0} \end{bmatrix} \in \Re^{mN\times mN} \tag{4.11}$$

where ***m*** is the number of degrees of freedom of the original state space of the continuous DDE.

Thus, given a drillstring system that utilizes a PDC drillbit, the Chebyshev Spectral Method can be implemented to determine its stability based on its eigenvalues. It is the purpose of this study to determine a range of stabilizing mass, stiffness and damping values of the PPMD as well as defining operation-stable regions. Stability

implies that there are no axial or torsional vibrations which means that the value of the time delay evaluated in Equation 3.12 is constant and equal to $2\pi/(\omega_d.n)$ since at stable steady state conditions the drillbit spin speed will be equal to that of the top drive. The Chebyshev DDE numerical solver is a linear method, and hence linearity is assumed at steady-state stable conditions meaning that there is always contact between the drillbit and the formation and that the drillbit reactive friction force and torque, W_f and T_f are neglected since they cannot be accounted for in Equation 4.11 as well as the applied axial load, W_o and the top drive applied torque, T. The dynamic cutting components W_c and T_c are accounted for since they are a function of the drillbit's dynamic depth of cut that is the dominating self-exciting source of vibration as stated by Richard et al [10-11]. Richard et al [10-11] also states that the drilling condition is that $W_o > W_f$. In the event a Stribeck friction model is implemented, a linearized damping coefficient can be obtained through a Taylor-Series-Expansion of Equation 3.19. Figure 4.1 shows the linearized damping coefficients over the spin speed rate. It can be observed that the highest negative-damping coefficient is -60 N.m.s/rad, and so as long as the positive torsional damping $\boldsymbol{c_T}$ is high enough, then the Chebyshev method can overcome the Stribeck Friction Effect .

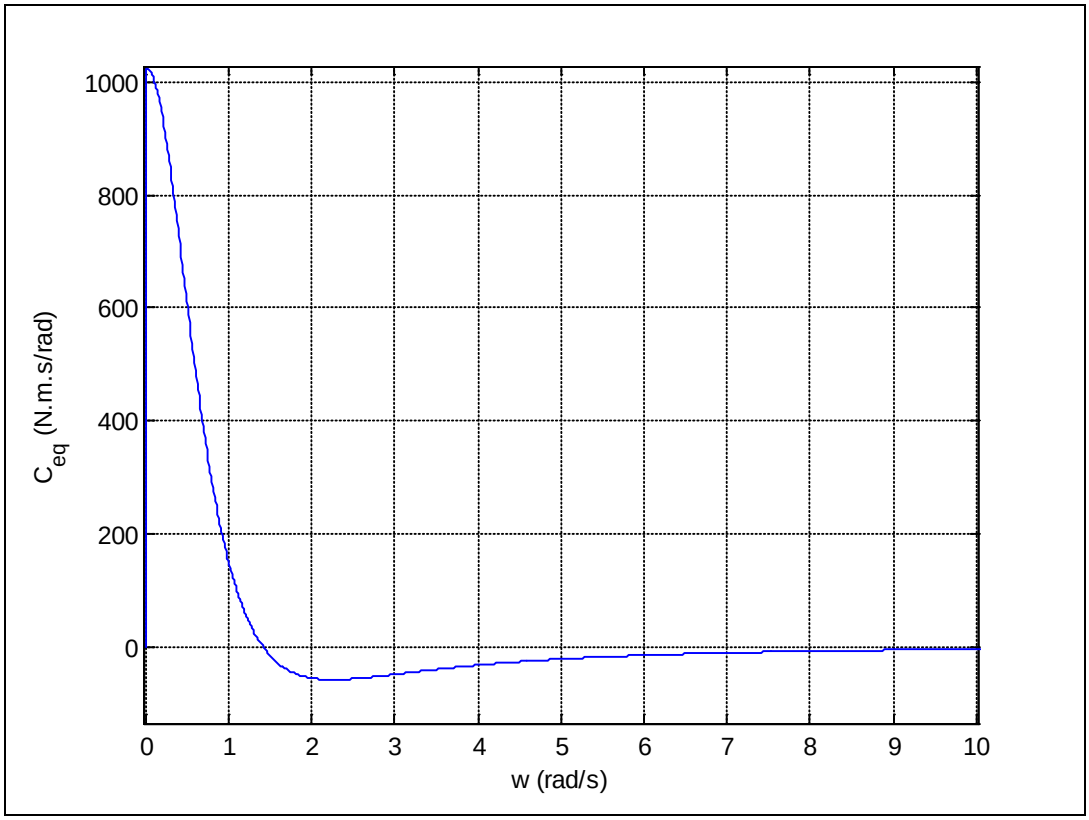

Figure 4.1: Linearized Torsional Damping Coefficients (Stribeck Friction Model)

5. RESULTS

5.1 Overview

The results are presented in four subsections. Subsection 5.2 demonstrates the effectiveness of the proof-mass-damper (PPMD) in suppressing bit-bounce and torsional vibrations using lumped-mass and finite element models of the BHA that only consider the axial and torsional degrees of freedom. Subsection 5.3 extends the degrees of freedom to include the lateral mode and illustrate the coupling between the axial, lateral, and torsional modes of vibration. Subsection 5.4 presents the results of simulating the flywheel performance when embedded in the BHA and subjected to downhole vibrations. Finally, subsection 5.5 extends the function of the flywheel to act as an active proof-mass-damper (APMD) to mitigate and suppress bit-bounce and torsional vibrations of the BHA.

5.2 Effectiveness of PPMD in Bit-Bounce Suppression

At a certain operating point, there exists a minimum stability speed of the top drive of the rotary table, below which the system becomes unstable due to increased time-delay due to the cutting action of the blades of the PDC drillbit. It is well known that time-delay resembles negative damping that destabilizes a system. Hence, the BHA will be more susceptible to bit-bounce when the speed of the top drive is lowered. In drilling operations, there are several reasons as to why the top drive speed is decreased. Logging-while-drilling (LWD) or measurement-while drilling (MWD) operations usually require lower penetration rates in order to obtain accurate data of the well.

Another reason is the power limitation on the motor driving the rotary table, since as the friction at the drillbit increases, the torque load on the driving motor increases and puts a limit on the maximum rotary speed. Even during normal operation, with increasing torque on bit (TOB), the rotary speed of the drillbit would be oscillating around the mean value of the top drive speed, and when its speed falls significantly, the time-delay between the cutting actions of the individual blades will increase. Moreover, the addition of new sections of drill-pipe requires that the drilling action be temporarily paused, bringing the rotary table to a complete stop, and then restarted passing through low rpm ranges which are susceptible to bit bounce.

Table 5.1: Parameter Description & Values (PDC Drillbit)

Parameter	***Description***	***Value***
$\boldsymbol{J}$	Drill-Collar Inertia	415 kg.m^2
$\boldsymbol{m_d}$	Drill-Collar Mass	87000 kg
$\boldsymbol{K_T}$	Equivalent Drill-pipe Torsional Stiffness	600 N.m/rad
$\boldsymbol{C_T}$	Added Drill-Collar Torsional Damping	500 N.s^2/rad
$\boldsymbol{W_o}$	Static Load	100 kN
$\boldsymbol{a}$	Drill-bit Radius	0.15 m
$\boldsymbol{l}$	Wearflat length	5 mm
$\boldsymbol{\sigma}$	Average Normal Stress	112 MPa
$\boldsymbol{\varepsilon}$	Intrinsic Specific Energy	160 MPa

Table 5.1 Continued

ξ	Inclination of Cutting Force on Cutting Face	0.7
γ	Spatial Orientation of wearflats	1.2
μ_0	Coefficient of Friction	0.06
n	Number of Blades	8

Table 5.2: Simulation Parameters (Roller-Cone Drillbit)

Parameter	**Description**	**Value**
k_c	Rock Formation Stiffness	67-134 MN/m
s_0	Formation Elevation Amplitude	1 mm
b	Formation Surface Function Constant	1
c_1	Penetration Constant	1.35e-8
c_2	Penetration Constant	-1.9e-4

One of the methods to stabilize the system is by adding additional mass to the BHA in order to suppress bit-bounce. This can be done by either increasing the BHA length, which is referred to as the "unsprung mass" case, or by attaching attenuator units consisting of a mass sprung on a series of springs and dampers. Figure 5.1 shows the minimum mass ratio needed to suppress bit-bounce over a top drive speed ranging from 65 to 130 rpm. At speeds of 130 rpm or higher, the time-delay is small enough and the

system is stable, and no added mass is needed. It can be clearly seen that the sprung added mass needed is much smaller than its unsprung counterpart.

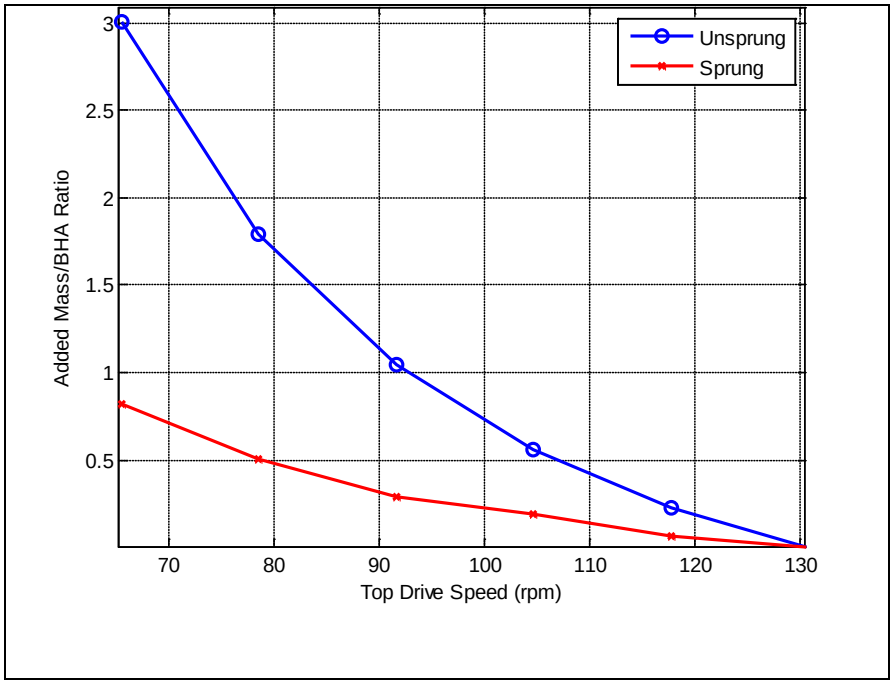

Figure 5.1: Minimum Added Mass Required to Suppress Bit-Bounce at Various Spin Speeds

A rigorous and controlled search, using numerical integration, was carried out to arrive at the stiffness and damping values of the spring, and damper, respectively that yielded the minimum and optimum sprung mass required to suppress bit-bounce. Figure 5.2 shows a 3D plot illustrating the corresponding sprung mass values. The optimum mass was chosen to be the minimum value at each rotational speed. It is to be noted that the entire search elapsed over 20 hours of computational time for a 120,000 possible search points.

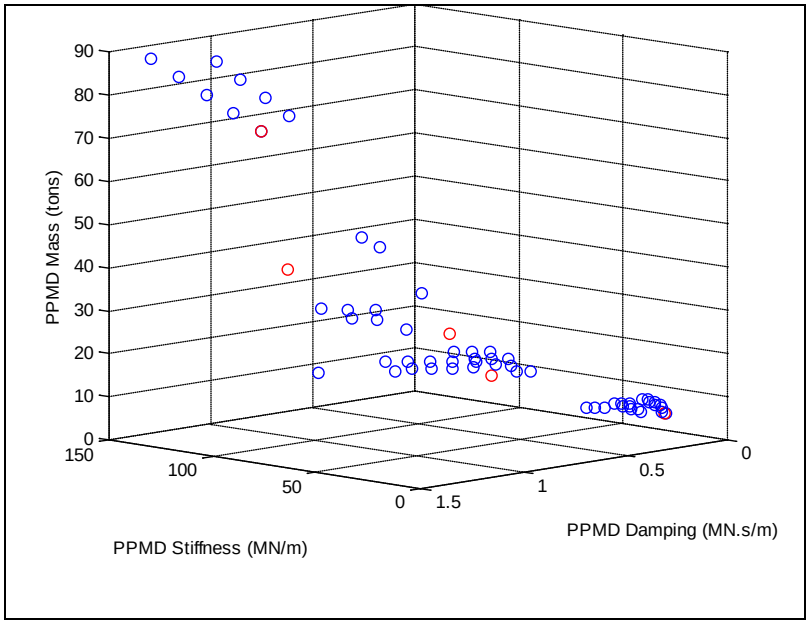

Figure 5.2: PPMD Stable Mass Values (Optimum Values in Red)

Consider a case when the top drive speed drops to 105 rpm, then bit-bounce vibrations will be clearly seen as shown in Figure 5.3 and there will be large fluctuations of the BHA rotary velocity as shown in Figure 5.4. In this case, bit bounce suppression requires that the BHA mass be increased by 49 tons if the mass is fixed to the BHA (unsprung mass), and by only 17 tons if the additional mass is attached to the BHA by appropriately selected stiffness (42.4 MN/m) and damper (0.72 MN.s/m) values (sprung mass). Thus the same result is achieved but the sprung mass is about 3 times less than its unsprung counterpart. Figures 5.5 and 5.6 illustrate the axial and torsional velocities of the BHA, respectively after adding the PPMD.

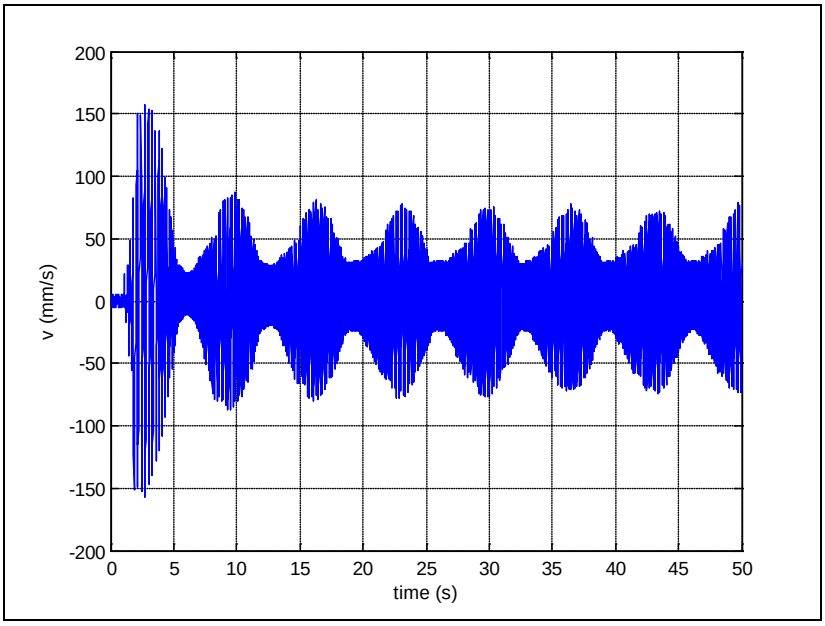

Figure 5.3: Axial BHA Velocity without PPMD (Rock Stress = 160 MPa & Formation Stiffness = 134 MPa)

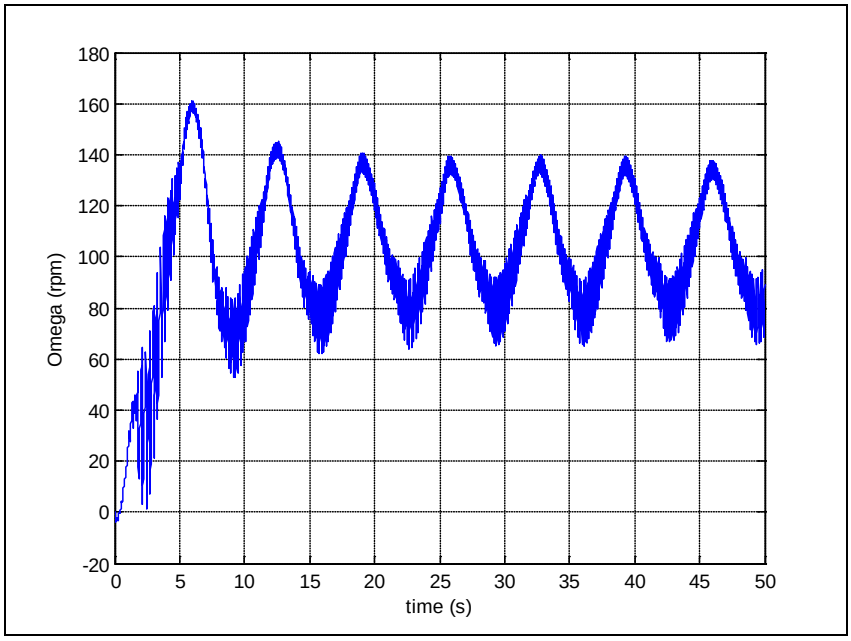

Figure 5.4: BHA Rotational Velocity without PPMD (Rock Stress = 160 MPa & Formation Stiffness = 134 MPa)

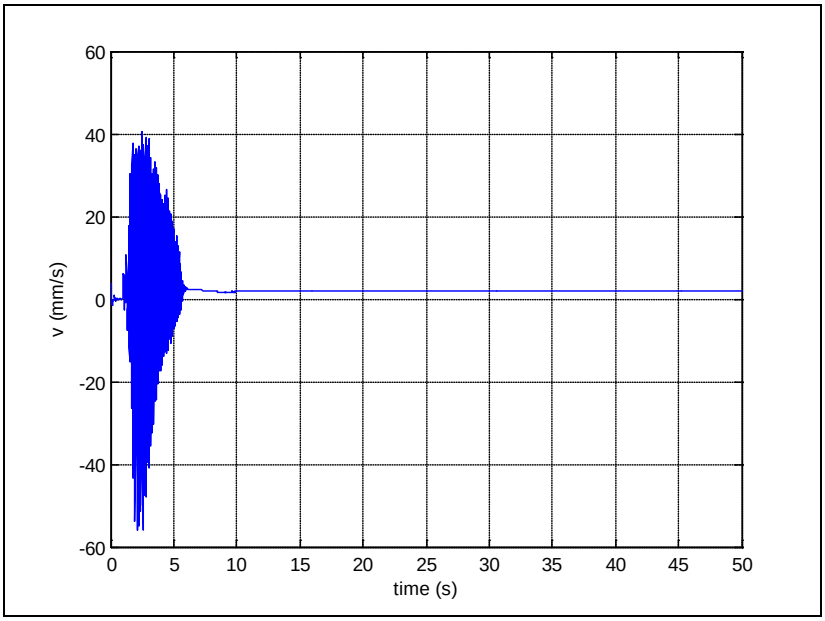

Figure 5.5: BHA Axial Velocity with PPMD (Rock Stress = 160 MPa & Formation Stiffness = 134 MPa)

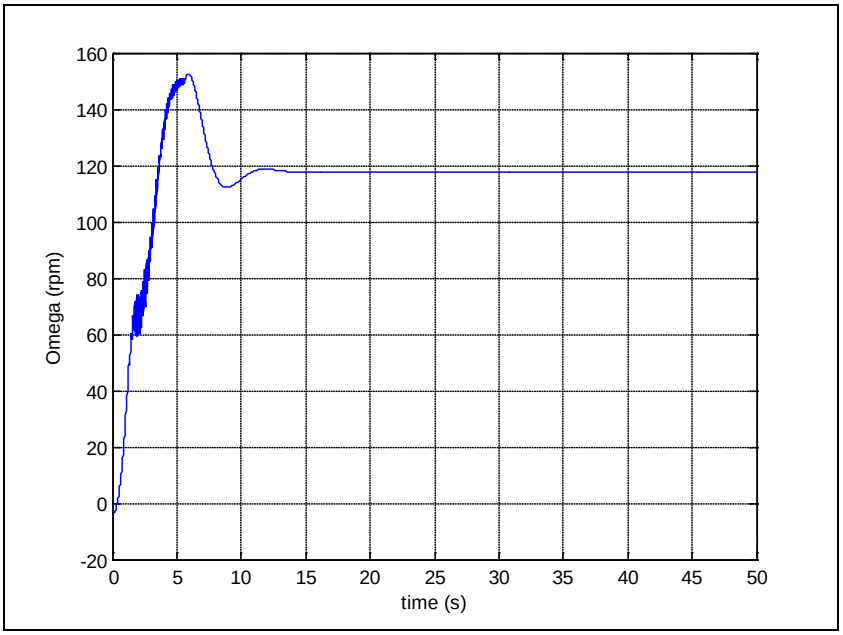

Figure 5.6: BHA Rotational Velocity with PPMD (Rock Stress = 160 MPa & Formation Stiffness = 134 MPa)

Since, numerical integration of the dynamic equations of motion is very time consuming, and thus a relatively few number of possible solutions can be scanned through trial-and-error, the Chebyshev-Based discretization spectral method was implemented in order to find values of the absorber mass, spring stiffness and damping that achieve overall system stability. By applying Equation 4.11, one can now obtain a characteristic matrix, $\mathbf{A_N}$, whose eigenvalues determine the stability. The system is stable if and only if all eigenvalues have negative real values. Hence, the computational time is greatly reduced thousands of possible solutions can be scanned in just a matter of minutes.

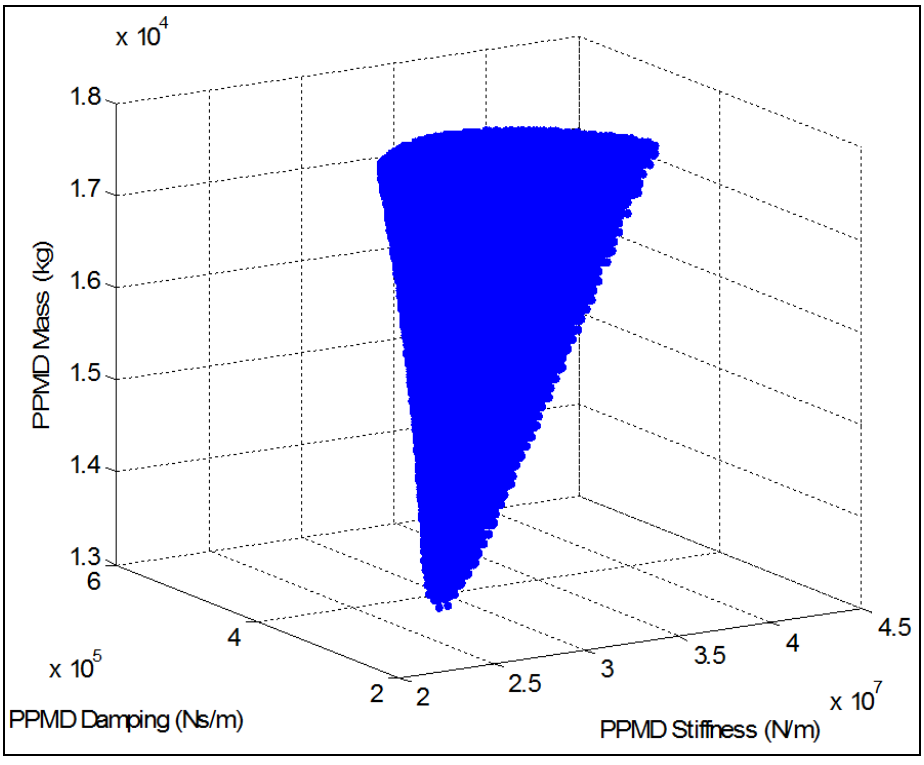

Figure 5.7: 3D Plot of Stable PPMD Values Using the Chebyshev Method

Figure 5.7 shows a 3-dimensional plot of solutions obtained using the Chebyshev-Based discretization spectral method. The number of search points was approximately 10 million points yet the search time elapsed less than 4 hours. If this search was conducted using numerical integration, the search time would be 58 days! If the drillstring model was finite-element based, then at least 1000 days would be needed to conduct this search! The validity of the Chebyshev method is verified by numerical integration at the same condition. Consider a case when the equivalent soil stiffness is 67 MPa and the top drive speed is 80 rpm. Without the PPMD, the system is unstable as can be seen in Figure 5.8 where there exist oscillations of axial velocity. The Chebyshev method predicts this instability through the evaluation of eigenvalues and it can be seen in Figure 5.9 that there are two conjugate and complex poles on the imaginary axis. Note that from Figure 5.9, the right-most conjugate poles have a frequency of 31 rad/s. The periodic time form Figure 5.8 is approximately 0.2 seconds which corresponds to an oscillation frequency of 31 rad/s, which is consistent with the frequency directly evaluated from the eigenvalue plot. Upon installing a PPMD that is 15% in mass of the original BHA whose natural frequency and damping ratio are 30 rad/s and 0.3, respectively, the system becomes stable and Figure 5.10 shows the eigenvalue plot obtained by the Chebyshev method indicating that the previously unstable poles have migrated into the left-hand-plane, further validating the spectral method implemented.

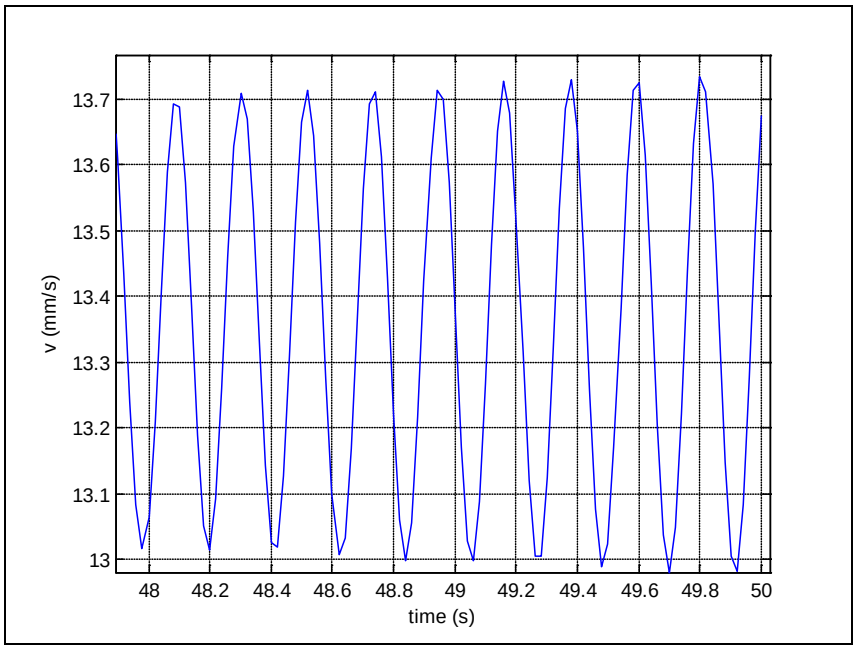

Figure 5.8: BHA Axial Velocity Oscillations Before Adding PPMD

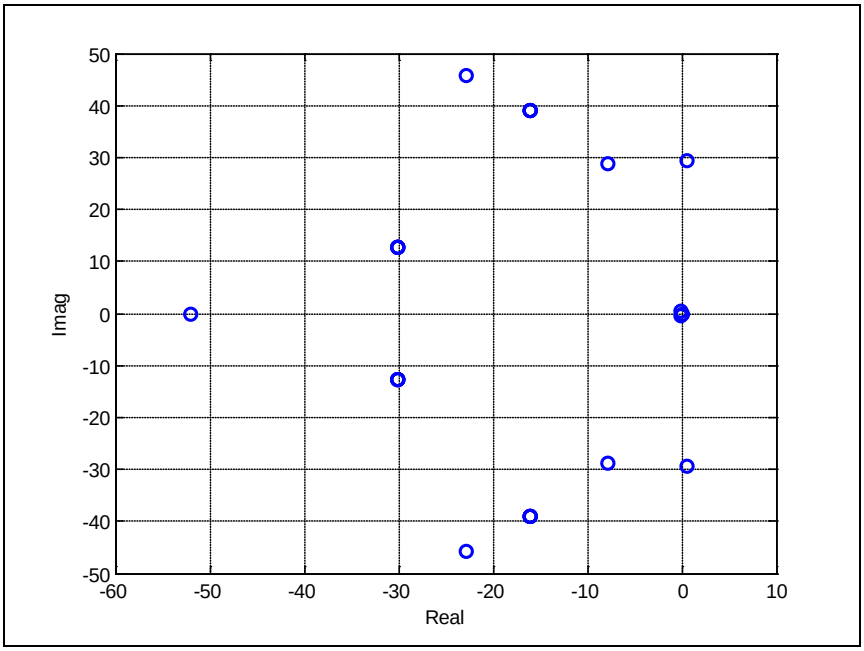

Figure 5.9: Eigenvalue Plot before Adding PPMD

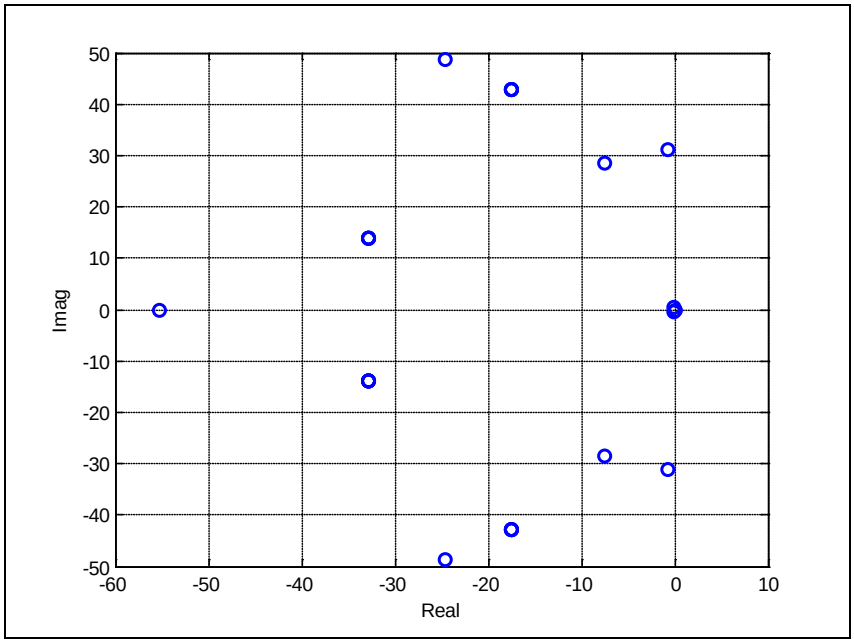

Figure 5.10: Eigenvalue Plot after Adding PPMD

Another advantage of Chebyshev method is that it can be implemented to obtain/predict operating-point stability chart. The term stability implies that there are neither axial nor torsional oscillations, i.e. the drillbit's axial and spin velocities are both constant, meaning that the time delay has a constant value at steady state. Figure 5.11 shows the stability boundary obtained utilizing the Chebyshev numerical DDE solver and rigorous numerical integration of the equations of motion utilizing a lumped model, FEM of the BHA, and FEM of the drillstring (BHA + drillpipe). As can be observed, there are minor differences in the onset stability spin speed in the 4 cases and the percentage deviation from the FEM-Drillstring model is under 9% as can be observed in Figure 5.12. It can also be observed from Figures 5.11 and 5.12 that the Chebyshev-Boundary-Line deviation slightly increases especially in the range of 120 – 160 MN/m

because the stability boundary lines where evaluated at W_o = 100 kN and by observing Figure 5.13, the friction component of the WOB, W_f becomes equal to 100 kN at a formation stiffness value of 160 MN/m. The terms, W_o and W_f are not accounted for in the eigenvalue characteristic equation described by Equations 3.12 and 4.11 since they are external forces. In order for drilling to take place $W_o > W_f$. Thus, by increasing the value of the applied axial load, W_o, the Chebyshev-Boundary-Line starts to deviate less from the FEM. Figure 5.14 shows the stability-boundary-line plot using W_o = 120 kN and Figure 5.15 quantifies the percentage deviation from the FEM-Drillstring. It can now be clearly observed that there is less deviation of the Chebyshev-Boundary-Line when W_o was increased over W_f. A remarkable observation is that there is a minor difference between both FEM-BHA and FEM-Drillstring in predicting the onset stability spin speed, the lumped model under-predicts this onset spin speed and the Chebyshev DDE solver predicts it in-between.

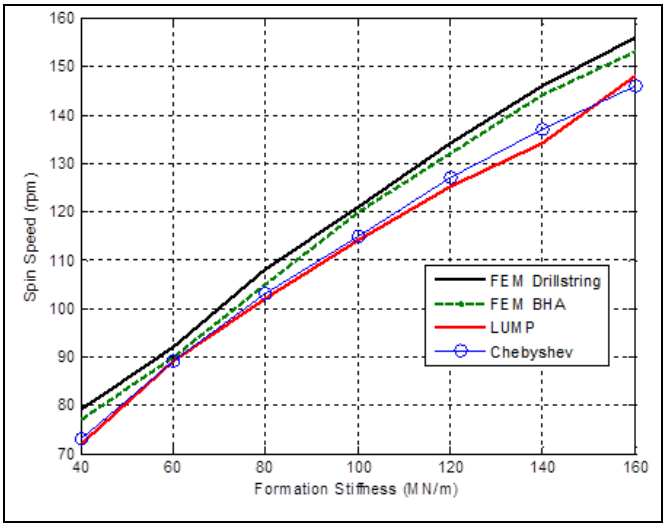

Figure 5.11: Operating Stability Boundary Curves (W_o = 100 kN)

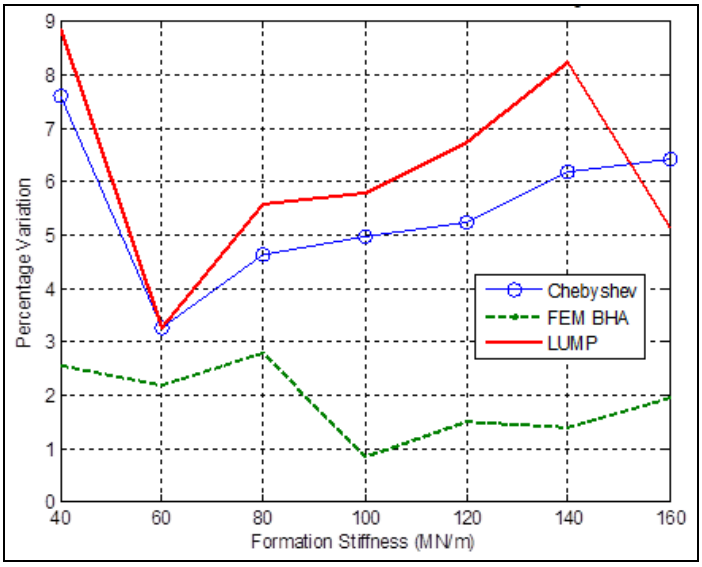

Figure 5.12: Percentage Deviation of Onset Stability Spin Speed from FEM-Drillstring (W_o = 100 kN)

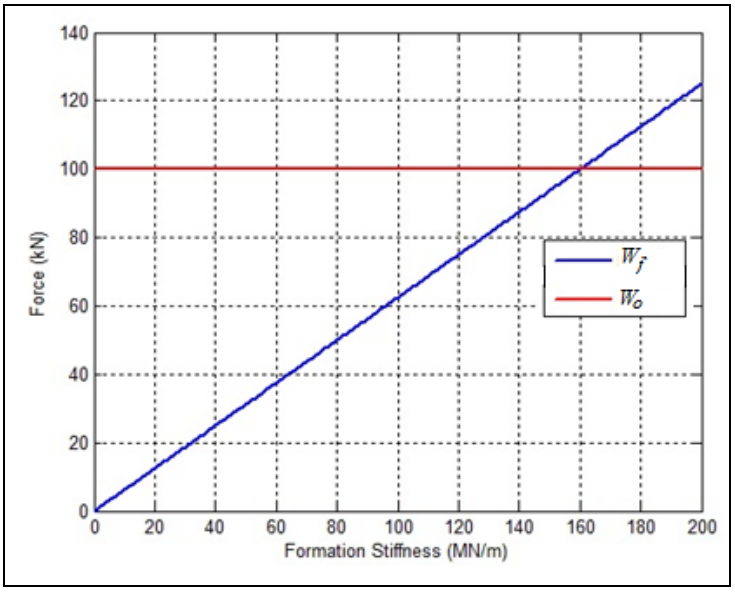

Figure 5.13: Applied Axial Load (W_o) vs. Friction Component of WOB (W_f)

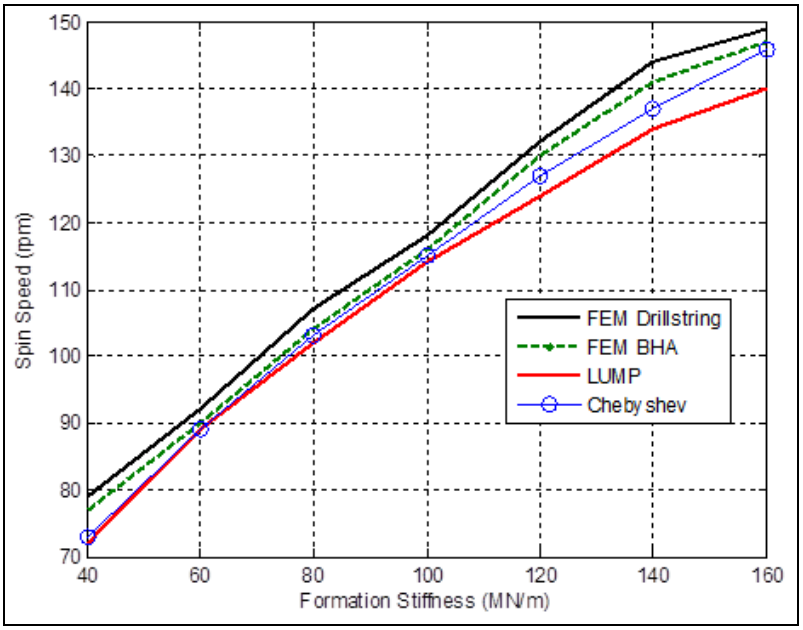

Figure 5.14: Operating Stability Boundary Curves (W_o = 120 kN)

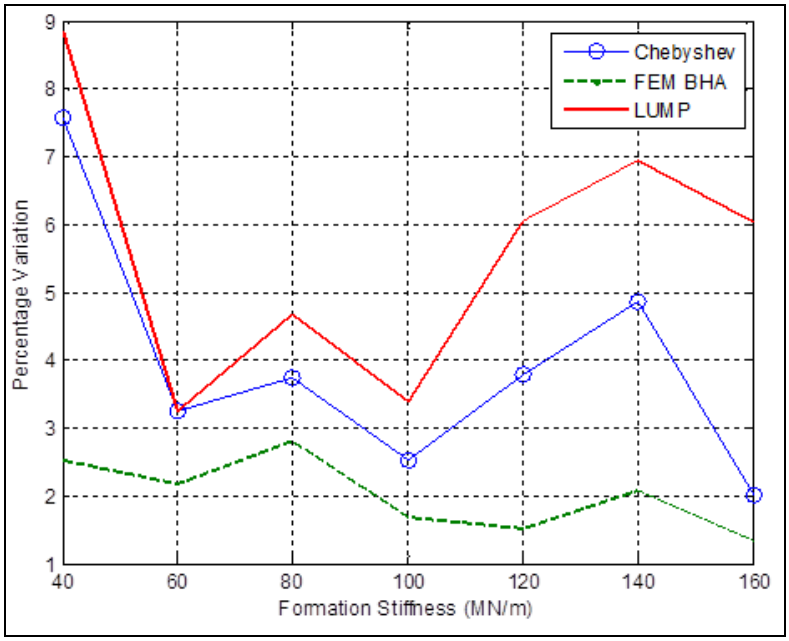

Figure 5.15: Percentage Deviation of Onset Stability Spin Speed from FEM-Drillstring (W_o = 120 kN)

Figure 5.16 shows a stability chart (very fine mesh) of top drive speed versus rock formation stiffness for different values of PPMD mass. The grid was divided into 1.2 million search points and the elapsed time to evaluate this chart was only 45 minutes.

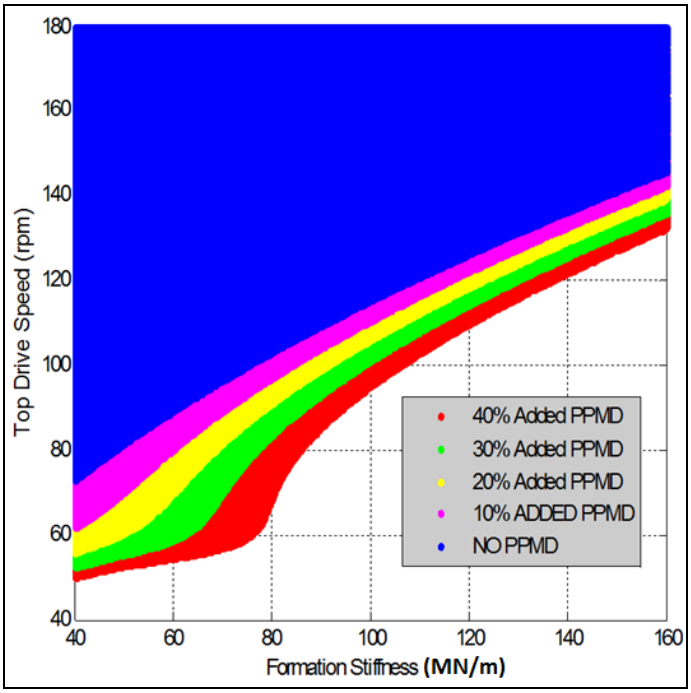

Figure 5.16: Operating-Point Stability Chart

Figures 5.17 – 5.20 show the system performance when drilling a formation stiffness of 100 MN/m with a PDC drillbit at 105 rpm before adding the PPMD by utilizing the lumped model and FEM. Figures 5.21 – 5.24 show suppression of bit-bounce and torsional vibrations after adding a PPMD that is 15% the original mass of the BHA and has a natural frequency and a damping ratio of 30 rad/s and 0.3, respectively. In Figures 5.17 – 5.24 the response is obtained using the lumped model, the FEM of the

BHA only, and the FEM of the entire drillstring (BHA + drillpipe). In all modeling cases, adding the PPMD completely suppresses the vibrations all 3 cases (both FEM and lumped system) which indicates that the lowest frequencies of vibration are dominant which is consistent with the literature and field observations. A field observation ocean-drilling case-study by Mayers et al. [53] reports that vibration frequencies due to the drillbit excitation lies in the range 0 – 5 Hz and that the higher frequencies in the range of 25 – 50 Hz are due to noise associated with the rig's operations and ship's motors. Richard et al [10] list this range within 0 – 3 Hz.

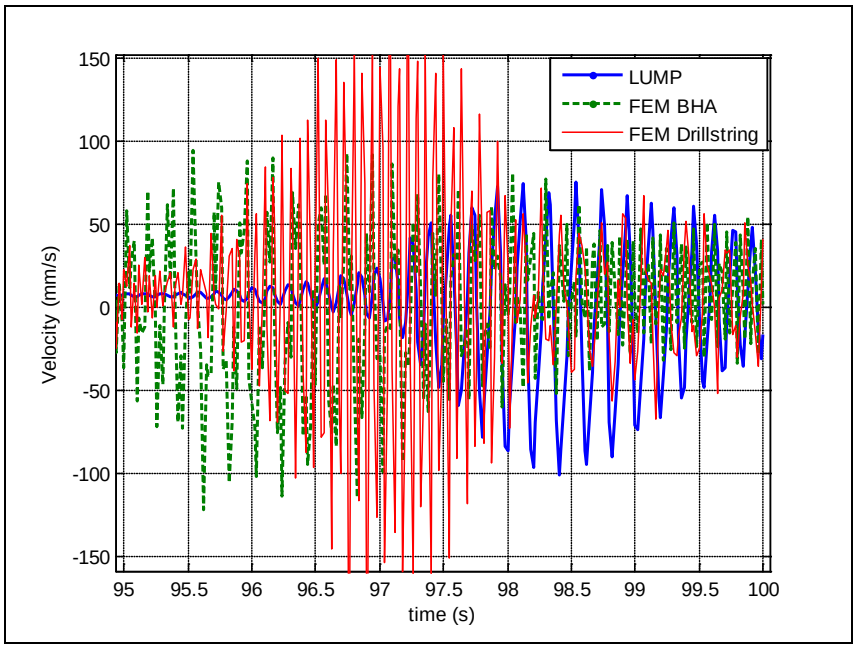

Figure 5.17: Axial Velocity near Drillbit before Adding PPMD (PDC)

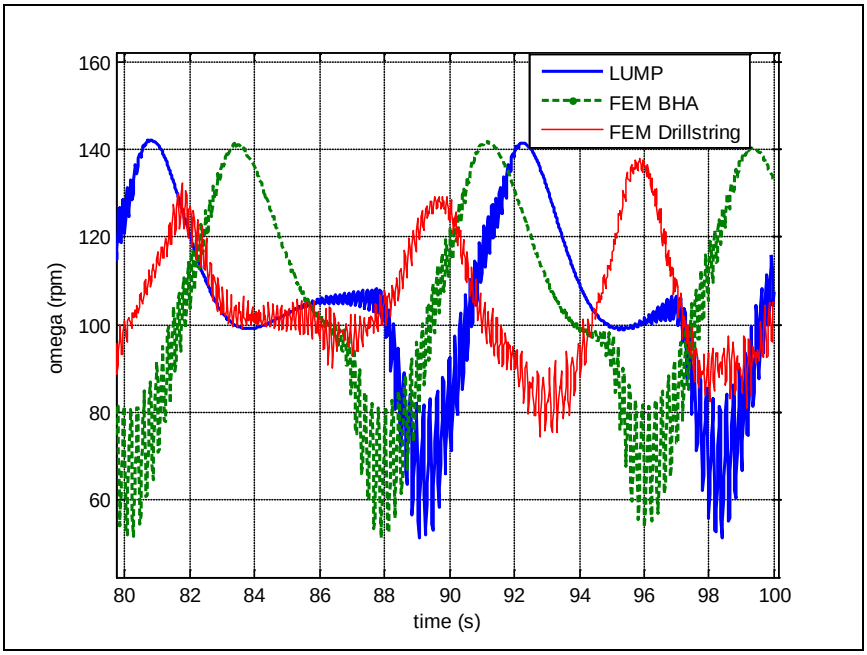

Figure 5.18: Torsional Velocity near Drillbit before Adding PPMD (PDC)

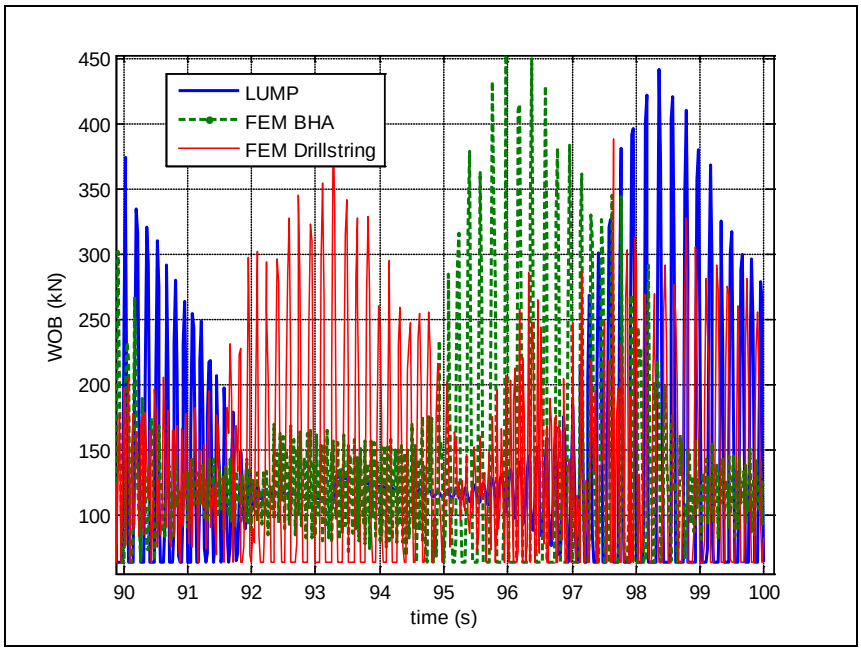

Figure 5.19: Drillbit Reaction Force – WOB before Adding PPMD (PDC)

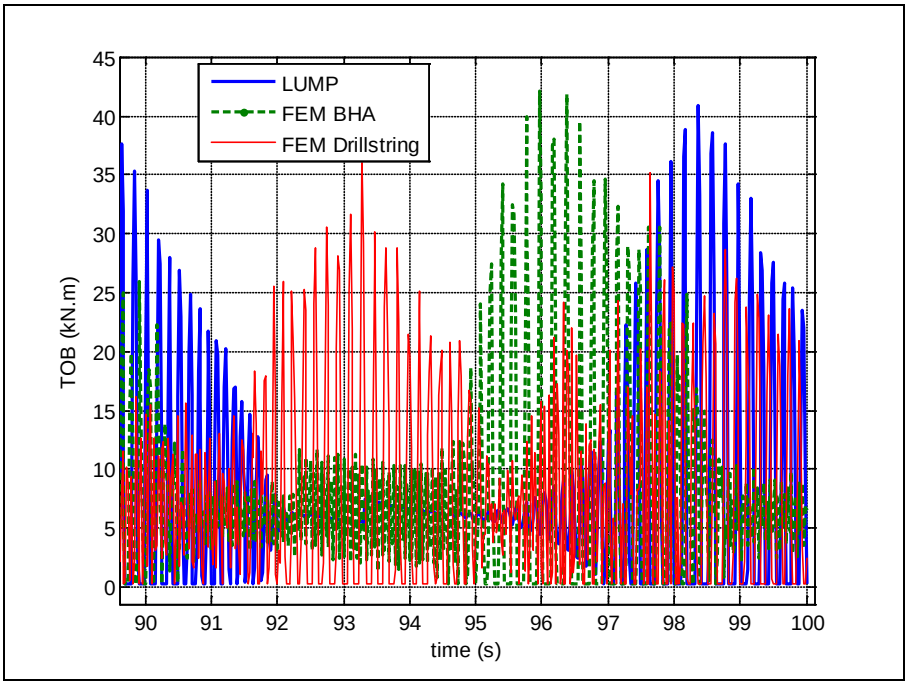

Figure 5.20: Drillbit Reaction Torque – TOB before Adding PPMD (PDC)

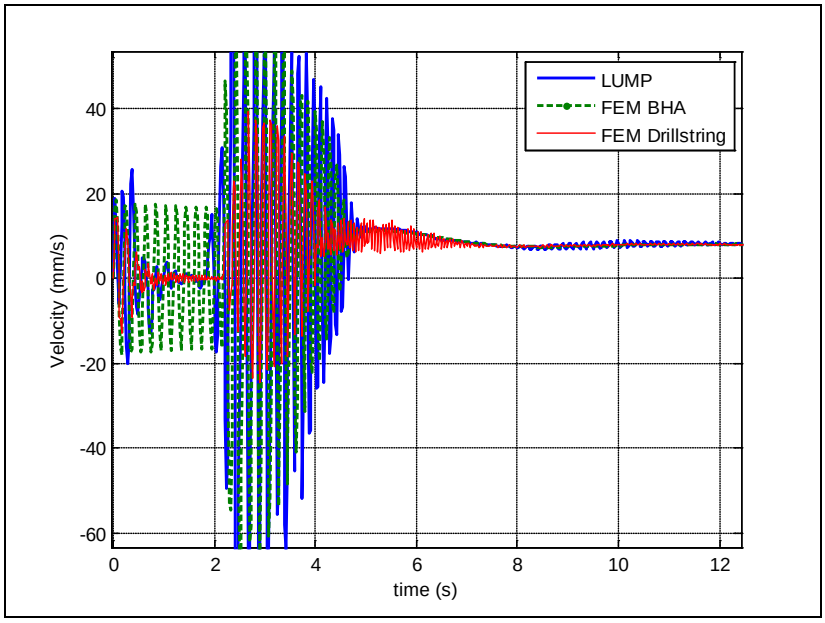

Figure 5.21: Axial Drillbit Velocity near Drillbit after Adding PPMD (PDC)

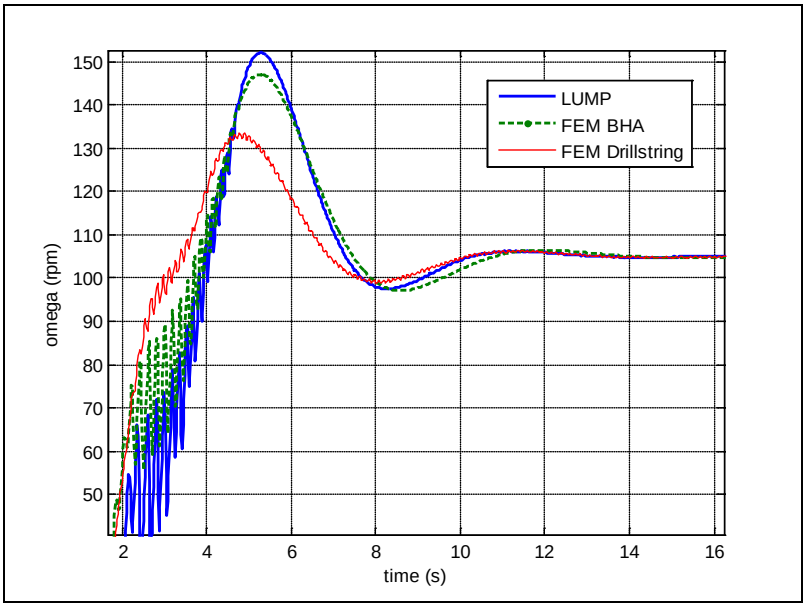

Figure 5.22: Torsional Drillbit Velocity near Drillbit after Adding PPMD (PDC)

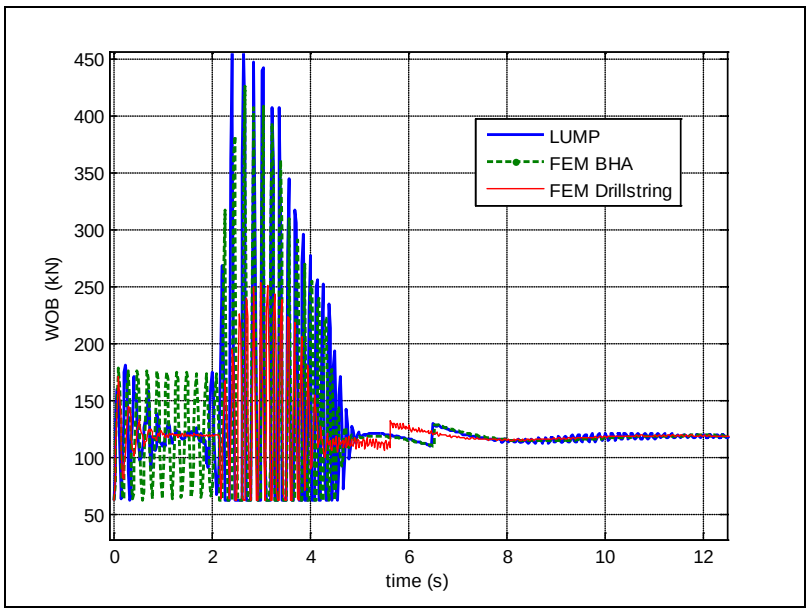

Figure 5.23: Drillbit Reaction Force – WOB after Adding PPMD (PDC)

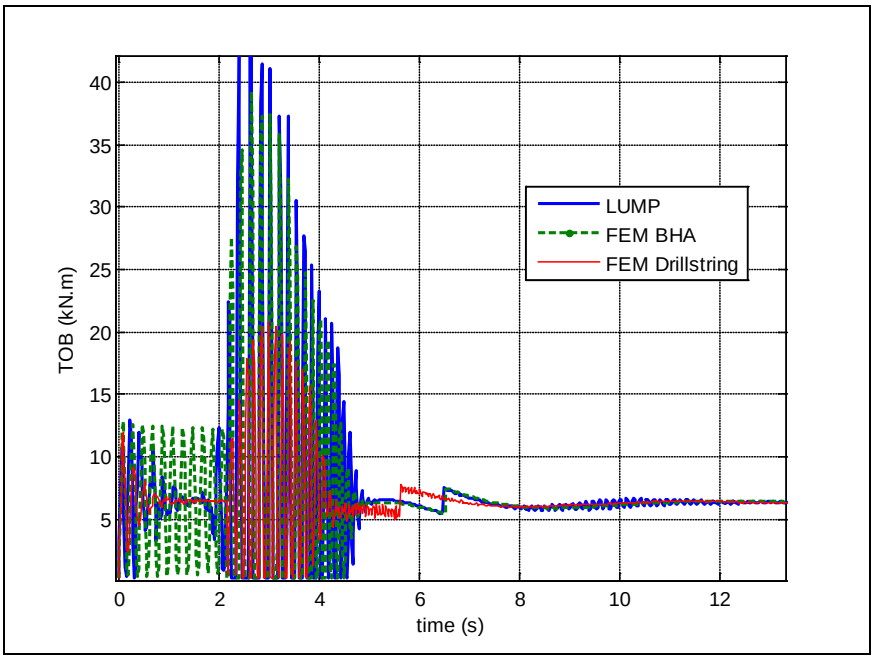

Figure 5.24: Drillbit Reaction Torque – TOB after Adding PPMD (PDC)

Similarly, the comparison simulation was redone but using a roller-cone drillbit instead of a PDC. Figures 5.25 – 5.28 show the drillstring's response before adding the PPMD. After the PPMD is added, the all three models indicate a significant reduction in axial and drillbit spin velocities, as well as WOB and TOB, as shown in Figures 5.29 – 5.32.

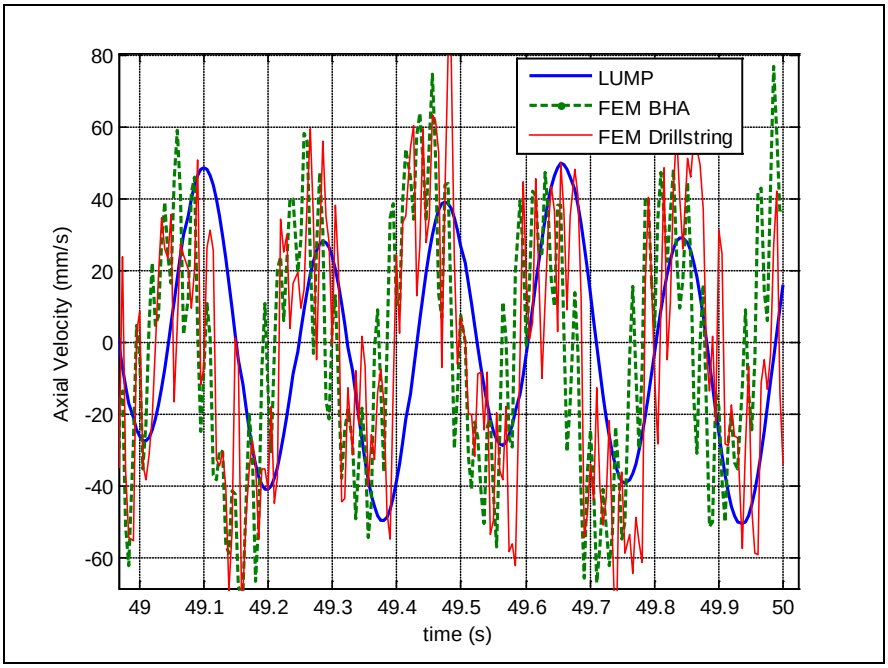

Figure 5.25: Axial Velocity near Drillbit before Adding PPMD (Roller-Cone)

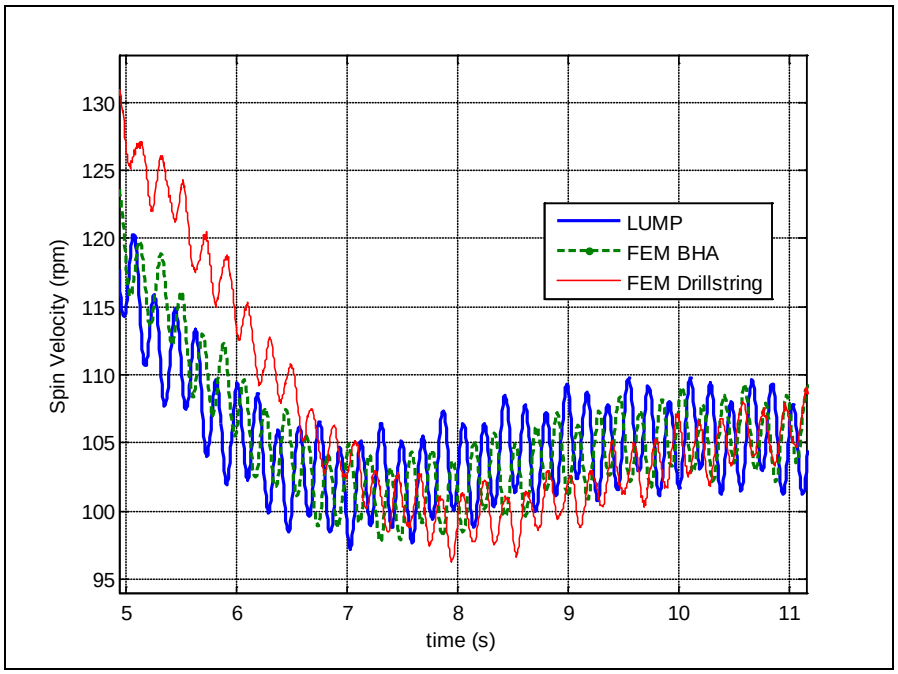

Figure 5.26: Torsional Velocity near Drillbit before Adding PPMD (Roller-Cone)

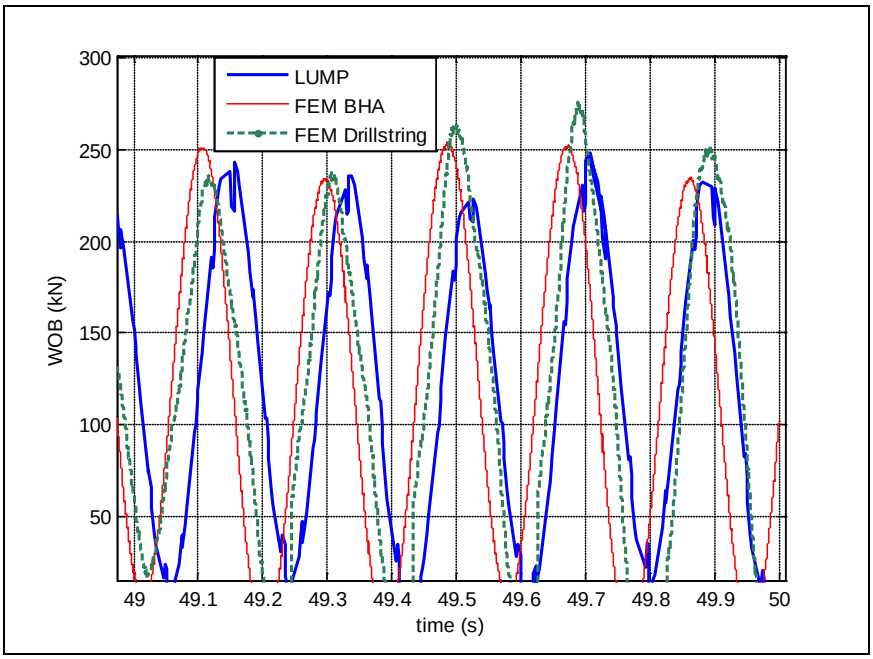

Figure 5.27: Drillbit Reaction Force – WOB before Adding PPMD (Roller-Cone)

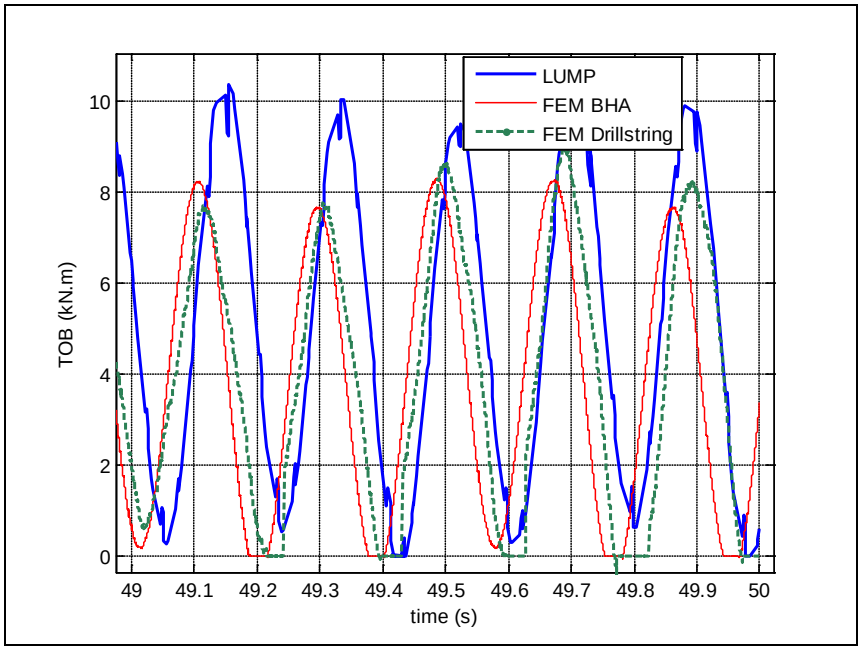

Figure 5.28: Drillbit Reaction Torque – TOB before Adding PPMD (Roller-Cone)

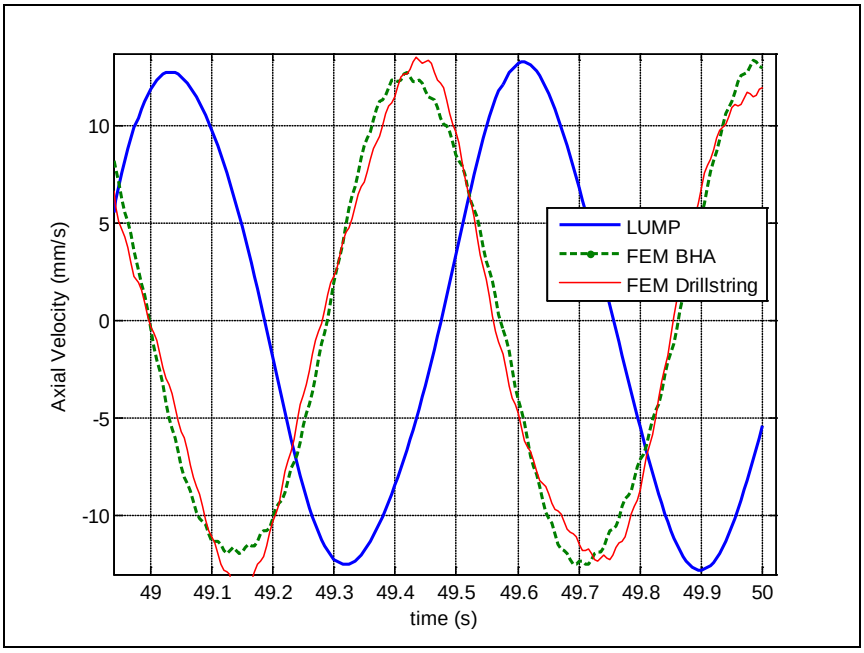

Figure 5.29: Axial Velocity near Drillbit after Adding PPMD (Roller-Cone)

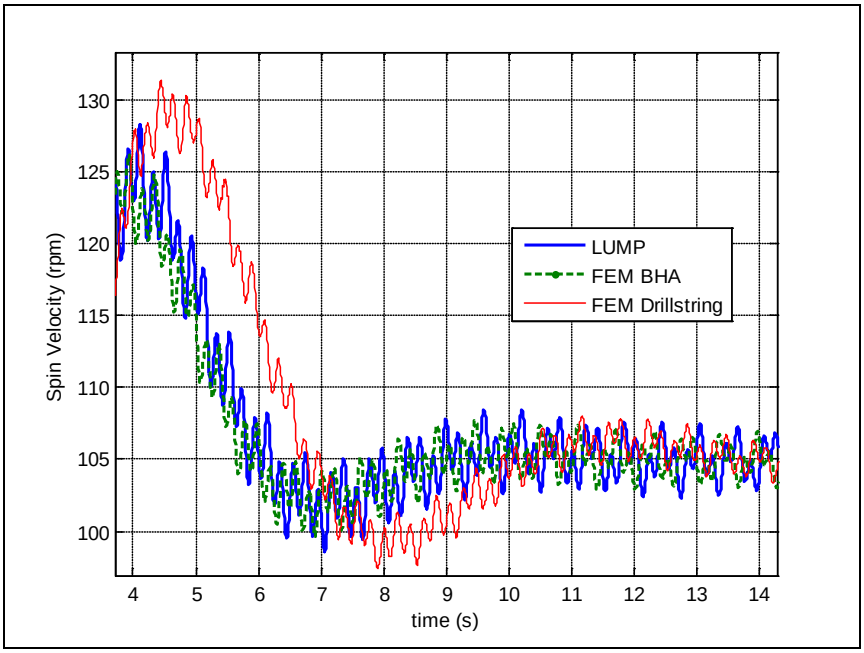

Figure 5.30: Torsional Velocity near Drillbit after Adding PPMD (Roller-Cone)

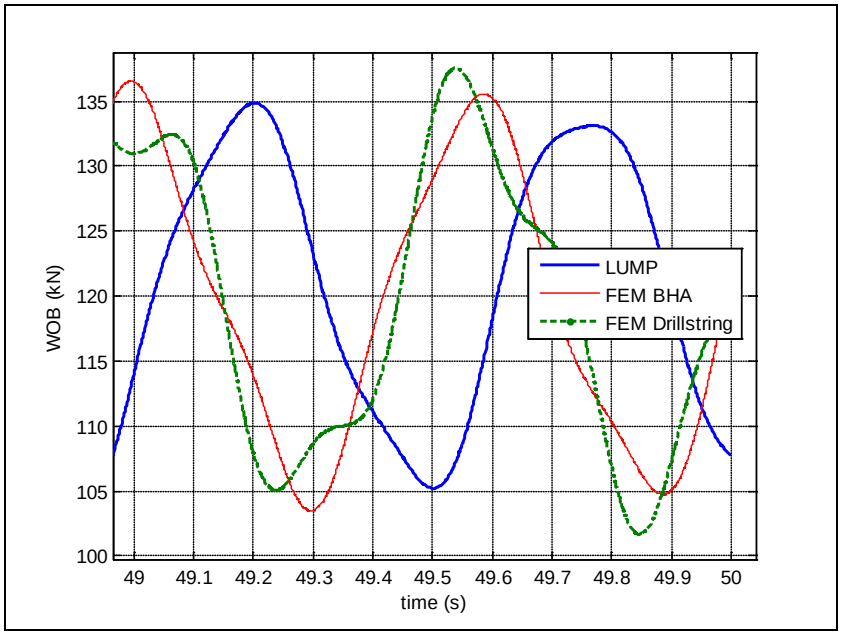

Figure 5.31: Drillbit Reaction Force – WOB after Adding PPMD (Roller-Cone)

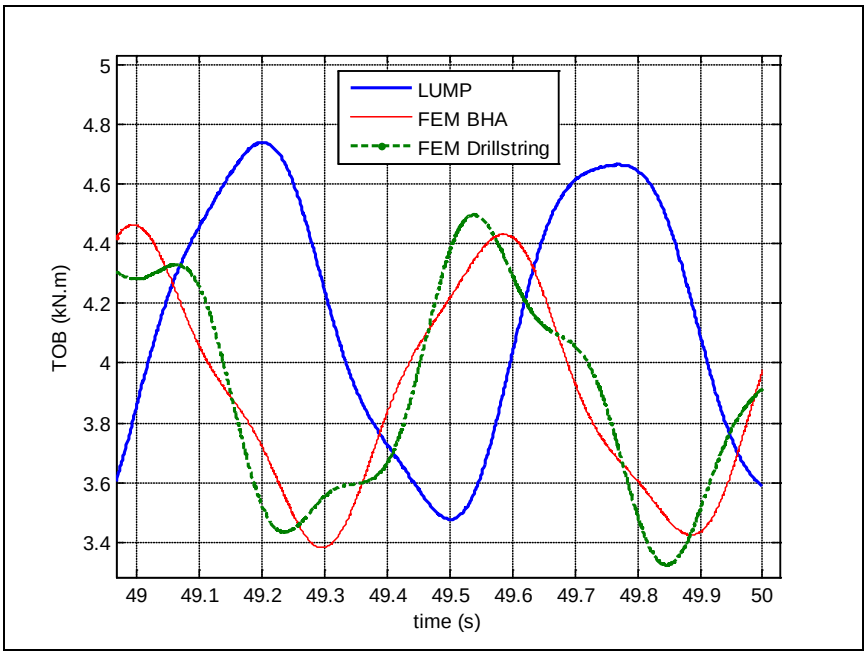

Figure 5.32: Drillbit Reaction Torque – TOB before Adding PPMD (Roller-Cone)

In order to demonstrate robustness, consider a universal PPMD with a natural frequency of 30 rad/s and a damping ratio of 0.3 to be fitted on any BHA that utilizes either a PDC or a roller-cone drillbit. Figure 5.33 shows the decrease of axial vibration amplitudes with increasing absorber mass for different operating top drive spin velocities when a PDC drillbit is used. This is similarly shown when utilizing a roller-cone drillbit in Figure 5.34.

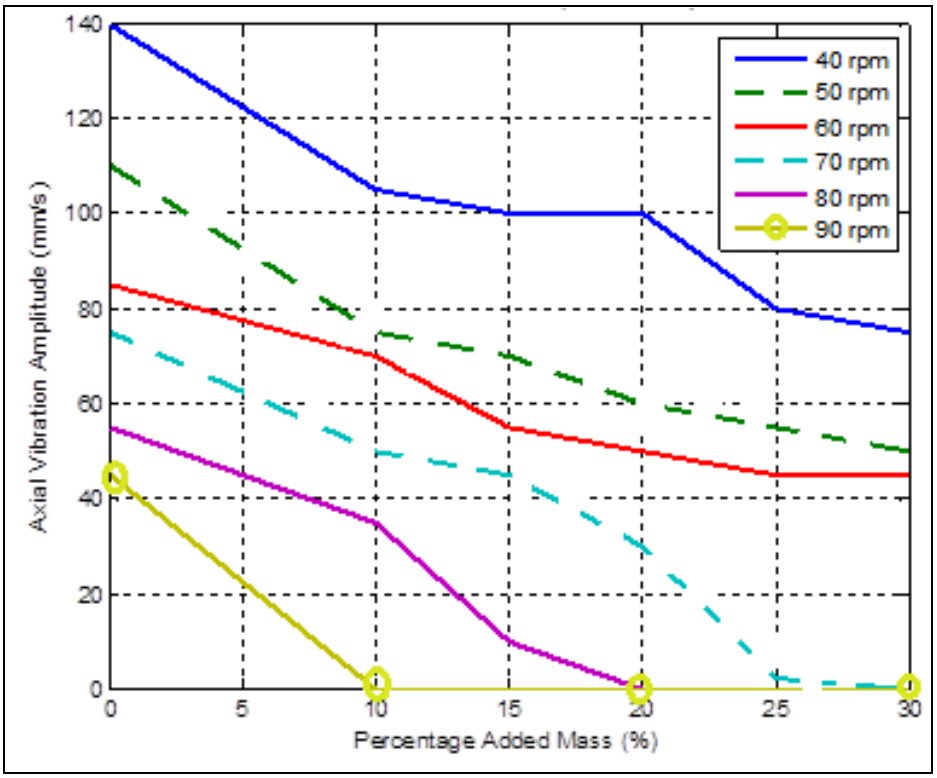

Figure 5.33: Universal PPMD Performance Over Top Drive Spin Speed Range (PDC Drillbit & Rock Stress = 80 MPa)

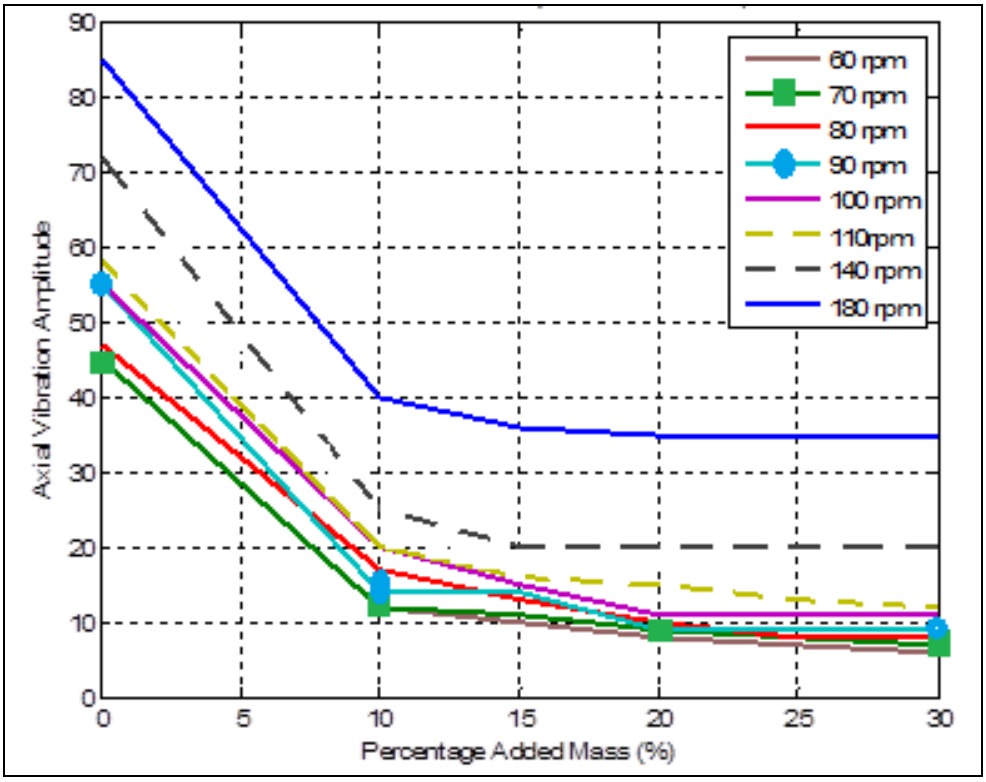

Figure 5.34: Universal PPMD Performance Over Top Drive Spin Speed Range (Roller-Cone Drillbit & Rock Stress = 80 MPa)

Figures 5.35 and 5.36 show a comparison between vibration amplitude values for added sprung and unsprung mass values at a top drive spin speed of 80 rpm for a PDC and roller-cone drillbit, respectively. Figures 5.37 and 5.38 illustrate vibration amplitude values versus rock formation stiffness when adding 15% sprung and unsprung mass to the original 87 tons BHA when the top drive is spinning at 80 rpm for a PDC and roller-cone drillbit, respectively.

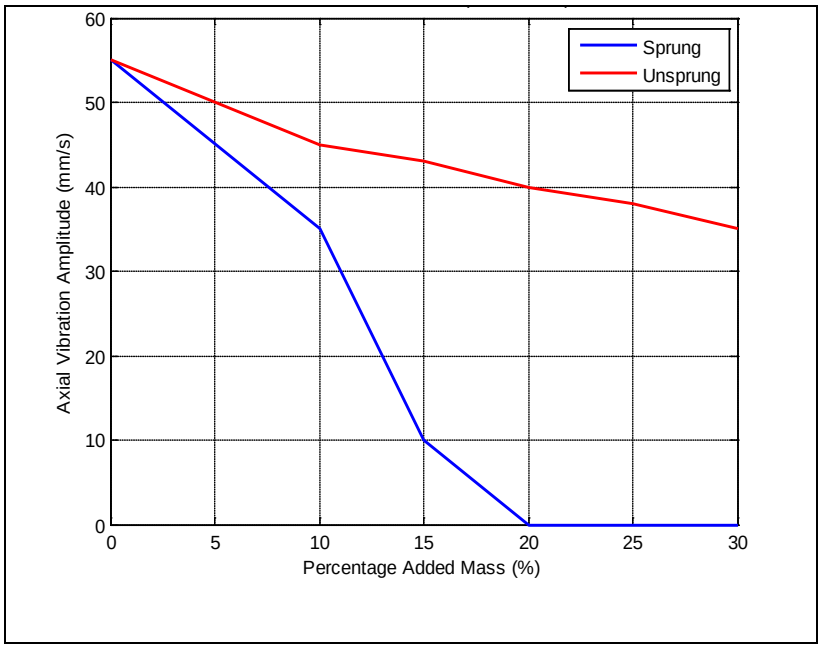

Figure 5.35: Effect of Added Sprung & Unsprung Mass on BHA Vibration (PDC Drillbit & Rock Stress = 80 MPa)

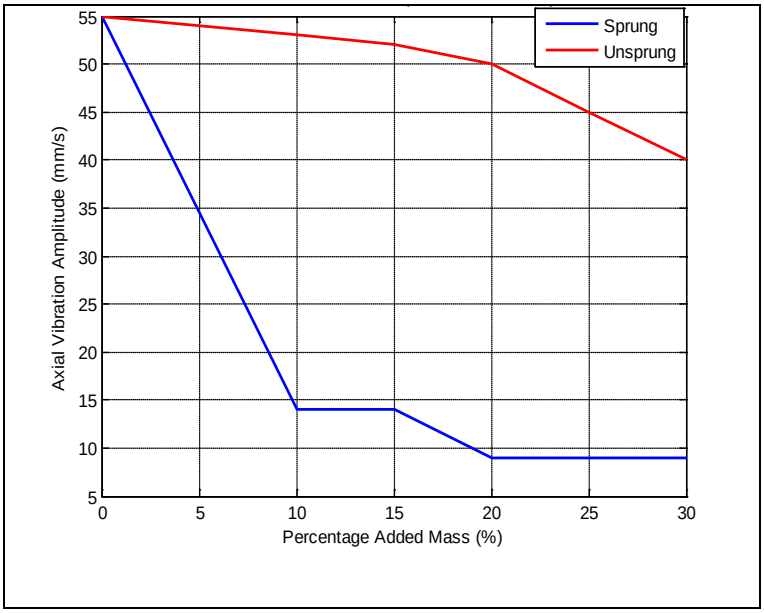

Figure 5.36: Effect of Added Sprung & Unsprung Mass on BHA Vibration (Roller-Cone Drillbit & Rock Stress = 80 MPa)

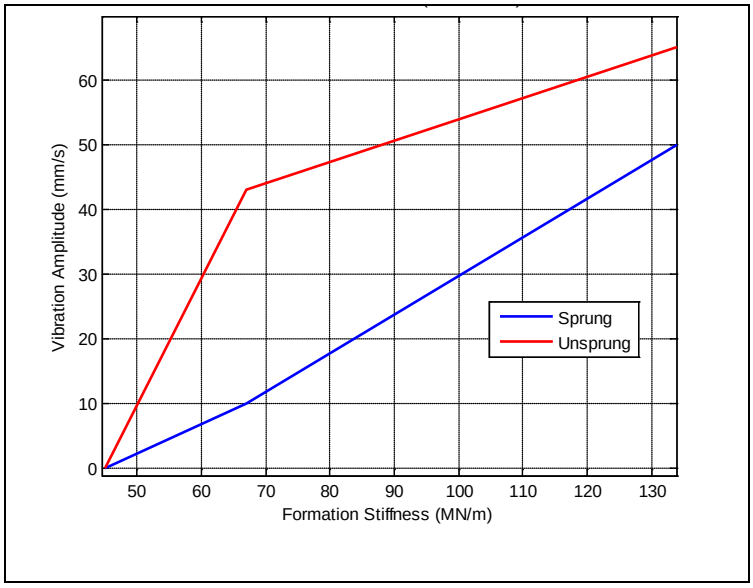

Figure 5.37: Effect of Added Sprung & Unsprung Mass on BHA Vibration (PDC Drillbit & Top Drive Spin Speed = 80 rpm)

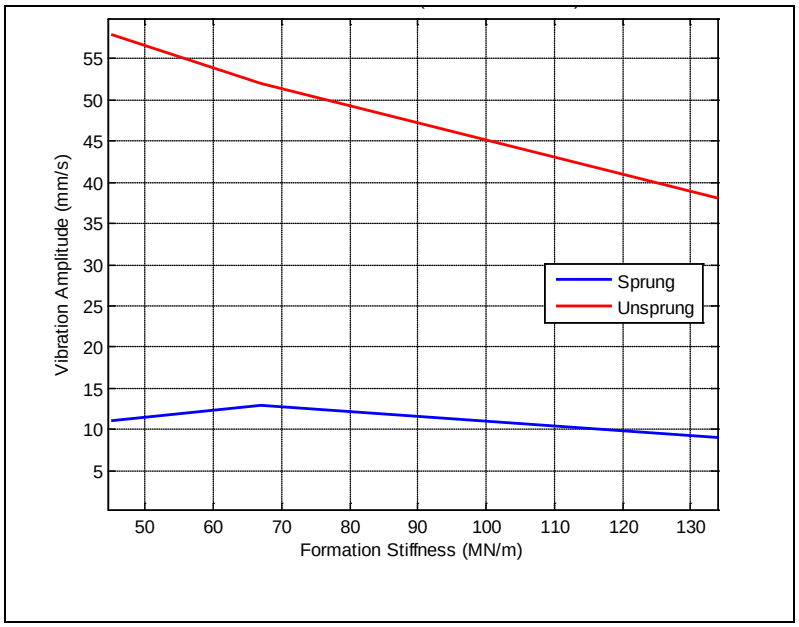

Figure 5.38: Effect of Added Sprung & Unsprung Mass on BHA Vibration (Roller-Cone Drillbit & Top Drive Spin Speed = 80 rpm)

Finally, the PPMD is compared against a standard shock absorber at different values of spin speed and formation stiffness. Elsayed & Aissi [21] provide general guidelines for designing a shock absorber whose equation of motion is given as:

$$m_{abs}\ddot{x}_{abs} + c_{abs}.\left(\dot{x}_{abs} - \dot{x}_{DC}\right) + k_{abs}.\left(x_{abs} - x_{DC}\right) = -\text{WOB} \qquad (5.1)$$

The mass of the shock absorber is utilized in our numerical simulations is 200 kg and its performance is analyzed at values of formation stiffness of 80, 120 and 160 MN/m over a spin speed range of 60 – 140 rpm. For each value of formation stiffness, the values of the shock absorber stiffness and damping were rigorously iterated in order to obtain the values that yielded optimum mitigation of the axial vibrations, as mentioned in Elsayed & Aissi [xx] that this selection should be made very carefully according to the operating conditions. The corresponding values of shock absorber natural frequency and damping ratio were 27 Hz – 0.29, 75 Hz – 0.42, and 185 Hz – 0.65 for the values of formation stiffness of 80, 120 and 160 MN/m, respectively. The mass ratio, natural frequency, and damping ratio of the PPMD are kept constant at all conditions at values of 0.15, 30 rad/s (4.77 Hz) and 0.3, respectively. At each value of spin speed the original vibration is recorded and the percentage reduction is observed utilizing the PPMD, the shock absorber and both the PPMD and shock absorber installed. Tables 5.3, 5.4 and .55 show the observations for values of formation stiffness of 80, 120 and 160 MN/m, respectively. It can be clearly observed that this universal PPMD yields improved reductions in vibration amplitude than the standard shock

absorber and more mitigation is achieved if both the PPMD and shock absorber are implemented together. Hence the universal PPMD is very robust and requires no tuning for different operating conditions unlike the standard shock absorber that is very sensitive to changes in operating conditions. Moreover, installing the PPMD in a BHA that is already equipped with a standard shock absorber mitigates and suppresses axial and torsional vibrations even further and significantly improves drilling efficiency.

Table 5.3: PPMD vs. Shock Absorber Comparison (Formation Stiffness = 80 MN/m)

Spin Speed (rpm)	Vibration Amplitude (mm/s)	% Reduction (Shock Absorber)	% Reduction (PPMD)	% Reduction (Shock Absorber + PPMD)
60	114	18.42	34.21	49.12
70	93	18.28	29.03	53.76
80	74	12.16	20.27	50.00
90	48	22.92	97.92	99.79
100	0.5	60.00	100.00	100.00
110	0.2	100.00	100.00	100.00
120	0.1	100.00	100.00	100.00
130	0.1	100.00	100.00	100.00
140	0.1	100.00	100.00	100.00

Table 5.4: PPMD vs. Shock Absorber Comparison (Formation Stiffness = 120 MN/m)

Spin Speed (rpm)	Vibration Amplitude (mm/s)	% Reduction (Shock Absorber)	% Reduction (PPMD)	% Reduction (Shock Absorber + PPMD)
60	120	6.67	31.67	43.33
70	100	11.00	25.00	40.00
80	86	12.79	19.77	37.21
90	74	10.81	13.51	33.78
100	41	4.88	26.83	34.15
110	28	14.29	32.14	53.57
120	2	75.00	90.00	100.00
130	0.1	100.00	100.00	100.00
140	0.1	100.00	100.00	100.00

Table 5.5: PPMD vs. Shock Absorber Comparison (Formation Stiffness = 160 MN/m)

Spin Speed (rpm)	Vibration Amplitude (mm/s)	% Reduction (Shock Absorber)	% Reduction (PPMD)	% Reduction (Shock Absorber + PPMD)
60	125	3.20	30.40	34.40
70	116	12.07	28.45	37.07
80	101	13.86	26.73	37.62
90	87	14.94	26.44	36.78
100	83	30.12	28.92	40.96
110	77	33.77	42.86	46.75
120	88	48.86	51.14	68.18
130	57	31.58	98.25	100.00
140	0.1	100.00	100.00	100.00

5.3 Lateral-Axial-Torsional Coupling of Drillstring Dynamics

As previously illustrated, the PPMD mitigates and can completely suppress bit-bounce vibrations as well as reducing torsional vibrations of the drillbit. In this section, the capabilities of the PPMD are extended to help mitigate lateral vibrations by further adding lateral springs and dampers between the PPMD and the BHA. There are two main points on the BHA that there is lateral excitation: the center of mass at the midpoint of the BHA and at the bottom near the drillbit due to the lateral component of

WOB. Since the distance between the midpoint and the bottom endpoint of the BHA is 100 m, one lateral PPMD installed at either locations is not enough, and hence at least two PPMDs are required to be installed; one at the center of mass and the other near the drillbit.

The following simulation illustrates the effect of adding combined axial-lateral PPMD on the BHA with PDC drillbit penetrating a hard granite formation of rock stress 170 MPa, when the top drive is spinning at 165 rpm. It is assumed in this simulation that the WOB is inclined at an angle of 3 degrees with respect to the BHA that has an unbalance of 435 kg.m. There are stabilizers at the top, middle, and bottom of the BHA, each with an equivalent damping of 600 N.s/m. Figure 5.39 shows the penetration of the drillbit with and without the PPMD, and Figure 5.40 is a zoom-in to illustrate the slight improvement achieved by extending the PPMD capabilities laterally. Figure 5.41 shows the axial velocity of the drillbit with and without the PPMD, and Figure 5.42 is a zoom-in to illustrate the slight improvement achieved by extending the PPMD capabilities laterally. Figures 5.43 and 5.44 show the lateral orbits at the center of mass and the drillbit, respectively, before and after adding the PPMD.

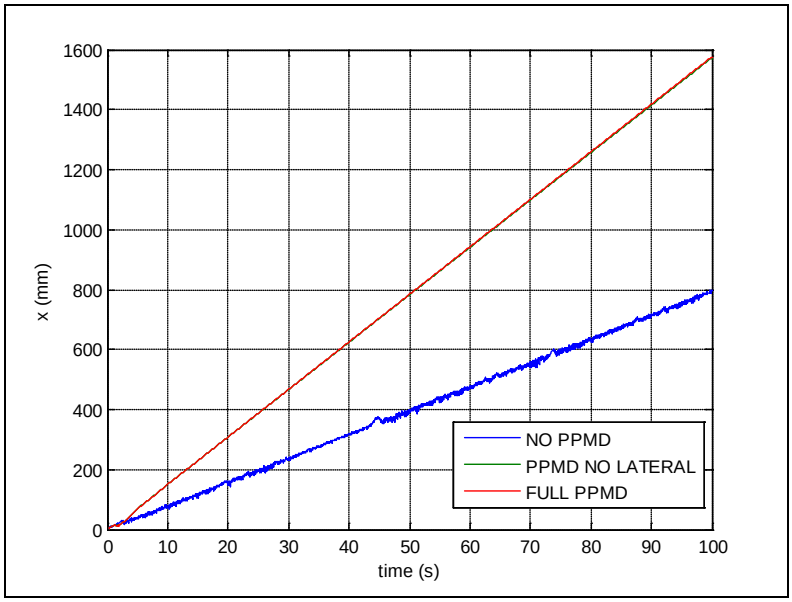

Figure 5.39: Axial Penetration with & without PPMD

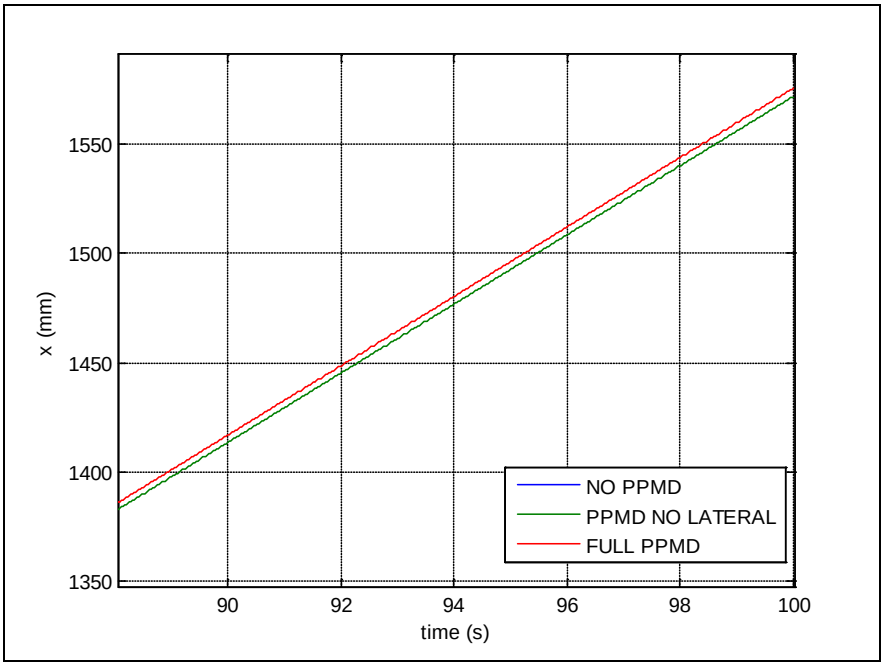

Figure 5.40: Zoom-In on Axial Penetration

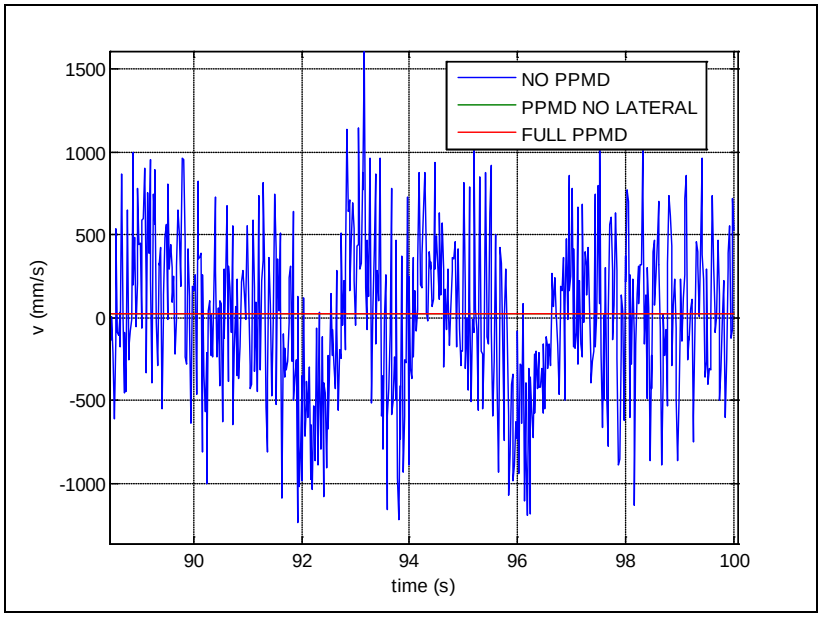

Figure 5.41: Axial Penetration Velocity with & without PPMD

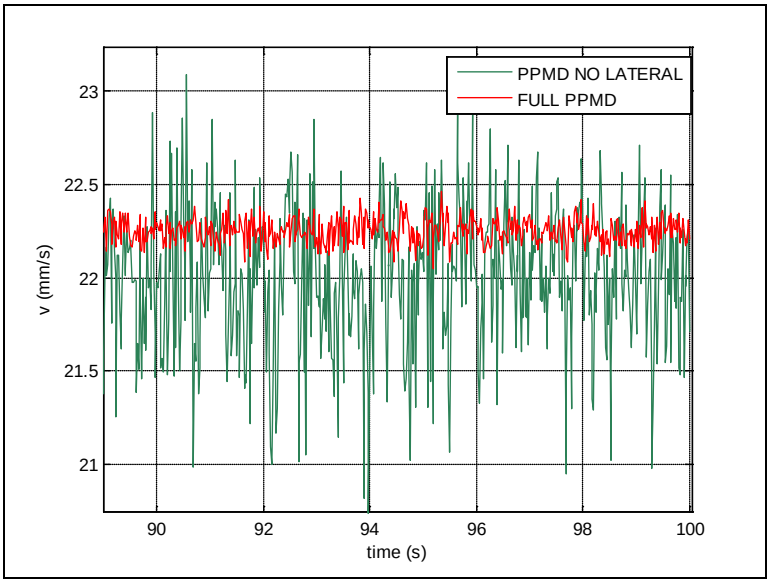

Figure 5.42: Zoom-In on Axial Penetration Velocity

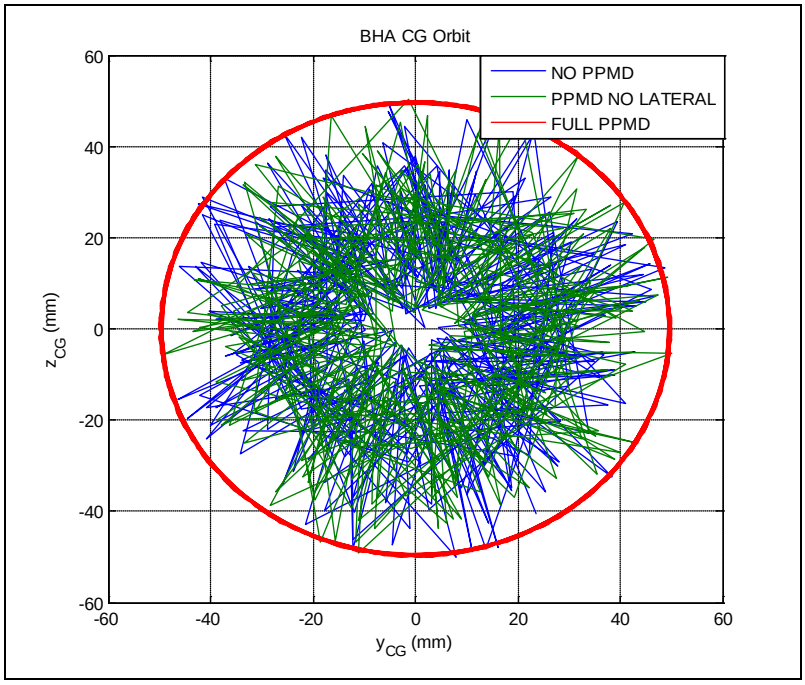

Figure 5.43: BHA Orbit at the Center of Mass with & without PPMD

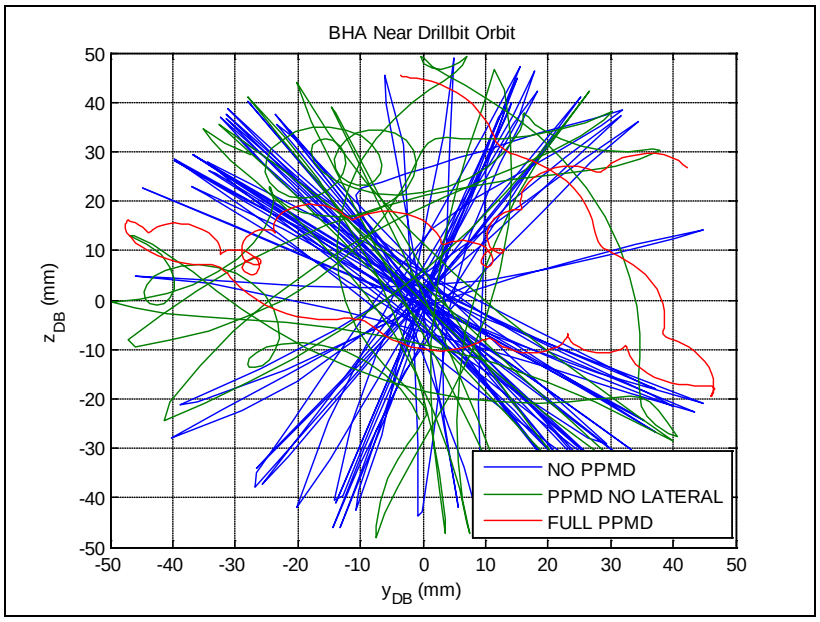

Figure 5.44: BHA Orbit near the Drillbit with & without PPMD

As for the lateral orbit at the center of mass, extending the PPMD to the lateral dimension eliminates the continuous rebounding but the BHA at that point tends to slide along the borehole. In this particular situation, the rate of change in lateral position is equal to the whirling speed, i.e. forward synchronous whirl. However, in other situations, the rate of change of in lateral position maybe in the opposite direction of the whirling speed, which would lead to backward whirl. Backward whirl is undesirable since it can lead to pure rolling contact that leads to harmful reverse bending vibration modes to be induced. Hence, in order to avoid this situation, the stabilizers damping coefficients can be increased to 30000 N.s/m, and hence borehole contact is completely avoided as shown in Figures 5.45 and 5.46.

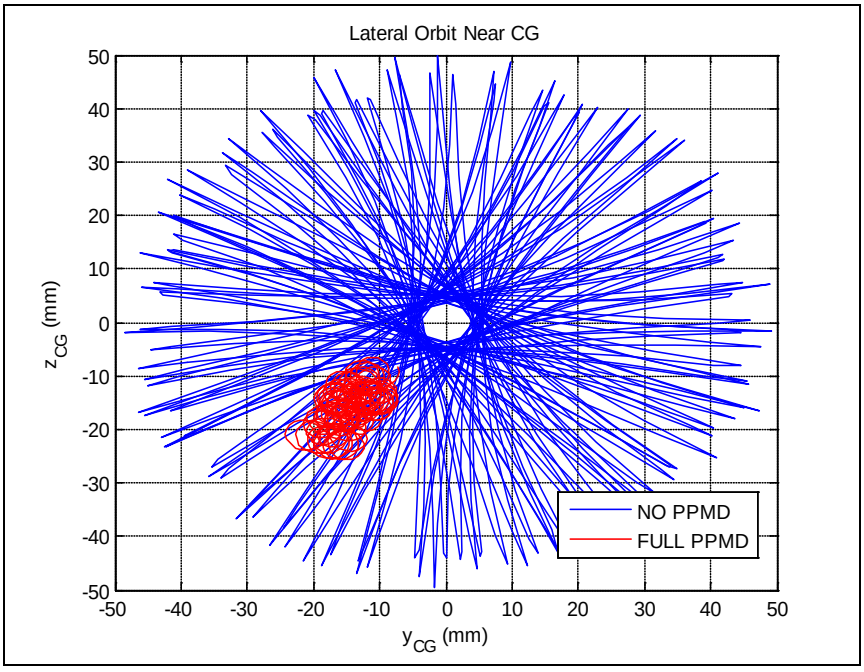

Figure 5.45: Lateral Vibration Reduction at CG after Increasing Stabilizer Damping

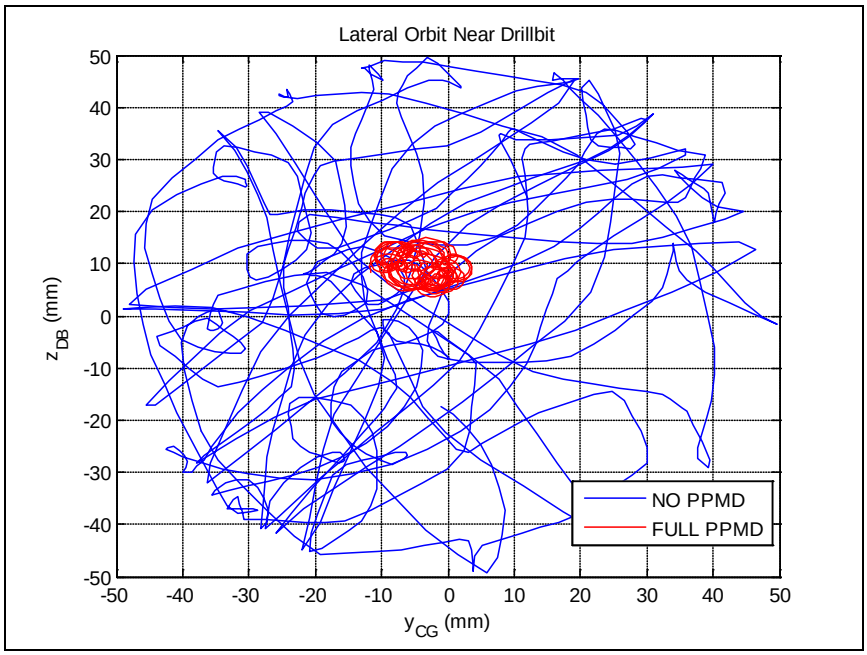

Figure 5.46: Lateral Vibration Reduction near Drillbit after Increasing Stabilizer Damping

The alternative solution would be for the drilling operator to use special downhole tools that are designed to promote forward whirl. One such tool is the V-STAB asymmetric tool manufactured by National Oilwell Varco [54 – 55] that doesn't have any mechanical moving parts, but its V-shaped blades are specially designed to produce contact reaction torques that force the BHA into forward whirl as shown in Figure 5.47.

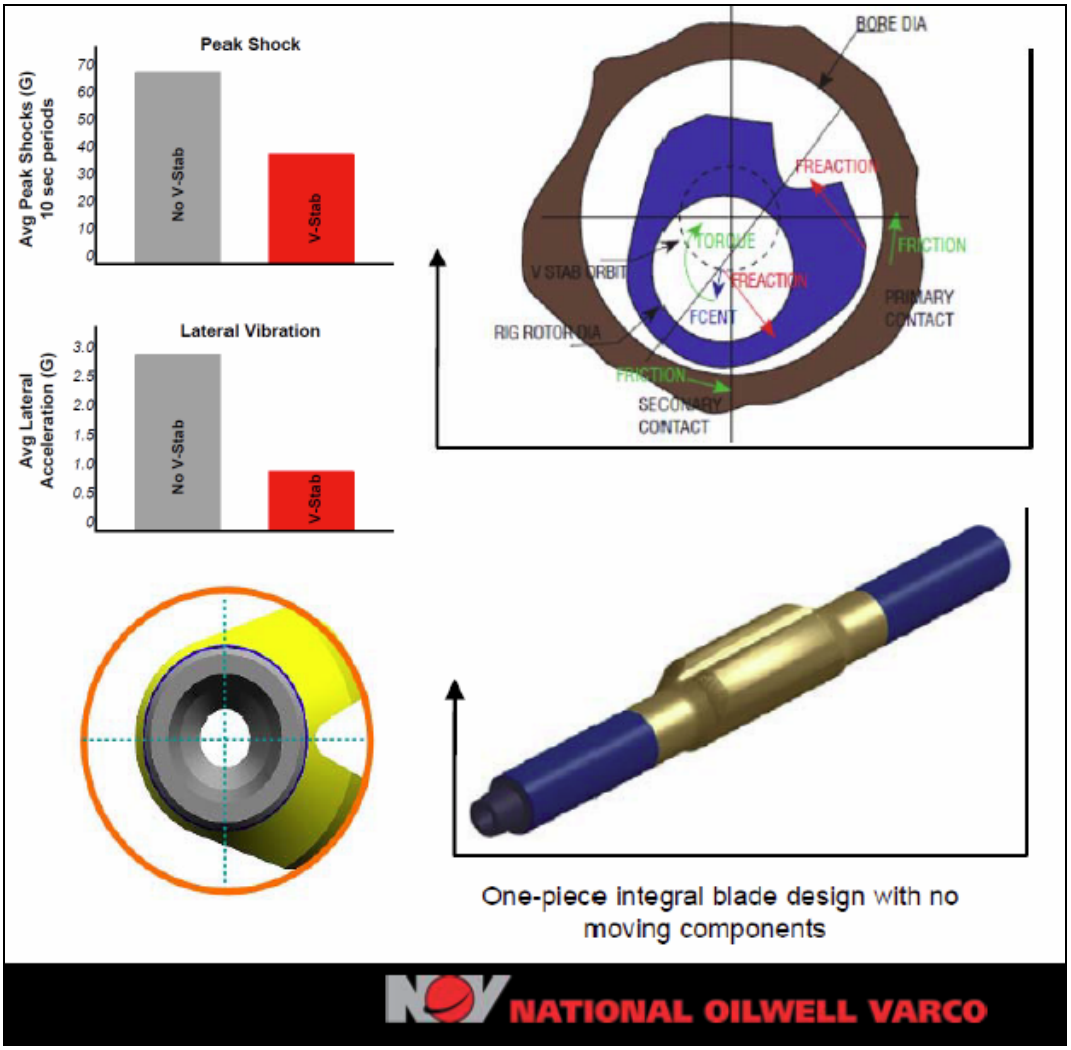

Figure 5.47: V-STAB Asymmetric Tool by National Oilwell Varco [55]

5.4 Downhole Flywheel Design & Levitation in BHA

In Section 2.2, a step-by-step sizing procedure was presented in order to determine the downhole flywheel dimensions and maximum spin speed, in addition to the dimensions of the containment vessels, given the downhole conditions, geometric constraints, and desired power to be stored. The desired energy to be stored is one kW.hr and the flywheel is to be embedded in a 9 inch BHA assembly that allows for at least a 3

inch inner diameter for mudflow, and operating at a downhole pressure of 30 kpsi. Output sizing data after applying this procedure is presented in Table 5.6.

Table 5.6: Output Sizing Data for Flywheel & Containment Vessels

Output Data	**Value**
Flywheel Inner Diameter	4.9”
Flywheel Outer Diameter	6.9”
Flywheel Length	4.4 ft
Flywheel Maximum Spin Speed	30,000 rpm
Flywheel Mass	132 kg
Flywheel Unbalance Eccentricity	5e-6 m
Outer Container Outer Diameter	9”
Outer Container Inner Diameter	7.2”
Inner Container Outer Diameter	3.7”
Inner Container Inner Diameter	3”

Given the parameters of each component in the magnetic levitation closed-control-loop, the stabilizing proportional and derivative gains can be evaluated over a range of equivalent AMB stiffness and damping. In order to make the flywheel less vulnerable to the downhole vibrations, the gains must be increased in order to achieve high values of stiffness and damping. On the other hand, saturation and noise reduction require lower controller gains. Hence, one must obtain a chart of stable operating points

according to the eigenvalues obtained from Equation 2.31. The stabilizing controller gains and their corresponding stiffness and damping are illustrated in Figures 5.48 and 5.49, respectively.

The equivalent AMB stiffness and damping can be obtained from Equations 5.2 and 5.3, respectively.

$$K_{AMB} = G_p.K_{i.}K_{PA}.K_s + K_X \tag{5.2}$$

$$C_{AMB} = G_d.K_i.K_{PA}.K_s \tag{5.3}$$

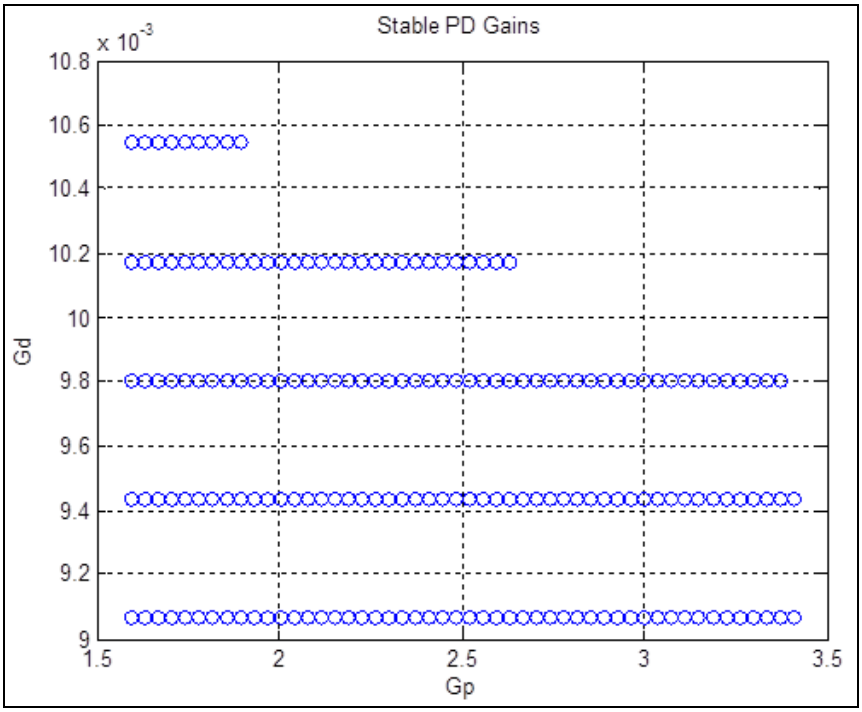

Figure 5.48: Stabilizing PD Controller Gains

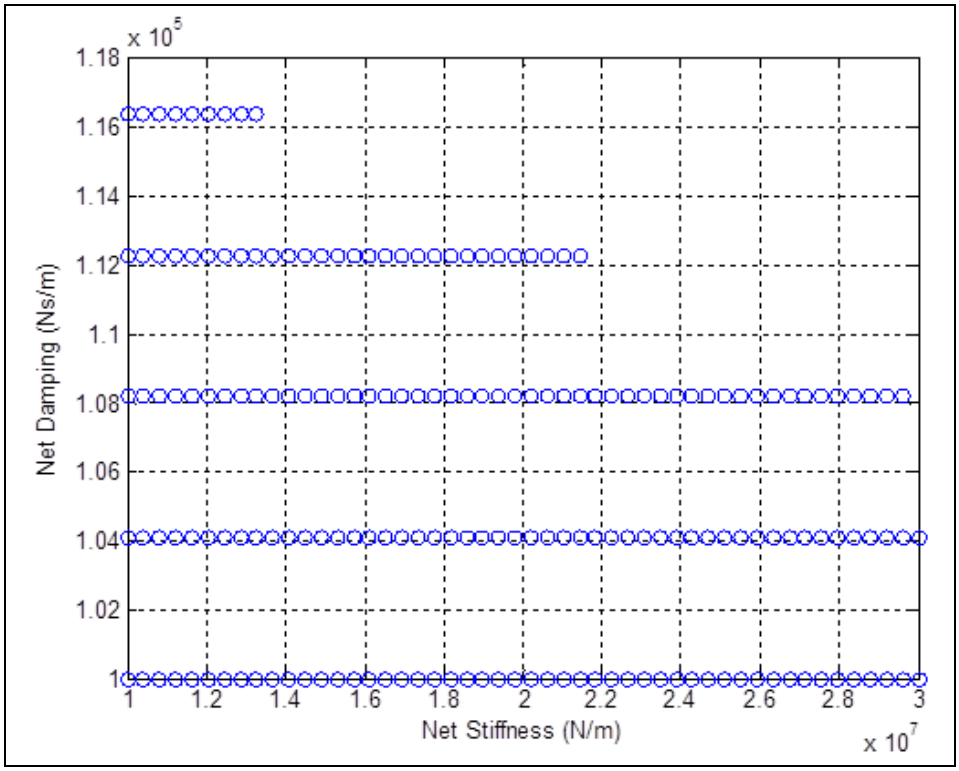

Figure 5.49: Stable Equivalent AMB Stiffness & Damping Values

The flywheel must maintain levitation and avoid hitting the catcher bearings due to the disturbance caused by the external downhole vibrations, in addition to the mass unbalance of the flywheel rotor. Equation 2.31 is numerically integrated to determine the time response of all components and sub-systems. The simulation parameters are listed in Table 5.7.

Table 5.7: Simulation Parameters for Flywheel Embedded in BHA

Parameter Description	**Parameter Symbol**	**Numerical Value**
Controller Proportional Gain	G_p	0.75 (Radial) 6 (Axial)
Controller Derivative Gain	G_d	0.0024 (Radial) 0.00181 (Axial)
Controller Time Constant	τ_{pd}	1/13000
Forward Power Amplifier Gain	k_{PA}	942
Feedback Power Amplifier Gain	γ	0.997
Overall Power Amplifier Gain	K_{PA}	1
Coil Inductance	L	0.15 H
Coil Resistance	R	2 Ohms (Radial) 2.4 Ohms (Axial)
Coil Voltage Saturation Limit	V_{sat}	150 V
Coil Current Saturation Limit	I_{sat}	20 A
AMB Current Stiffness	K_i	1400 N/A (Radial) 1450 N/A (Axial)
AMB Position Stiffness	K_x	-7.609x10^6 N/m (Radial) - 10x10^6 N/m (Axial)
Feedback Sensor Gain	K_S	7840 V/m
Sensor Time Constant	τ_{ps}	1/31000

Table 5.7 Continued

Flywheel Rotation Speed	$\boldsymbol{\omega_{FW}}$	30,000 rpm
BHA Effective Mass	$\boldsymbol{m_d}$	0.87e5 kg
Applied Axial Load	$\boldsymbol{W_0}$	100 kN
Top Drive Spin Speed	$\boldsymbol{\omega_d}$	180 rpm
BHA Torsional Stiffness-to-Ground	$\boldsymbol{k_T}$	600 N.m/rad
BHA Torsional Damping-to-Ground	$\boldsymbol{c_T}$	500 N.s.m/rad
Rock Formation Stiffness	$\boldsymbol{k_c}$	100 MN/m
Drillbit Radius	$\boldsymbol{a}$	0.15 m
Mean Friction Coefficient	$\boldsymbol{\mu_0}$	0.06
ROP Factor	$\boldsymbol{c_1}$	1.35e-8
ROP Factor	$\boldsymbol{c_2}$	-1.9e-4

Figures 5.50 and 5.51 show the lateral orbits of the relative displacements at each magnetic bearing and it can be noted that the maximum relative displacement is less than the 0.35 mm catcher bearing clearance value.

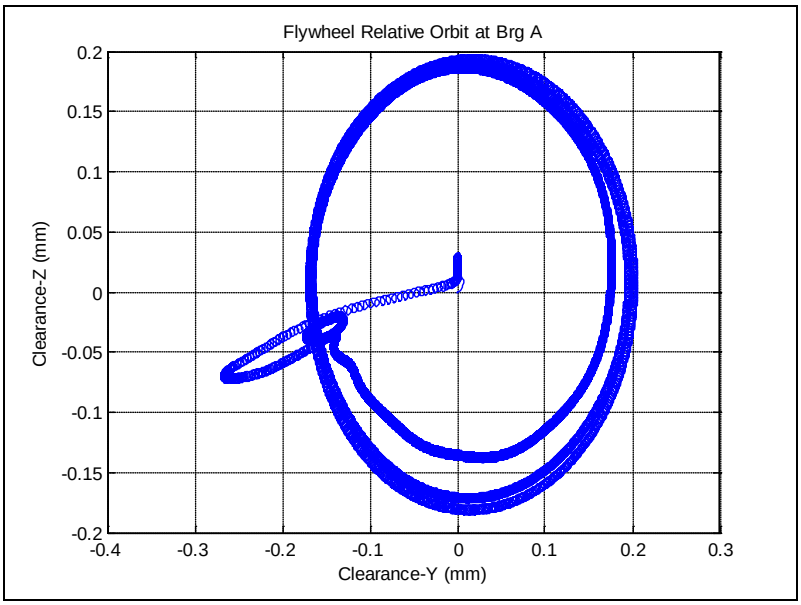

Figure 5.50: Relative Lateral Orbit at Magnetic Bearing A

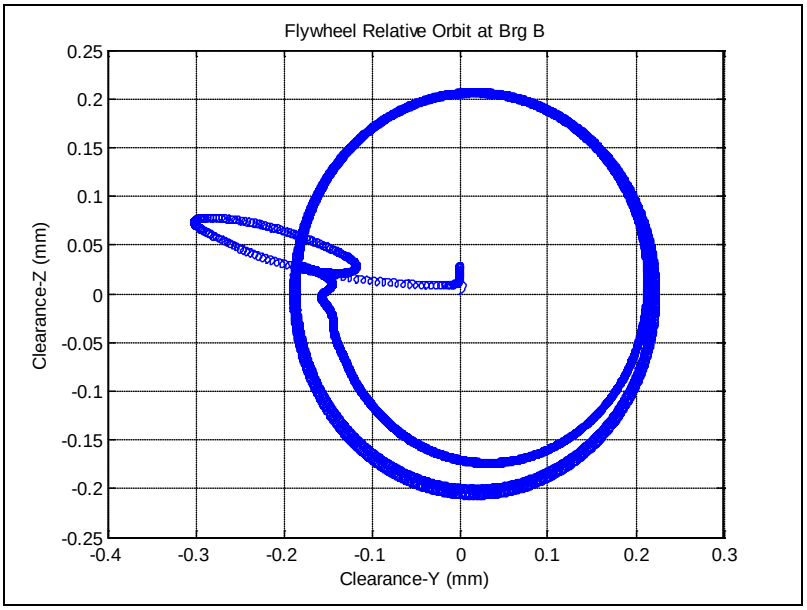

Figure 5.51: Relative Lateral Orbit at Magnetic Bearing B

The BHA lateral orbits where the magnetic bearings are attached are illustrated in Figures 5.52 and 5.53.

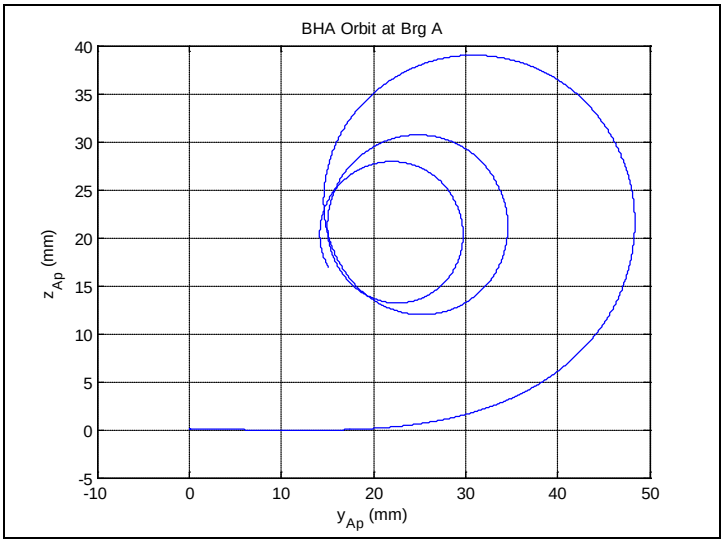

Figure 5.52: BHA Lateral Orbit at Magnetic Bearing A

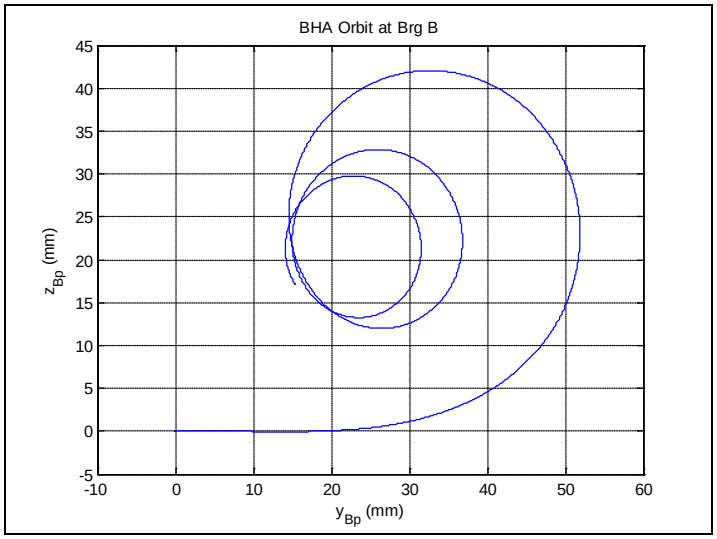

Figure 5.53: BHA Lateral Orbit at Magnetic Bearing B

The tricone drillbit axial velocity is shown in Figure 5.54 and Figure 5.55 shows the relative axial displacement at the axial magnetic bearing, demonstrating that the flywheel maintains axial levitation due to bit-bounce.

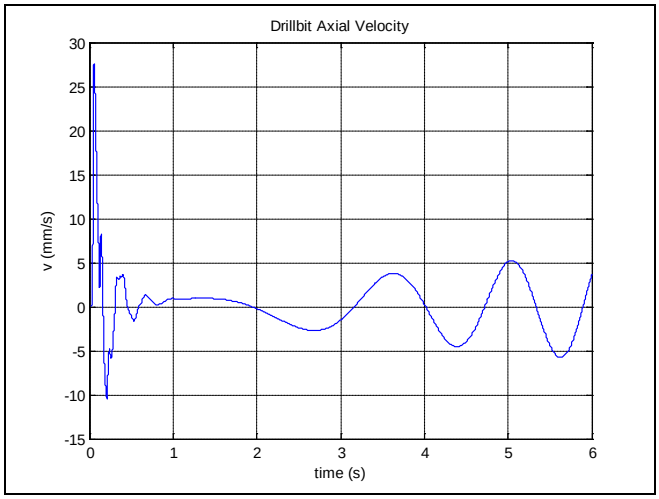

Figure 5.54: Drillbit Axial Velocity

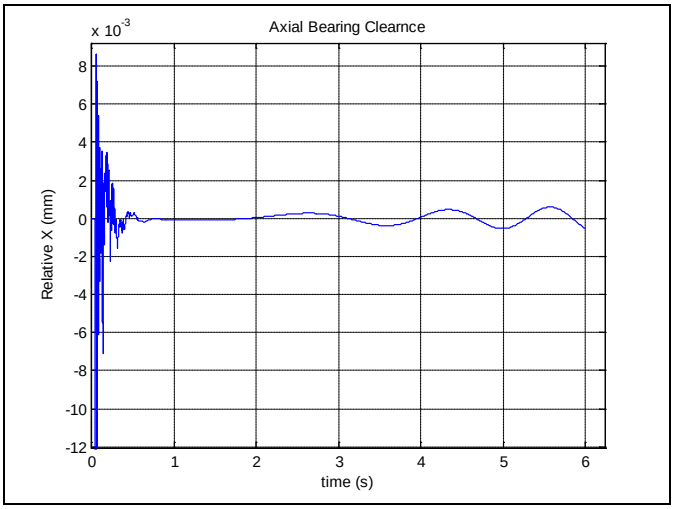

Figure 5.55: Relative Clearance at Axial Magnetic Bearing

Figures 5.56 through 5.57 show the controller voltages, AMB coil currents, power amplifier voltages, and AMB actuation forces, respectively, for each of the five axes of the magnetic levitation control system.

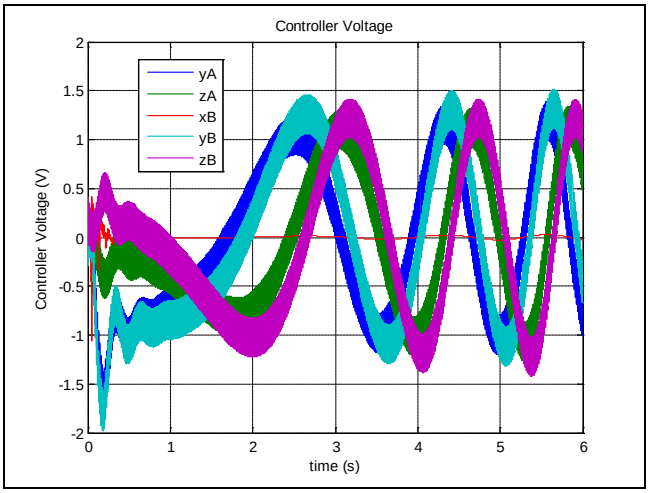

Figure 5.56: Controller Voltages for Each Control Axis

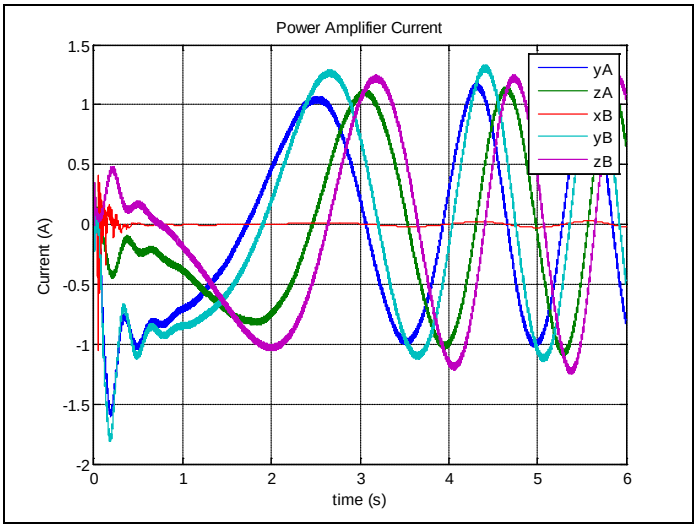

Figure 5.57: AMB Coil Current per Axis

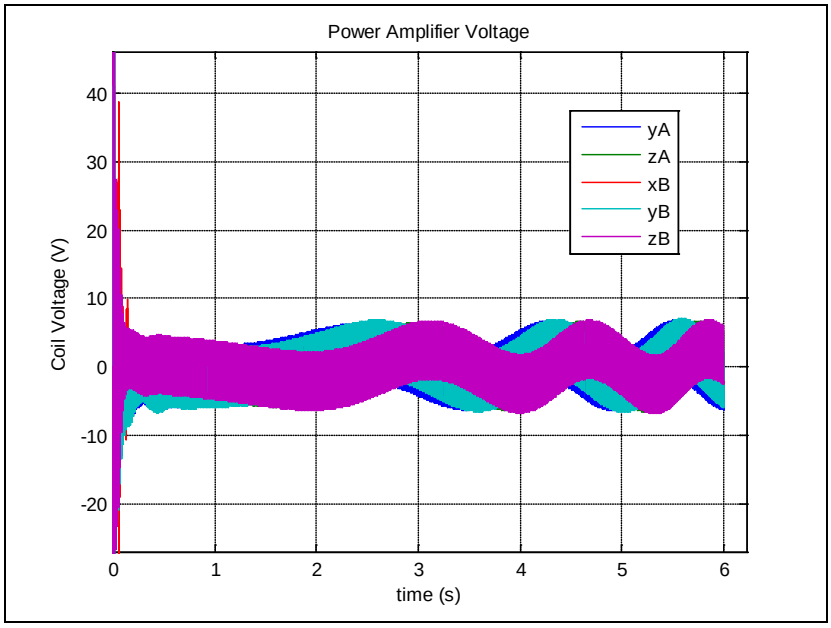

Figure 5.58: Power Amplifier Voltage per Axis

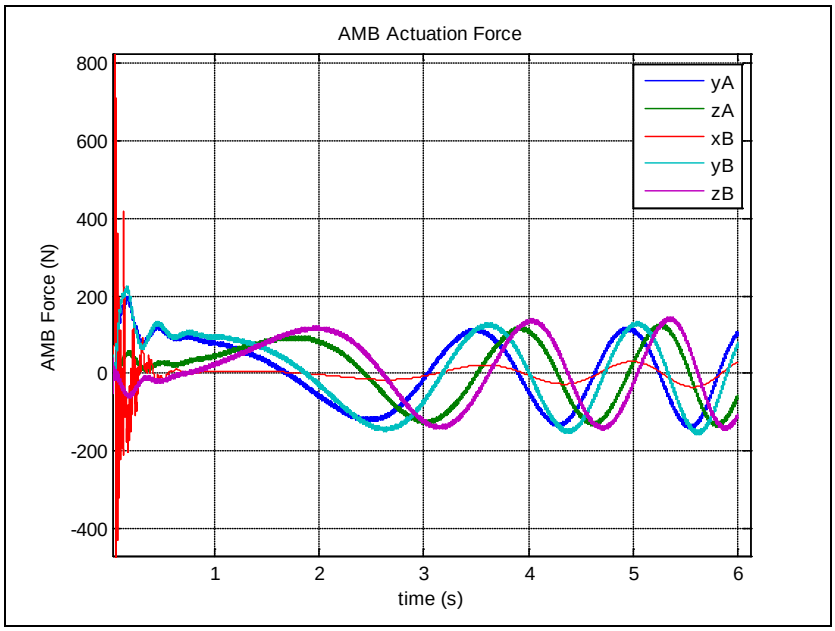

Figure 5.59: AMB Actuation Forces per Axis

It is to be mentioned that a notch filter, tuned at a frequency of 500 Hz with a quality factor of 20 was utilized in order to mitigate the high frequency component especially with respect to the power amplifier current. There are two harmonics in the response; a low frequency component of 0.8 Hz due to the external excitation on the BHA, and a high frequency component of 500 Hz due to the mass unbalance of the flywheel rotating at 30,000 rpm. Adding a low-pass filter will eliminate the high frequency component but will destabilize the system, and thus a notch filter tuned at the same frequency of the excitation source, i.e. 500 Hz corresponding to the 30,000 rpm spin rate of the flywheel would be the alternative.

In order to demonstrate the robustness of the magnetic levitation control system, a destabilizing lateral cross-coupling stiffness component is introduced at the BHA where the AMBs are fixed in order to induce a chaotic orbit. Figures 5.60 and 5.61 show the lateral orbits of the BHA at both bearing locations, and Figures 5.62 and 5.63 show the relative lateral orbits and it can be observed that the maximum relative lateral displacement doesn’t exceed the proposed clearance of 0.35 mm. By doubling the values of the proportional and derivative gains of the controller on the radial axes, the size of the relative orbit can be further reduced to approximately 0.1 mm as shown in Figures 5.64 and 5.65. The controller voltages, AMB coil currents, power amplifier voltages, and AMB actuating forces are shown in Figures 5.66 through 5.69, respectively.

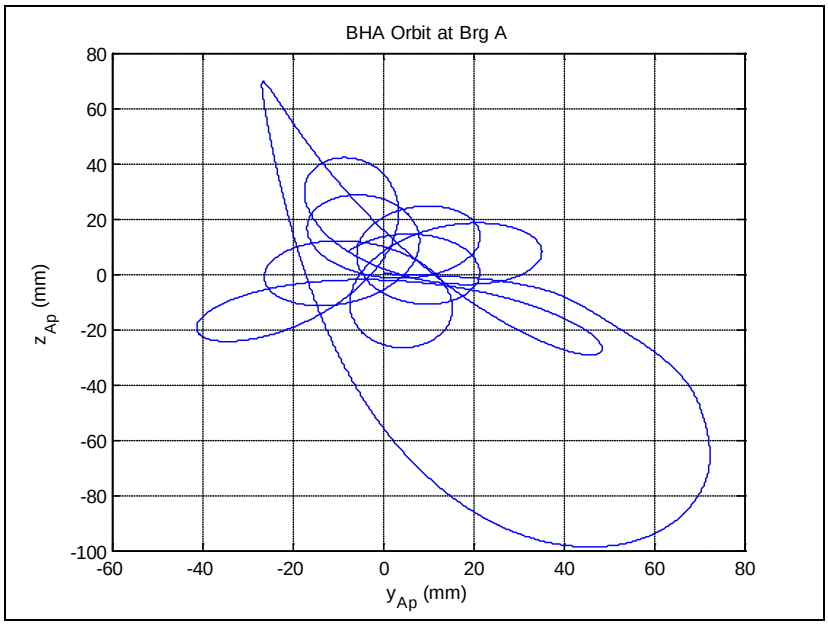

Figure 5.60: BHA Lateral Orbit at Bearing A (Destabilizing Case)

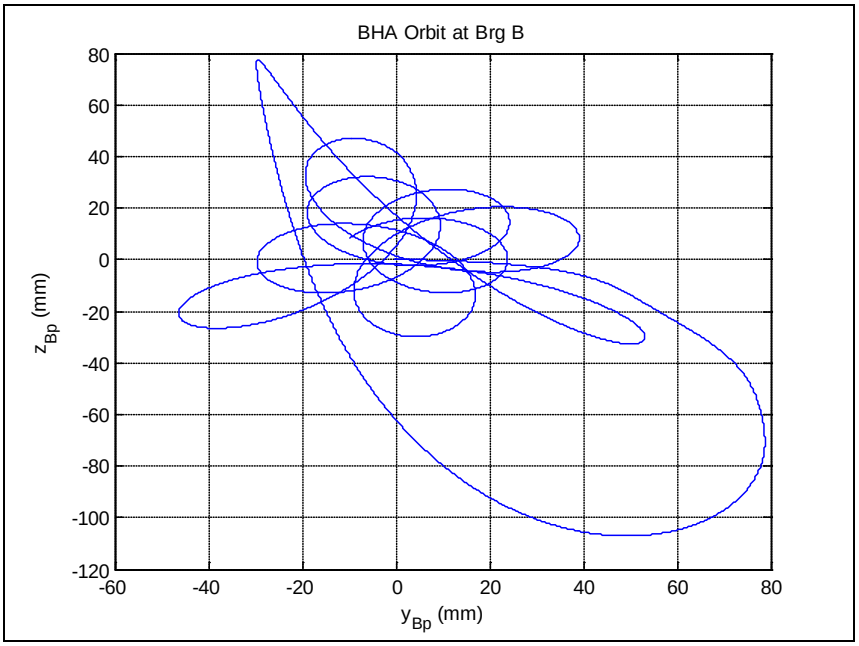

Figure 5.61: BHA Lateral Orbit at Bearing B (Destabilizing Case)

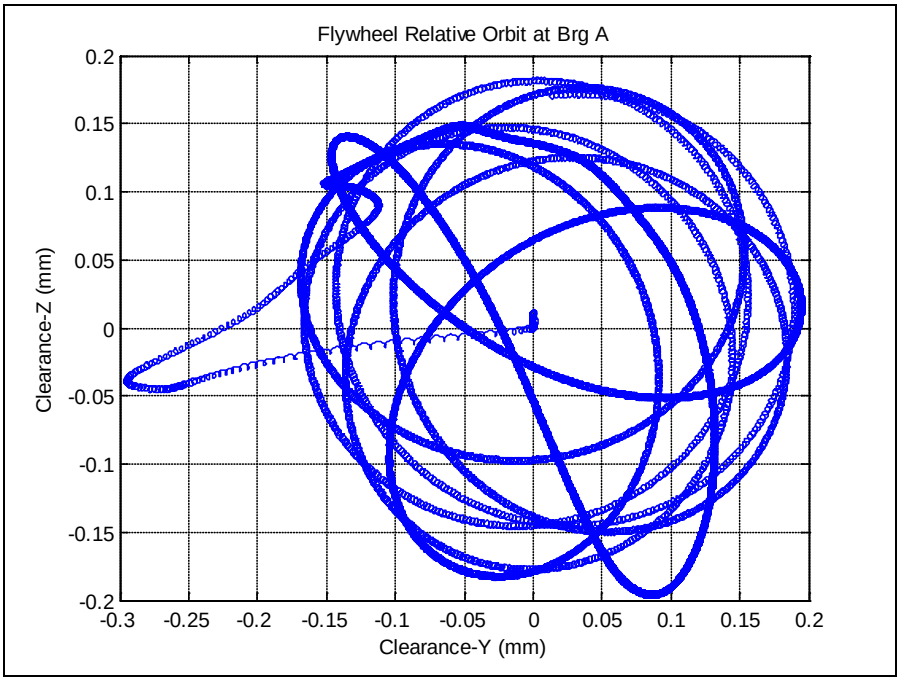

Figure 5.62: Relative Lateral Orbit at Bearing A (Destabilizing Case)

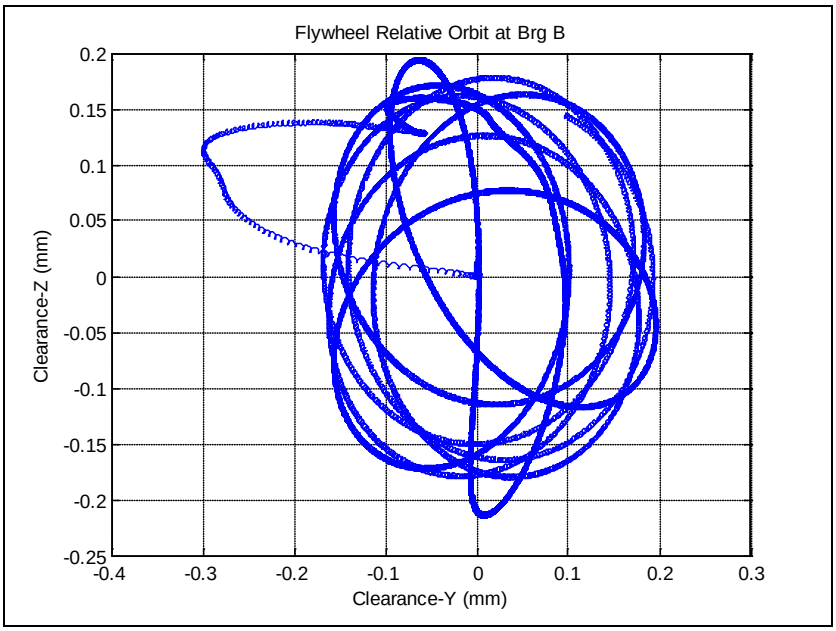

Figure 5.63: Relative Lateral Orbit at Bearing B (Destabilizing Case)

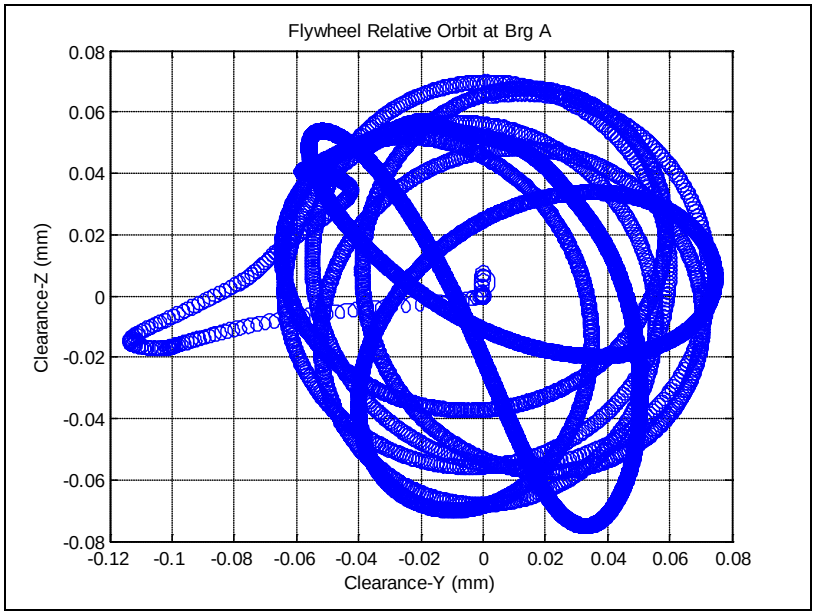

Figure 5.64: Reduced Relative Lateral Orbit at Bearing A (Destabilizing Case)

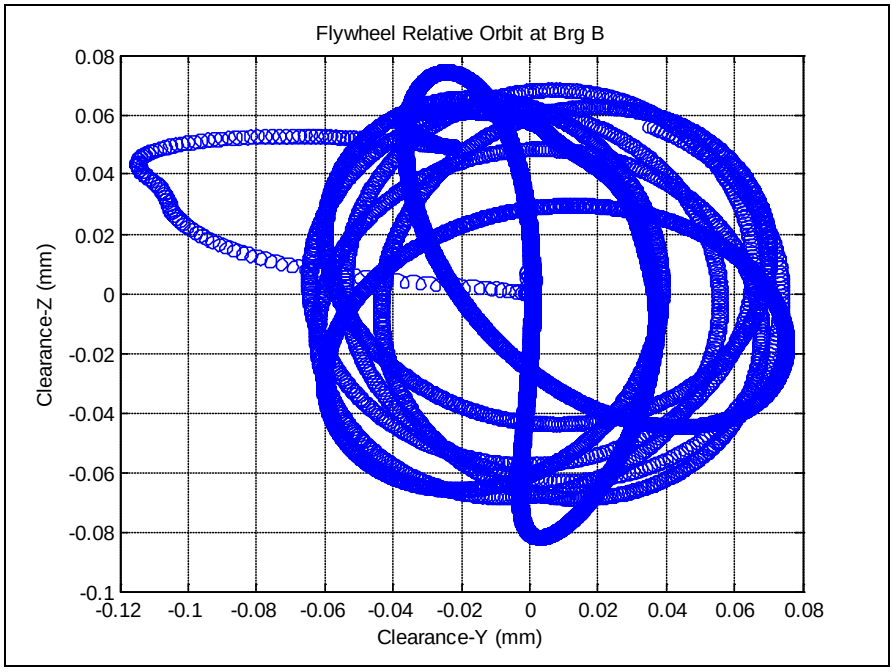

Figure 5.65: Reduced Relative Lateral Orbit at Bearing B (Destabilizing Case)

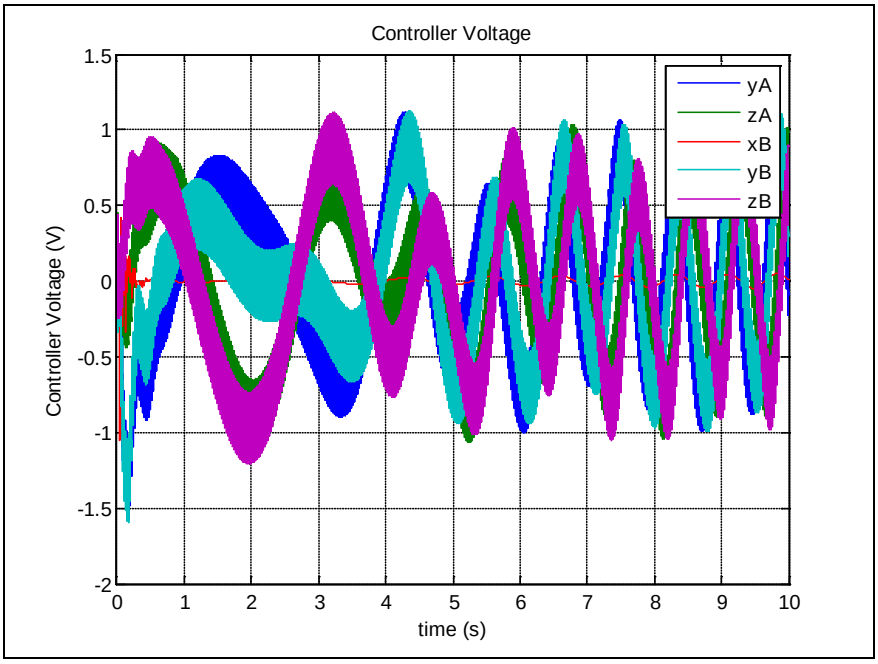

Figure 5.66: Controller Voltages per Axis (Destabilizing Case)

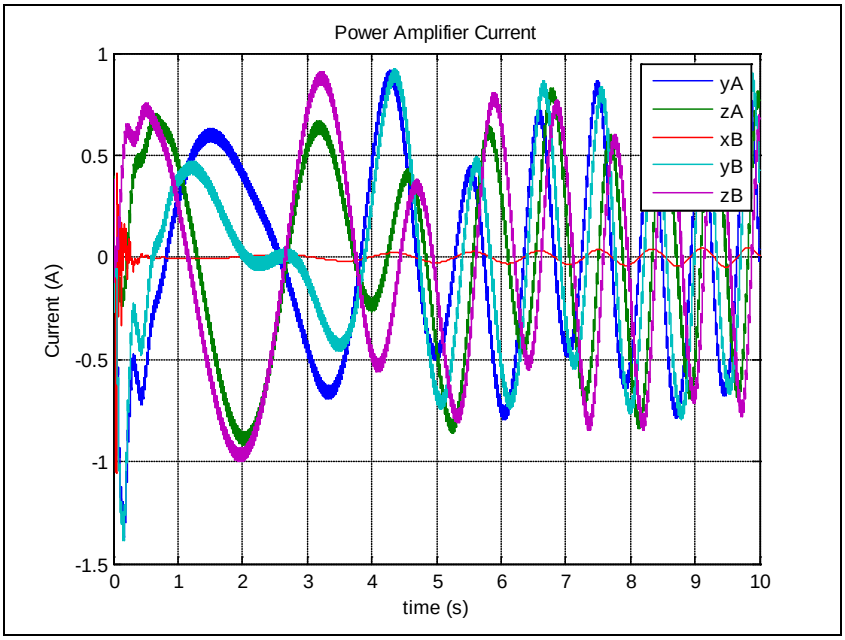

Figure 5.67: AMB Coil Currents per Axis (Destabilizing Case)

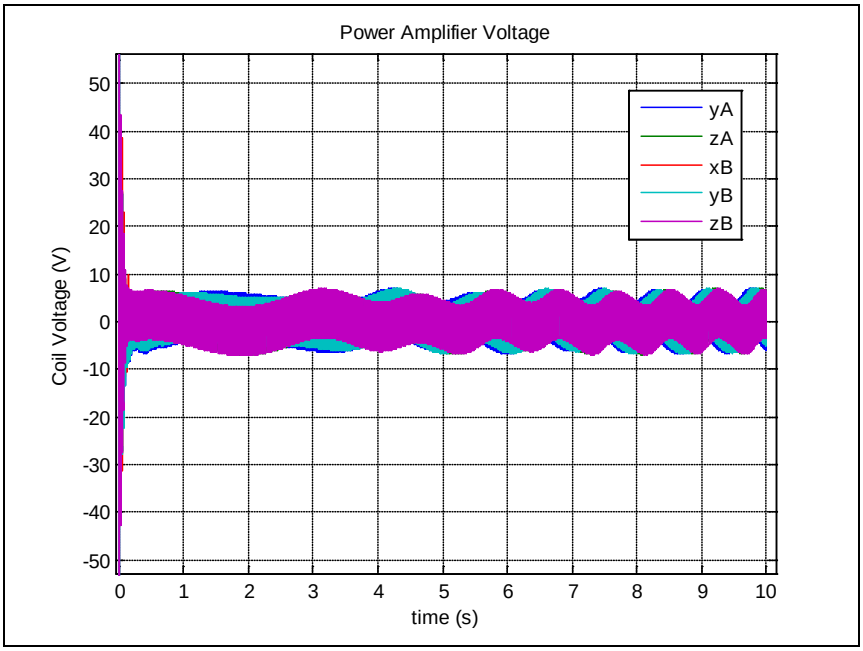

Figure 5.68: Power Amplifier Voltages per Axis (Destabilizing Case)

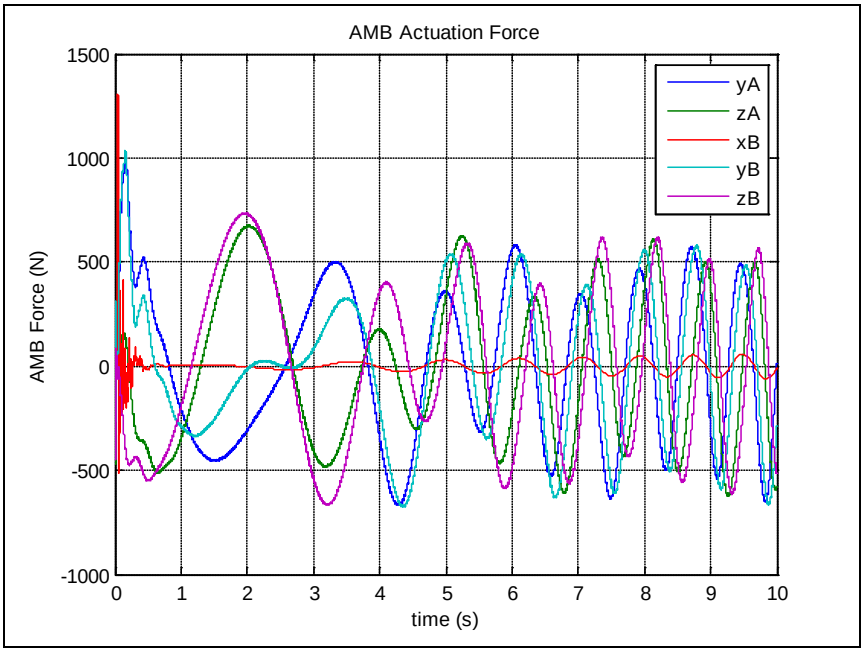

Figure 5.69: AMB Actuation Forces per Axis (Destabilizing Case)

By adding a 5 mV random noise signal at the sensor, the power amplifier voltage is still below the 150 V saturation limit but the response of the system remains almost unchanged. Figures 5.70 – 5.72 show that plots of the controller voltage, power amplifier current, and AMB actuating forces respectively. Figures 5.73 and 5.74 show the plot of the power amplifier voltage when the values of the controller gains after and before being doubled, respectively.

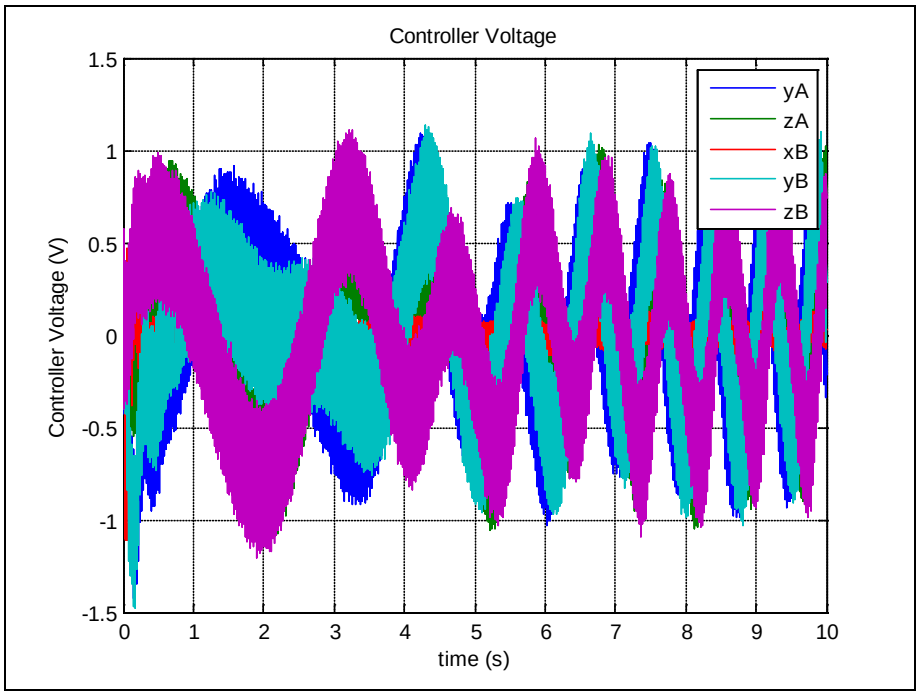

Figure 5.70: Controller Voltage after Adding 5 mV Sensor Noise

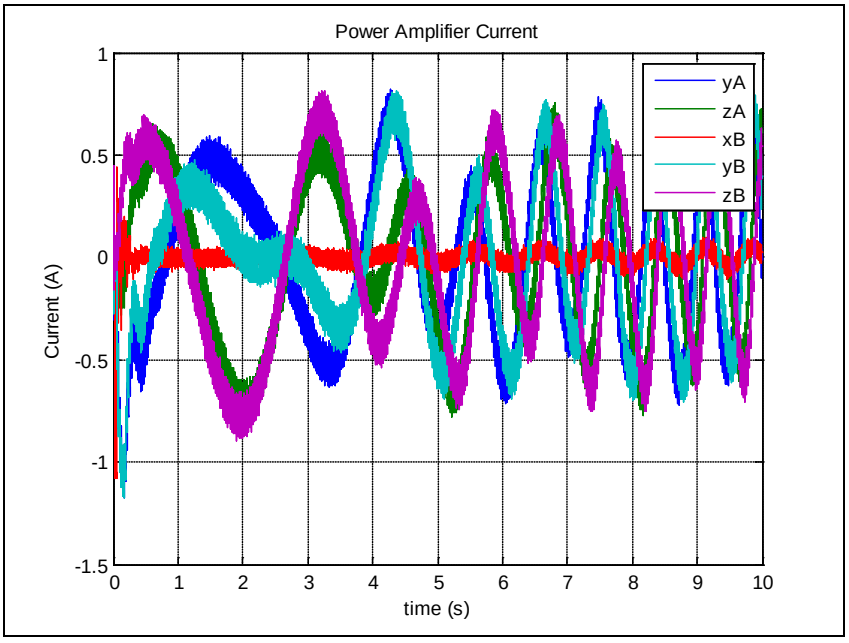

Figure 5.71: AMB Coil Current after Adding 5 mV Sensor Noise

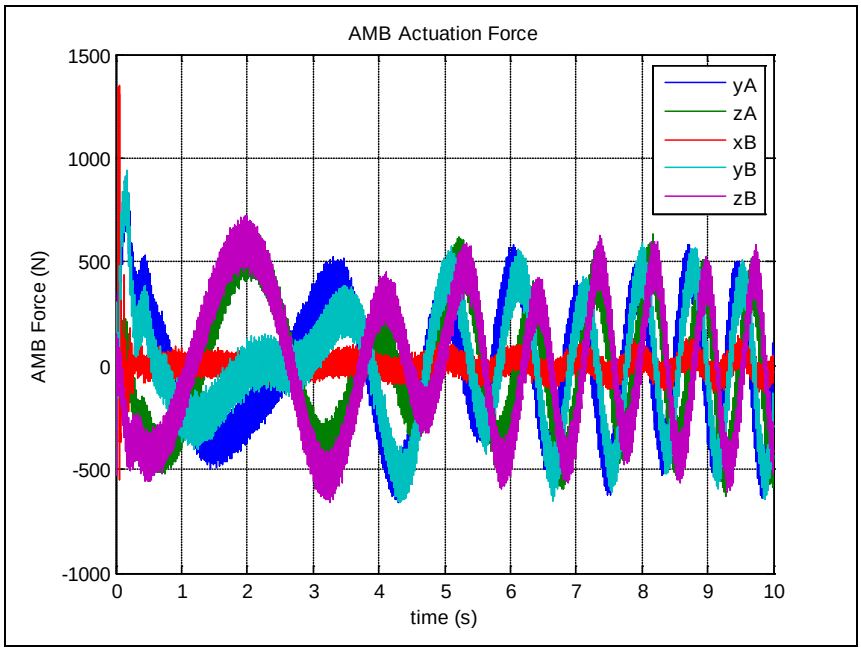

Figure 5.72: AMB Actuating Forces after Adding 5 mV Sensor Noise

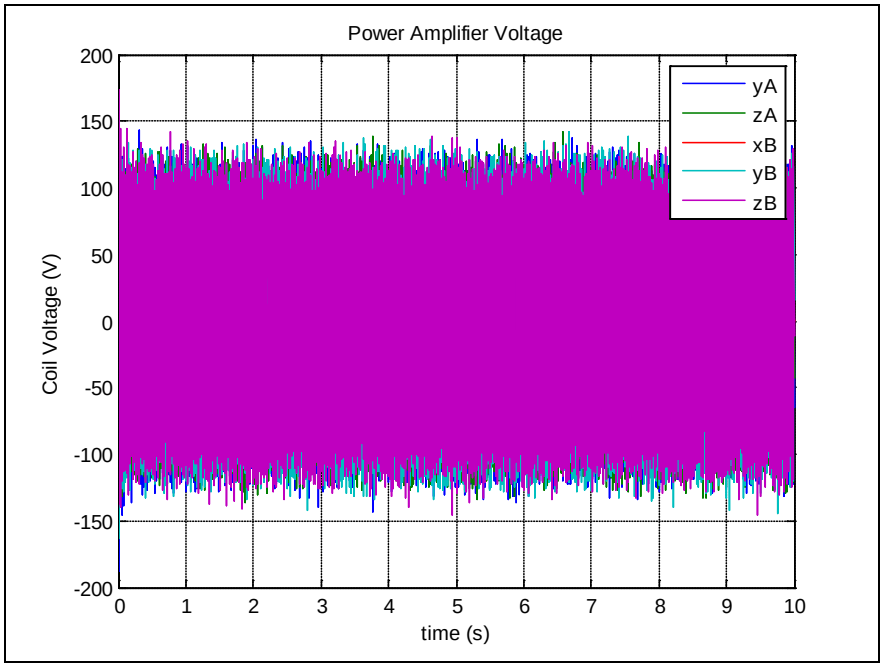

Figure 5.73: Power Amplifier Voltage with Noise after Doubling Controller Gains

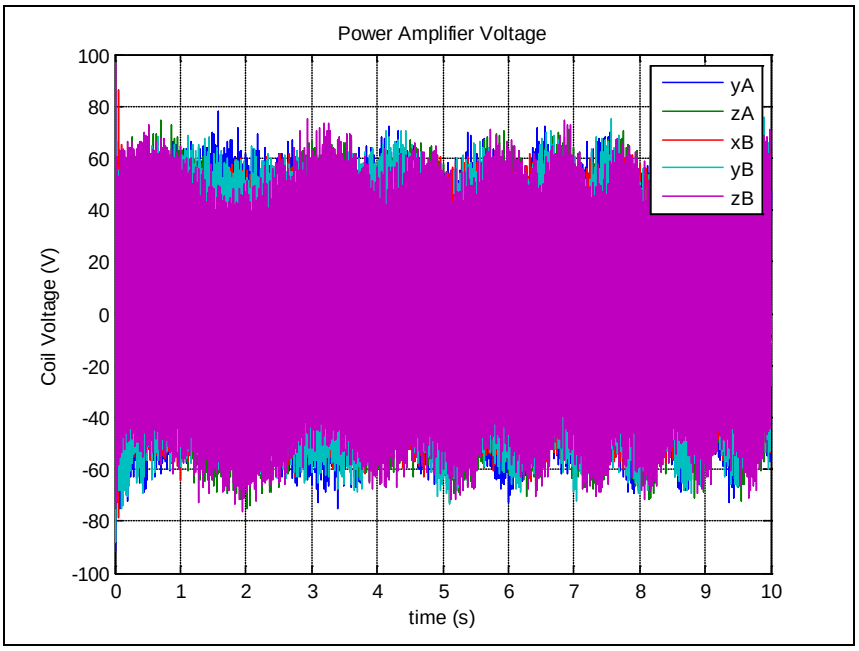

Figure 5.74: Power Amplifier Voltage with Noise before Doubling Controller Gains

5.5 Extension of Flywheel Capabilities to Act as APMD

Previously it was demonstrated that a passive proof mass damper whose mass can be determined according to the mass of the BHA, can mitigate and suppress bit-bounce vibrations, as well as mitigating torsional vibrations. Moreover, it was also demonstrated that an embedded flywheel inside the BHA can successfully maintain levitation during bit-bounce and stick-slip vibrations, as well as lateral vibrations. It can be noted that the equivalent AMB stiffness and damping values are equal to or greater than those utilized in the PPMD. Thus, if a number of flywheel modules are installed such that the their total mass is approximately 7 – 15 % of the BHA mass, the flywheels can act as active proof-mass-dampers (APMD) via the action of the axial AMB in order to mitigate/suppress bit-bounce vibrations. Hence, the idea of conceiving an APMD is possible for light BHAs utilized in drilling softer rock formations, since the mass of each flywheel is 132 kg. In the following example, a light BHA weighing 8500 kg is utilized to drill a soft formation of stiffness 25 MN/m (44 MPa rock cutting stress) using a PDC drillbit, and the top drive is spinning at 170 rpm. Figures 5.75 and 5.76 show the axial and rotary spin velocities of the drillbit, respectively, before adding proof-mass-damping. In order to suppress the vibrations, 4 flywheel modules are added, each module contributes equivalent stiffness and damping values of 5.8e7 N/m and 2e4 N.s/m, respectively, in the axial direction by using the controller gains listed in Table 5.4. A lumped mass model was utilized in the simulation by taking into consideration the dynamics of the power amplifier. Figures 5.77 and 5.78 show the axial and rotary speeds, respectively of the drillbit after adding the 4 flywheel modules. Figure 5.79

shows the relative displacement between each flywheel and the BHA, and it can be seen that the maximum displacement is less than 0.3 mm (i.e. less than the 0.35 mm catcher bearing clearance).

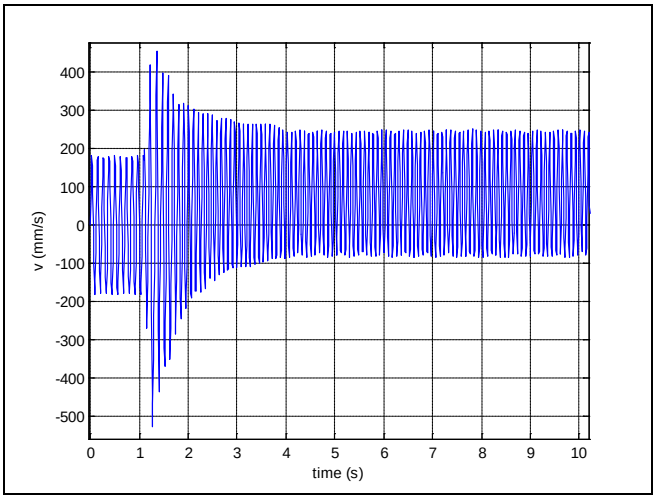

Figure 5.75: Axial Velocity of the Drillbit before Adding the APMD

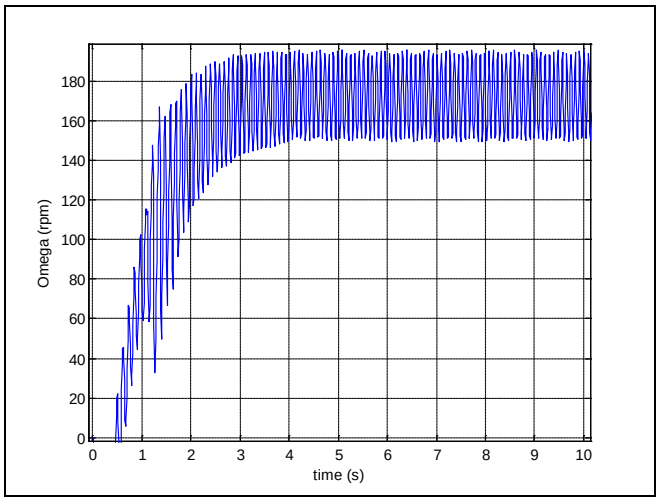

Figure 5.76: Rotary Velocity of the Drillbit before Adding the APMD

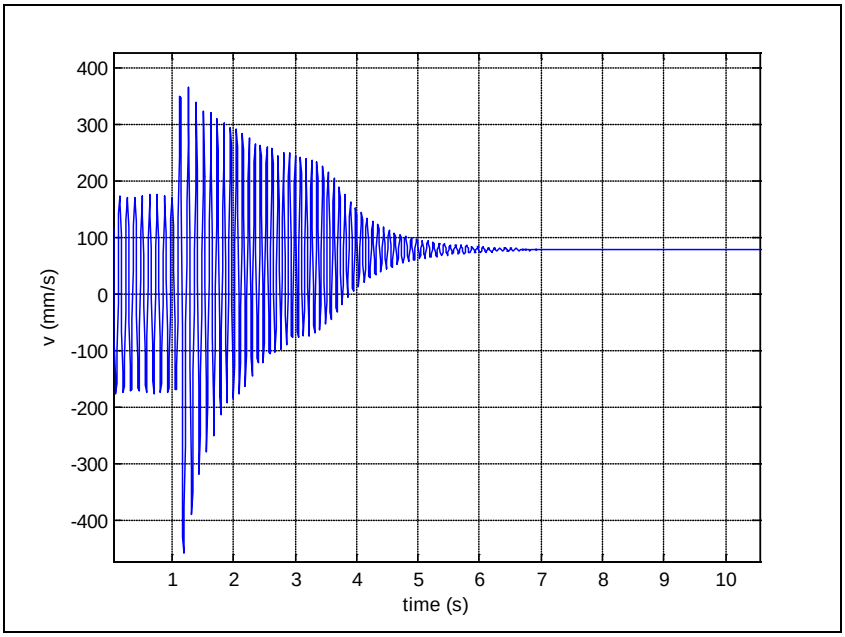

Figure 5.77: Axial Velocity of Drillbit after Adding APMD

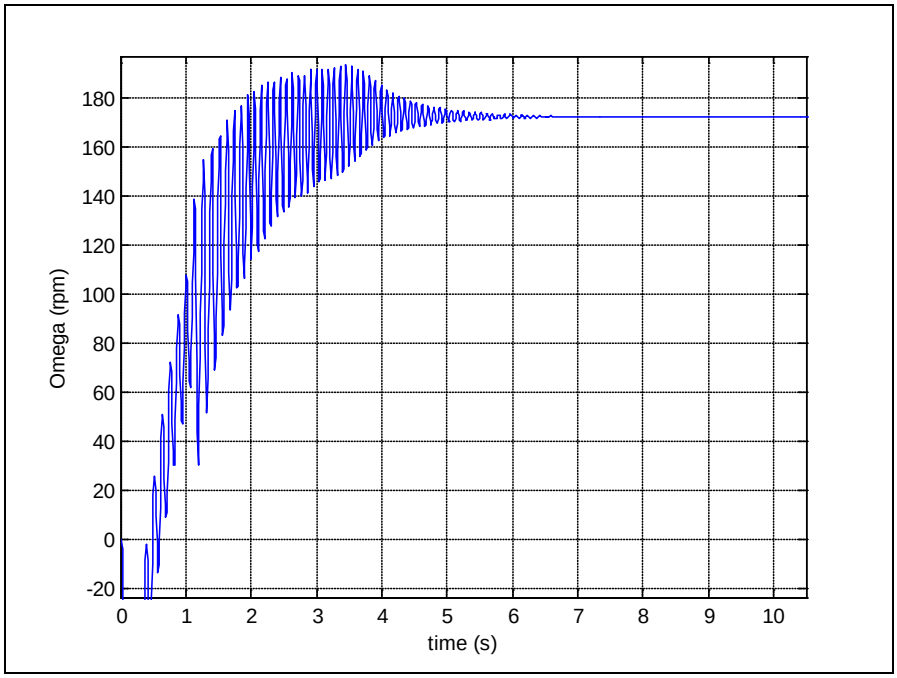

Figure 5.78: Rotary Velocity of Drillbit after Adding APMD

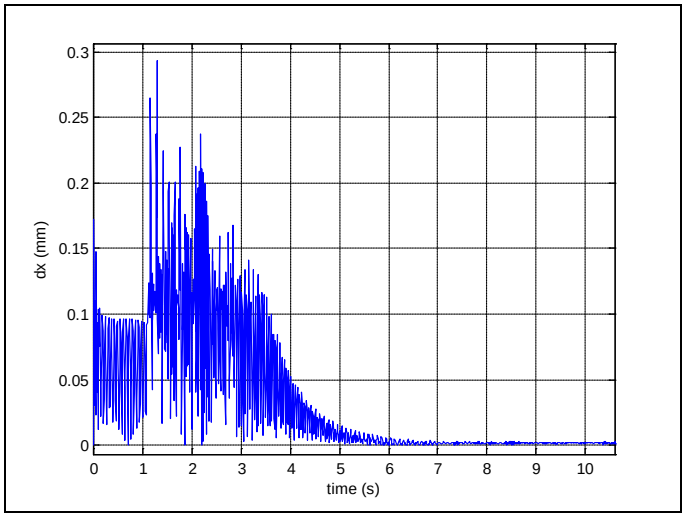

Figure 5.79: Absolute Relative Displacement after Adding APMD

The axial AMB coil current, actuator force, and power amplifier voltage are shown in Figures 5.80 through 5.82, respectively.

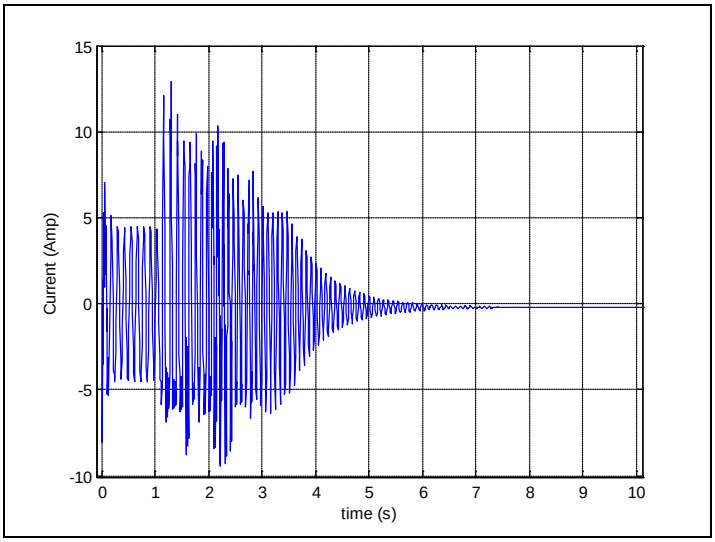

Figure 5.80: Axial AMB Coil Current after Adding APMD

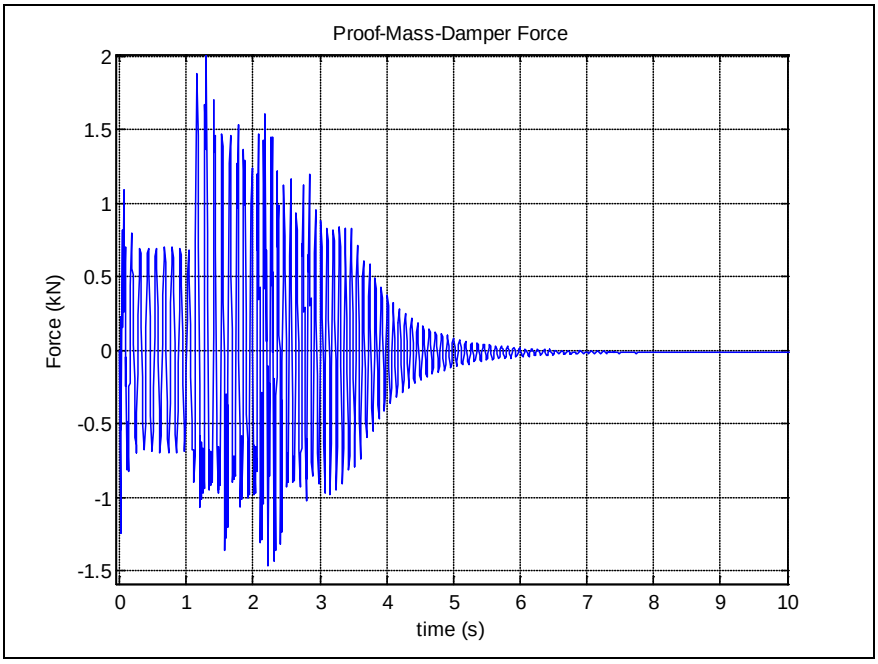

Figure 5.81: Axial Actuating Force after Adding APMD

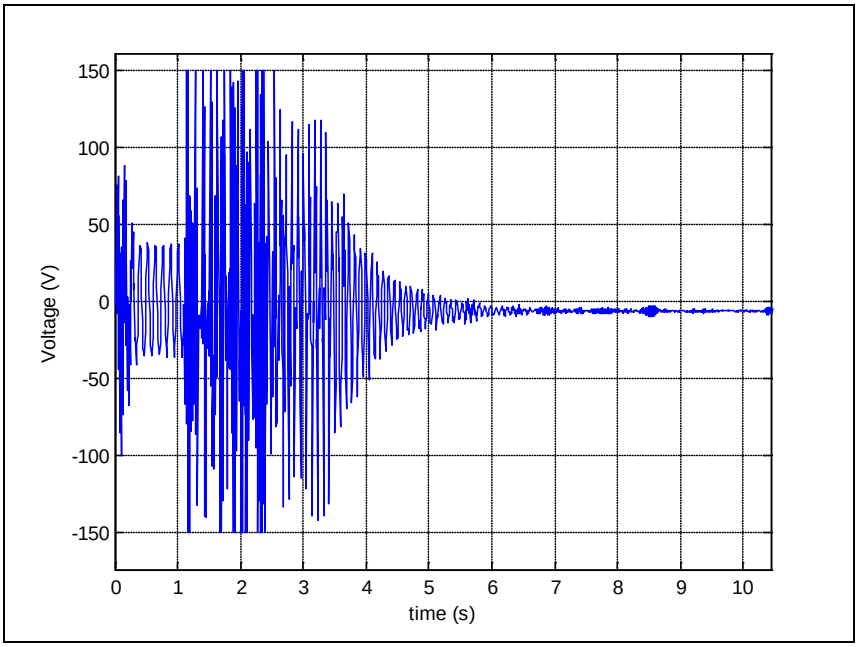

Figure 5.82: Power Amplifier Voltage (Axial Axis) after Adding APMD

6. CONCLUSIONS AND FUTURE WORK

6.1 Conclusions

Based upon the study, findings, and results the following can be concluded:

a) Embedding a downhole flywheel inside a BHA in order to replace existing lithium-ion battery packs is possible, given the geometric and environmental constraints. In this study, a flywheel was sized to be fitted in a 9” OD BHA allowing 3” of mudflow, and operating at a downhole pressure of 30 kpsi. The downhole flywheel can store 1 kW.hr of kinetic energy that is converted to electric energy by decelerating from a maximum speed of 30,000 rpm to a minimum of 10,000 rpm.

b) The magnetic levitation control system can continuously maintain the suspension of the flywheel within the 0.35 mm clearance circle of the catcher bearings due to axial and lateral excitations. The proportional and derivative gains of the controller can be further increased to limit the maximum relative motion of the flywheel with respect to the BHA to 0.12 mm or less, allowing for more sustainability under extreme downhole vibrations.

c) Increasing the controller gains will increase the equivalent stiffness and damping of the AMBs and hence the downhole flywheel is able to withstand severe vibrations but at the same time, this may lead to an increase in coil current and voltage across the power amplifier that can lead to saturation. Thus, optimum values of proportional and derivative gains must be utilized to effectively tolerate the severe downhole

vibrations, in addition to avoiding coil current and power amplifier voltage saturation.

d) The design of an axial passive proof-mass-damper (PPMD) was developed in order to mitigate and suppress bit-bounce vibrations, in addition to reducing the torsional BHA vibrations, since the drillbit cutting dynamics couple the axial and torsional modes. At lower values of top drive spin speeds, the BHA is susceptible to axial and torsional vibrations, especially when utilizing PDC drilbits, where the associated time-delay value is high which increases the negative damping in the system leading to an instability in the form of limit cycle oscillations. Vice versa, at higher values of top drive speeds, these coupled axial and torsional vibrations disappear and a PPMD may not be needed.

e) The value of PPMD sprung-mass needed to suppress bit-bounce at lower values of top drive speeds is less than that of adding additional drill-collar sections to the existing BHA (unsprung-mass case). At very low speeds the ratio of unsprung to sprung mass can be as high as 3, and this ratio decrease by increasing top drive speeds until neither sprung nor unsprung mass are needed. The values of the PPMD sprung mass were selected to be between 10 – 30 % of the original BHA mass. Drilling at lower top drive spin speeds is desirable as it requires less power to operate especially if the available power is limited and higher top drive speeds may not be feasible.

f) The values of the mass, stiffness, and damping of the PPMD can be tuned to completely suppress bit-bounce and torsional vibrations. Results indicated robustness of using a universal type PPMD with constant natural frequency and damping ratio to mitigate bit-bounce and torsional vibrations over a wide range of operating top drive spin speeds as well as rock formation stiffness values and types. Tables 6.1 – 6.4 summarize the results obtained and the effectiveness of the PPMD over a wide range of values formation stiffness for both PDC and tricone drillbits.

g) The optimization and tuning of the PPMD can either be performed by numerical integration of the equations of motion or via utilizing the Cheyshev spectral method technique described by evaluating the eigenvalues of the system that incorporates the induced time-delay through the PDC drillbit cutting dynamics. The Chebyshev spectral method is much faster compared to numerical integration, and extra thousands of possible mass, damping, and stiffness can be scanned during the same period it takes to iterate through a number of a limited number of operating points by numerical integration.

h) The Chebyshev spectral method enables the fast determination of stable operating points over a wide range of conditions and thus stability operating charts can be obtained efficiently in much reduced computational time. The stability chart produced in this study was obtained in less than 45 minutes whilst it would have

taken over 100,000 hours to scan 1.2 million possible operating points via numerical integration, especially for systems with extended degrees of freedom.

i) The validity of the Chebyshev spectral method was verified by simulating the system's performance through numerical integration of the equations of motion under the same operating conditions, and there was an agreement between the cutoff stable top drive spin speed, effectiveness of PPMD, as well as the frequency and periodic time of the limit cycle oscillations.

j) Adding a torsional degree of freedom to PPMD didn't affect the stability of the system either in a positive or a negative manner.

k) The study addressed a new type of coupling between the lateral, axial and torsional modes of vibration of the drillstring due to the inclination of the rock formation reaction (or WOB) with respect to the BHA axis, and to the best of knowledge, there is no work in the literature that specifically addressed this issue, and the only lateral axial coupling mentioned was that due to buckling. Even for small inclination angles, a rock formation reaction average value of 100 kN will yield a lateral component of 1.75 – 8.75 kN for inclinations of 1 – 5 degrees, respectively.

l) Extending the PPMD to the lateral dimension yielded mitigation of lateral vibrations either at the center of gravity of the BHA or near the drillbit. Since the distance

between the center of gravity and the drillbit is over 300 feet, two lateral PPMD must be utilized in order to reduce the size of the lateral orbit at each location since the excitation at the center of gravity is due to the mass unbalance, and that at the drillbit is due to the lateral component of the WOB.

m) It is strongly recommended to use addition stabilizers that provide addition damping to ground if a lateral PPMD is utilized in order to avoid whirling of the BHA. If the whirling is of backward type, there will be rolling contact between the BHA and the wellbore that will lead to undesirable reverse bending in the drillstring.

n) The concept of the proof-mass-damping was expanded to the flywheel in order to achieve an active proof-mass-damper (APMD) whose equivalent stiffness and damping values can be tuned by adjusting the proportional and derivative controller gains, respectively, especially that these stiffness and damping values are equal to or greater than those utilized in the PPMD. Since the flywheel mass is small (less than 150 kg), multiple modules could be embedded in a light BHA such that the combined flywheel modules mass is approximately 7 – 15 % of the original BHA mass.

o) Simulations indicated that the proposed APMD successfully suppressed bit-bounce and torsional vibrations of a light-weight BHA drilling through a soft formation.

Four flywheels modules were utilized and their combined mass was 6.5 % of the original weight of the BHA.

p) Utilizing high proportional and derivative controller gains in order to achieve an APMD and at the same time avoid axial catcher bearing collision yielded an AMB coil current below the saturation limit of 20 A but there some transient voltage saturation across the power amplifier.

Table 6.1: Drillstring Original Axial Vibration (PDC Drillbit)

Spin Speed (rpm)	Formation Stiffness = 80 MN/m	Formation Stiffness = 120 MN/m	Formation Stiffness = 160 MN/m
	Vibration Amplitude (mm/s)	Vibration Amplitude (mm/s)	Vibration Amplitude (mm/s)
60	114	120	125
70	93	100	116
80	74	86	101
90	48	74	87
100	0.5	41	83
110	0.2	28	77
120	0.1	2	88
130	0.1	0.1	57
140	0.1	0.1	0.1

Table 6.2: Axial Vibration Percentage Reduction Utilizing PPMD (PDC Drillbit)

Spin Speed (rpm)	PPMD /BHA Mass Ratio	Formation Stiffness = 80 MN/m			Formation Stiffness = 120 MN/m			Formation Stiffness = 160 MN/m		
		0.15	0.2	0.25	0.15	0.2	0.25	0.15	0.2	0.25
60		34.2	38.60	43.86	31.67	34.17	37.50	30.40	38.40	43.20
70		29.1	33.33	48.39	25.00	27.00	30.00	28.45	35.34	41.38
80		20.2	25.68	95.95	19.77	22.09	38.37	26.73	31.68	35.64
90		97.9	98.96	99.79	13.51	32.43	35.14	26.44	29.89	33.33
100		100	100	100	26.83	48.78	68.29	28.92	32.53	38.55
110		100	100	100	32.14	57.14	98.21	42.86	54.55	61.04
120		100	100	100	90.00	95.00	100	51.14	65.91	71.59
130		100	100	100	100	100	100	98.25	99.12	100
140		100	100	100	100	100	100	100	100	100

Table 6.3: Drillstring Original Axial Vibration (Roller-Cone Drillbit)

Spin Speed (rpm)	Formation Stiffness = 80 MN/m	Formation Stiffness = 120 MN/m	Formation Stiffness = 160 MN/m
	Vibration Amplitude (mm/s)	Vibration Amplitude (mm/s)	Vibration Amplitude (mm/s)
60	65	62	55
70	66	65	57
80	68	66	58
90	70	68	60
100	73	72	62
110	76	74	64
120	79	78	66
130	82	80	68
140	85	82	70

Table 6.4: Axial Vibration Percentage Reduction Utilizing PPMD (Roller-Cone Drillbit)

Spin Speed (rpm)	PPMD /BHA Mass Ratio	Formation Stiffness = 80 MN/m			Formation Stiffness = 120 MN/m			Formation Stiffness = 160 MN/m		
		0.15	0.2	0.25	0.15	0.2	0.25	0.15	0.2	0.25
60		76.92	81.54	84.62	85.48	90.32	93.55	94.55	96.36	98.18
70		77.27	80.30	83.33	86.15	90.77	93.85	94.74	96.49	98.25
80		76.47	77.94	82.35	84.85	89.39	92.42	94.83	96.55	98.28
90		75.71	77.14	80.00	85.29	89.71	92.65	93.33	95.00	96.67
100		75.34	78.08	80.82	84.72	88.89	91.67	93.55	95.16	96.77
110		73.68	76.32	78.95	85.14	89.19	90.54	93.75	95.31	96.88
120		73.42	75.95	78.48	84.62	88.46	91.03	92.42	93.94	95.45
130		73.17	75.61	76.83	85.00	88.75	90.00	92.65	94.12	95.59
140		70.59	72.94	76.47	84.15	87.80	90.24	92.86	94.29	95.71

6.2 Future Work

The work and results obtained from this study can be extended but not limited to:

a) Building and testing a lab prototype of the proposed downhole flywheel concept and comparing the performance of the flywheel in the lab with the simulations based on the model stated in this study.

b) Developing an advanced prototype of the proposed downhole flywheel concept for field testing in a deep oil well and comparing the performance of the flywheel in the field with that in the lab and also with the simulations based on the integrated flywheel – BHA model developed in this study.

c) Developing advanced control laws for the magnetic levitation system that include nonlinear control and artificial intelligence such as neural networks, fuzzy logic and neuro-fuzzy especially with the very recent advancement and development of embedded digital systems that can withstand extreme high temperatures and pressures.

d) Development and further optimization of the flywheel and magnetic bearing design and parameter values using advanced optimization methods or genetic algorithms.

e) Development of a lab test rig to measure and quantify reaction forces and torques induced on drillbits to further enhance the drillbit cutting dynamics models utilized in this study.

f) Building and testing a lab prototype for the proposed passive proof-mass-damper (PPMD) and comparing the performance of the flywheel in the lab with the simulations based on the model stated in this study.

g) Developing an advanced prototype of the proposed PPMD concept for field testing in a deep oil well and comparing the performance of the PPMD in the field with that in the lab and also with the simulations based on the model developed in this study.

h) Performing advanced bifurcation and stability analysis of the time-delay differential equations that contribute to the bit-bounce and stick-slip dynamics.

i) Extension of this study to directional and horizontal drilling.

j) Extending the concepts and theory developed and applied in this study to other applications that operate in extreme environment such as fighter aircraft and submarines.

REFERENCES

[1] A. Yigit, A. Christoforou, Stick-Slip and Bit-Bounce Interaction in Oil-Well Drillstrings, *Journal of Energy Resources Technology* 128 (2006) 268–274.

[2] A. Yigit, A. Christoforou, Fully Coupled Vibrations of Actively Controlled Drillstrings, *Journal of Sound and Vibration* 267 (2003) 1029–1045.

[3] A. Yigit, A. Christoforou, Coupled Torsional and Bending Vibrations of Drillstring Subject to Impact with Friction, *Journal of Sound and Vibration* 215 (1998) 167–181.

[4] A. Yigit, A. Christoforou, Coupled Torsional and Bending Vibrations of Actively Controlled Drillstrings, *Journal of Sound and Vibration* 234 (1) (2000) 67–83.

[5] Y. Khulief, F. Al-Suliman, S. Bashmal, Vibration Analysis of Drillstrings with Self-Excited Stick–Slip Oscillations, *Journal of Sound and Vibration* 299 (2007) 540–558.

[6] R. Sampaio, M. Piovan, G. Lozano, Coupled Axial/Torsional Vibrations of Drill-Strings by Means of Non-Linear Model, *Mechanics Research Communications* 34 (2007) 497–502.

[7] P. Spanos, A. Sengupta, R. Cunningham, P. Paslay, Modeling of Roller Cone Bit Lift-Off Dynamics in Rotary Drilling, *Journal of Energy Resources Technology* 117 (1995) 197–207.

[8] J. Roukema, Y. Altintas, Time Domain Simulation of Torsional–Axial Vibrations in Drilling, *International Journal of Machine Tools & Manufacture* 46 (2006), 2073–2085.

[9] S. Voronov, A. Gouskov, A. Kvashnin, E. Butcher, S. Sinha, Influence of Torsional Motionon the Axial Vibrations of a Drilling Tool, *ASME Journal of Computational and Nonlinear Dynamics* 2 (2007) 58–64.

[10] T. Richard, E. Detournay, M. Fear, B. Miller, R. Clayton, O. Matthews, Influence of Bit-Rock Interaction on Stick-Slip Vibrations of PDC bits, *Proceedings of the SPE Annual Technical Conference & Exhibition*, San Antonio, TX, 2002

[11] T. Richard, C. Germay, E. Detournay, Self-Excited Stick–Slip Oscillations of Drill Bits, *C.R. Mecanique* 332 (2004) 619–626.

[12] C. Germay, N. Wouw, H. Nijmeijer, R. Sepulchre, Nonlinear DrillString Dynamics Analysis, *SIAM Journal of Applied Dynamical Systems* 8 (2) (2009) 527–553

[13] B. Gien, Drill String Shock Absorbers, *US Patent 5377772*, Jan 1995.

[14] O. Aldraihem, A. Baz, System, Method for Drill String Vibration Control, *International Patent WO 2010/117963 A1*, 2010.

[15] W. Koger, Downhole Shock Absorbers for Torsional & Axial Loads, *US Patent 2009/0023502 A1*, 2009.

[16] J. Pabon, J. Sihler, D. Pafitis, H. Chaur-Jiang, Methods & Apparatus For Attenuating Drillstring Vibrations, *International Patent WO 2008/036498 A1*, 2008.

[17] D. Bowar, P. Blair, J. Ficken, Downhole Vibration Dampener, *International Patent WO 2010/085321 A1*, 2010.

[18] M. Wassel, Magnetorheological Fluid Apparatus, Especially Adapted for Use in a Steerable Drill String, and a Method for Using Same, *US Patent 6,257,356 B2*, July 2001.

[19] M. E. Cobern, M. E. Wassell, Drilling Vibration Monitoring & Control System, *Presented at the National Gas Technologies II Conference*, Phoenix, AZ, 8-11 February, 2004.

[20] M. E. Cobern, M. E. Wassell, Laboratory Testing of an Active Drilling Vibration Monitoring & Control System, *AADE 2005 National Technical Conference and Exhibition*, Houston, TX, 2005.

[21] M. Elsayed, C. Aissi, Analysis of Shock Absorber Characteristics for Drillstrings, *Proceedings of the ASME 8th Biennial Conference on Engineering Systems Design and Analysis (ESDA2006)*, July 2006, Torino, Italy.

[22] D. Raymond, M. Elsayed, Controllable Magneto-Rheological Fluid-Based Dampers for Drilling, *US Patent 7036612*, 2006.

[23] B. Schmalhorst, Dynamic Behaviour of a Bit-Motor-Thruster Assembly, *SPE Paper 52823, SPE/IADC Drilling Conference*, March 1999, Amsterdam, Holland.

[24] K. Mongkolcheep, A. Palazzolo, A. Ruimi, R. Tucker, A Modal Approach for Chaotic Vibrations of a Drillstring, *Proceedings of the ASME IDETC/CIE 2009*, San Diego, California, USA

[25] A. Yigit, A. Christoforou, Coupled Axial and Transverse Vibrations of Oilwell Drillstrings, *Journal of Sound and Vibration* 195 (4) (1996) 617–627.

[26] G. Sun, A. Palazzolo, A. Provenza, G. Montague, Detailed Ball Bearing Model for Magnetic Suspension Auxiliary Service, *Journal of Sound and Vibration* 269 (2004) 933–963.

[27] J. Park, A. Palazzolo, MIMO Active Vibration Control of Magnetically Suspended Flywheels for Satellite IPAC Service, *ASME Journal of Dynamic Systems, Measurement, and Control* 130 (2008).

[28] S. Lei, A. Palazzolo, Control of Flexible Rotor Systems with Active Magnetic Bearings, *Journal of Sound and Vibration* 314 (2008) 19–38.

[29] A. Kenny, A. Palazzolo, Single Plane Radial, Magnetic Bearings Biased With Poles Containing Permanent Magnets, ASME Journal of Mechanical Design, 125 (2003) 178–185.

[30] B. Grbesa, Low Loss and Low Cost Active Radial Homopolar Magnetic Bearing, *Proceedings of the Sixth International Symposium on Magnetic Bearings*, Cambridge, MA (1998) 286–295.

[31] C.K. Sortore, P. Allaire, H. Maslen, R. Humphris, P. Studer, Permanent Magnetic Biased Bearings–Design, Construction, and Testing, *Proceedings of the Second International Symposium on Magnetic Bearings*, Tokyo (1990) 175–182.

[32] U. Na, Fault-Tolerant Control of Heteropolar Magnetic Bearings, *Ph.D. Dissertation, Texas A&M University, College Station, TX*, 1999.

[33] Y. Okadaet, B. Nagai, T. Shimane, Cross Feedback Stabilization of the Digitally Controlled Magnetic Bearing, *ASME Journal of Vibration and Acoustics* 114 (1992) 54–59.

[34] D. Meeker, E. Maslen, M. Noh, An Augmented Circuit Model for Magnetic Bearings Including Eddy Currents, Fringing, and Leakage, *IEEE Transactions of Magnetics* 32 (4) (1996) 3219–3227.

[35] C. Kim, A. Palazzolo, A. Kascak, G. Brown, Eddy Current Effects on the Design of Rotor-Magnetic Bearing Systems, *ASME Journal of Mechanical Design* 117 (B) (1995) 162–170.

[36] H. Jeong, C. Kim, C. Lee, Modeling and Control of Cone-Shaped Active Magnetic Bearing System, *Proceedings of the International Symposium on Magnetic Bearings*, Vol. 4, Zurich, Switzerland, August 1994, pp. 23–28.

[37] Y. Zhuravlyov, On LQ-Control of Magnetic Bearing, *IEEE Transactions of Control System Technology* Vol. 8, No. 2, 2000, pp. 344–350.

[38] Y. Zhuravlyov, Linear Quadratic Optimal Control of Active Magnetic Bearings for High Speed Rotor, *Proceedings of International Symposium on Magnetic Bearings*, Vol. 6, Boston, USA, August 1998, pp. 587–596.

[39] F. Losch, C. Gahler, R. Herzog, M-Synthesis Controller Design for a 3MW Pump running in AMBs, *Proceedings of the Sixth International Symposium of Magnetic Bearings*, Cambridge, MA, August 1998, pp. 415–428.

[40] M. Hirata, K. Nomani, T. Ohno, Robust Control of a Magnetic Bearing System Using Constantly Scaled H-Infinity Control, *Proceedings of the Sixth International Symposium of Magnetic Bearings*, Cambridge, MA, August 1998, pp. 713–722.

[41] S. Lei, A. Palazzolo, A. Kenny, A. Kascak, Fuzzy Logic Control of Magnetic Bearings for Suppression of Vibration due to Sudden Imbalance, *Proceedings of the Fifth International Symposium of Magnetic Suspension Technology*, Santa Barbara, CA, 1999, pp. 459–471.

[42] W. Zhang, J. Zu, Transient and Steady Nonlinear Responses for a Rotor-Active Magnetic Bearings System with Time-Varying Stiffness, *Journal of Chaos, Solitons and Fractals* 38 (2008) 1152–1167.

[43] Yeonkyu Kim, Integrated Power and Attitude Control of a Rigid Satellite with Onboard Magnetic Bearing Suspended Rigid Flywheels, *Ph.D. Dissertation, Texas A&M University, College Station, TX*, 2003.

[44] A. Chiba, T. Fukao, O.Ichikawa, M. Oshima, M. Takemoto, D. Dorrell, *Magnetic Bearings and Bearingless Drives*, Elsevier, Oxford, United Kingdom, 2005.

[45] R. Viguié, G. Kerschen, Design Procedure of a Nonlinear Vibration Absorber Using Bifurcation Analysis, *Proceedings of the IMAC-XXVII*, February 9-12, 2009 Orlando, Florida USA.

[46] R. Budynas, K. Nisbett, *Shigley's Mechanical Engineering Design*, McGraw-Hill, 2006.

[47] J. Fu, T. Shi, Dynamic Analysis of BHA with Bent Housing, *SPE Paper 37046, 1998 International Conference on Horizontal Well Technology*, Calgary, Canada.

[48] P. Defourny, F. Abbassian, Flexible Bit: A New Antivibration PDC-Bit Concept, *SPE Paper 52888, SPE Drilling & Completion*, December 1998.

[49] J.S. Przemieniecki, *Theory of Matrix Structural Analysis*, McGraw-Hill, New York, USA, 1968.

[50] Breda et al., Pseudospectral Differencing Methods for Characteristic Roots of Delay Differential Equations, *SIAM Journal on Scientific Computing* 27 (2) (2005) 482–495.

[51] D. Breda, Numerical Computation of Characteristic Roots for Delay Differential Equations, *Ph.D. thesis, Universit`a degli Studi di Padova*, 2004.

[52] E. Jarlebring, The Spectrum of Delay-Differential Equations: Numerical Methods, Stability and Perturbation, *Ph.D Dissertation, Technische Universit¨at Carolo-Wilhelmina zu Braunschweig*, Sweden, 2008.

[53] G. Mayers, D. Goldberg, J. Rector, Drill String Vibration: A Proxy for Identifying Lithologic Boundaries while Drilling, *Proceedings of the Ocean Drilling Program, Scientific Results* Vol. 179, 2002.

[54] I. Forester, Axial Excitation as a Means of Stick-Slip Mitigation: Small Scale Rig Testing and Full Scale Field Testing, *SPE Paper 139830, 2011 SPE/IADC Drilling Conference and Exhibition*, Amsterdam, The Netherlands.

[55] J. McCarthy, I. Forester, T. Burnett, A. Kabbara, Careful Planning and Application of an Asymmetric Vibration Damping Tool Dramatically Improves Underreaming While Drilling Performance in Deepwater Drilling, *OTC Paper 22439, 2011 Offshore Technology Conference*, Rio de Janeiro, Brazil.

VITA

Ahmed Mohamed Saeed received his Bachelor of Science degree in mechanical engineering from Alexandria University, Egypt in 2003. He was appointed as a teaching assistant at the Faculty of Engineering, Alexandria University, Egypt in September 2003 and received his Master of Science degree in December 2005. Mr. Saeed entered the mechanical engineering graduate program at Texas A&M University in August 2006 and received his Doctor of Philosophy degree in May 2012. His research interests include intelligent control systems, rotordynamics, flywheel energy storage systems, and drillstring dynamics.

Mr. Saeed may be reached at 10804 Fallstone Rd. Suite 210, Houston, TX 77099. His email is ahmednoorsaeed@yahoo.com.